UC Berkeley
UC Berkeley Electronic Theses and Dissertations

Title

Development and Applications of Multiplexed Charge Detection Mass Spectrometry

Permalink

https://escholarship.org/uc/item/09j66568

Author

Harper, Conner Cox

Publication Date

2020

Peer reviewed|Thesis/dissertation

eScholarship.org Powered by the California Digital Library
University of California

Development and Applications of Multiplexed Charge Detection Mass Spectrometry

by

Conner C Harper

A dissertation submitted in partial satisfaction of the

requirements for the degree of

Doctor of Philosophy

in

Chemistry

in the

Graduate Division

of the

University of California, Berkeley

Committee in charge:

Professor Evan R. Williams, Chair
Professor Daniel M. Neumark
Professor Hartmut Häffner

Fall 2020

Development and Applications of Multiplexed Charge Detection Mass Spectrometry

Copyright © 2020

by

Conner C Harper

Abstract

Development and Applications of Multiplexed Charge Detection Mass Spectrometry

by

Conner C Harper

Doctor of Philosophy in Chemistry

University of California, Berkeley

Professor Evan R. Williams, Chair

Mass spectrometry (MS) is a ubiquitous method in analytical science, with applications ranging from physics to molecular biology. The fundamental nature of mass makes weighing molecules and/or their fragments a reliable way to characterize identity, structure, and function. Conventional MS methods work by measuring the mass to charge ratio (m/z) of an ensemble of ionized analyte molecules. The mass is then determined by multiplying the m/z by the charge (z) of the ion, a quantity that is typically determined either by ionization method or by measuring the spacing between m/z peaks. For smaller molecules, deconvolving the charge from the m/z spectrum is straightforward, but becomes increasingly difficult for large molecules (>1 MDa) or samples that contain heterogeneous mixtures because m/z peaks overlap and are unresolved. Single ion MS techniques circumvent this problem by measuring the mass of individual ions via independent measurements of both the m/z and the charge, but these measurement methods are typically too time-consuming to be practical for acquiring the thousands of ions necessary to produce meaningful mass spectrum. This dissertation focuses on the development and application of multiplexed charge detection mass spectrometry (CDMS), a single ion MS technique that enables much faster individual ion mass measurements. A novel data analysis method that uses the amplitudes of the first and second harmonic frequencies in the Fourier transform of ion signal to dynamically determine ion energies is demonstrated. By monitoring the ion energies of individually trapped ions in CDMS, information about ion cross section and neutral solvent evaporation is obtained. For the first time, multiplexed CDMS measurements are demonstrated and the time necessary to acquire a statistically significant sample of individual ion data is decreased by an order of magnitude compared to other CDMS techniques. Simulations of optimized CDMS data show that multiplexed measurements combined with a novel method for decoupling ion m/z and frequency can further decrease the ion acquisition time to less than one minute. These CDMS techniques are applied to the study of the mechanisms of electrospray ionization for nanometer-sized droplets and macromolecules originating from different aqueous solutions and new insights on these previously difficult to measure systems are gained.

Table of Contents

Abstract 1
Table of Contents i
Acknowledgements v
Introduction 1
1.1 Overview 1
1.2 Single Molecule Mass Spectrometry 2
1.3 Charge Detection Mass Spectrometry 4
1.3.1 Single Pass Charge Detection Mass Spectrometry 4
1.3.2 Ion Trap Charge Detection Mass Spectrometry 5
1.4 Applications of Charge Detection Mass Spectrometry 7
1.4.1 Polymer of Charge Detection Mass Spectrometry 7
1.4.2 Native MS of Large Biomolecules 8
1.4.3 Nanodrop Charging in Electrospray Ionization 9
1.5 References 10
Determining Energies and Cross Sections of Individual Ions using Higher Order Harmonics in Fourier Transform Charge Detection Mass Spectrometry (FT-CDMS) 20
2.1 Abstract 20
2.2 Introduction 20
2.3 Experimental 22
2.4 Results and Discussion 23
2.4.1 Individual Ion Energies from Ratio of Harmonic Amplitudes 23
2.4.2 Ion Signal Simulation 25
2.4.3 Comparison of Model to Signals of PEG Ions 25
2.4.3 Ion Cross Sections from Energy Loss Measurements 27
2.5 Conclusions 28
2.6 Acknowledgements 29
2.7 References 29
2.8 Figures 33

2.8 Supporting Information 37
2.8.1 Determining Ion Energy at Different Trap Potentials 37
2.8.2 SIMION Simulations: Determining Energy Lost from Solvent Evaporation . 37
2.9 Supporting Figures 39
Multiplexed Charge Detection Mass Spectrometry for High Throughput Single Ion Analysis of Large Molecules 41
3.1 Abstract 41
3.2 Introduction 41
3.3 Experimental 43
3.3.1 Charge Detection Mass Spectrometry 43
3.3.2 RuBisCO Expression and Purification 44
3.4 Results and Discussion 45
3.4.1 Ion Motion Inside the Trap 45
3.4.2 Mass Analysis 46
3.4.3 Mass Analysis and Number of Ions Trapped 47
3.4.4 Gain in Analysis Speed 48
3.5 Conclusions 49
3.6 Acknowledgements 50
3.7 References 50
3.8 Table and Figures 56
3.9 Supporting Information 60
3.9.1 Quadrupole-Time of Flight (Q-TOF) Mass Spectrometry of RuBisCO 60
3.9.2 Bovine Serum Albumen (BSA) CDMS Measurements 60
3.10 Supporting Table and Figures 61
Enhanced Multiplexing in Fourier Transform Charge Detection Mass Spectrometry by Decoupling Ion Frequency from Mass to Charge Ratio 65
4.1 Abstract 65
4.2 Introduction 65
4.3 Theory 67
4.3.1 Decoupling Ion Frequency and *m*/*z* in CDMS 67
4.4 Methods 69
4.4.1 Simulating CDMS Ion Frequencies 69
4.5 Results and Discussion 71

4.5.1 Maximum Gains in Analysis Speed for Different Analytes 71
4.5.2 Improved Quantitation and Dynamic Range via Decoupling 72
4.6 Conclusions 73
4.7 Acknowledgements 74
4.8 References 74
4.9 Tables and Figures 79
4.9 Supporting Information 86
4.9.1 Python Code and Parameters for CDMS Mass Histogram Simulation 86
Direct Observation of Ion Emission from Charged Aqueous Nanodrops: Effects on Gaseous Macromolecular Charging 89
5.1 Abstract 89
5.2 Introduction 89
5.3 Experimental 92
5.3.1 Charge Detection Mass Spectrometry 92
5.3.2 MS2 Capsid Synthesis 92
5.4 Results and Discussion 93
5.4.1 Acquiring Individual Nanodrop Data 93
5.4.2 Nanodrop Mass and Charge Distributions from Different Solutions 94
5.4.3 Comparing Individual “Dry” and “Wet” Ions 94
5.4.4 Direct Observations of Ion Emission 95
5.4.5 Origins of Solution-Dependent Nanodrop Mass and Charge 96
5.4.6 The Role of Ion Evaporation in Charging of MDa Macromolecules 97
5.4.7 Evidence for Solution Phase Capsid Compaction 98
5.5 Conclusions 99
5.6 Acknowledgements 99
5.7 References 100
5.8 Table and Figures 105
5.9 Supporting Information 111
5.9.1 Experimental Details: Charge Detection Mass Spectrometry 111
5.9.2 Charge and Mass Lost after Ion Emission Events 111
5.9.3 Experimental Details: Small Angle X-ray Scattering (SAXS) 111
5.9.4 Experimental Details: Dynamic Light Scattering (DLS) 112
5.9.5 Correlation of Nanodrop Mass and Solute Identity 112

5.9.6 Supporting Reference 112
5.10 Supporting Figures 113
Conclusions and Future Directions 123
6.1 Conclusions 123
6.2 Future Directions and Applications of CDMS 124
6.2.1 The Need for Speed 124
6.2.2 Advantage of Dynamic Energy Measurement 125
6.3 Next-generation CDMS Instrumentation 126
6.4 References 127
6.5 Figures 129

Acknowledgements

There are many people to whom I would like to express gratitude for their roles in supporting me and the work in this dissertation. First and foremost, I am deeply indebted to my dear wife of eight years (and counting!), Alicia Harper, for her unwavering faith and patience with me as I have strived to accomplish my goals. Despite trials associated with our initial move to a place far away from family, the birth of our first child, Abigail, and the imminent birth of our second, she has always been there for me, offering encouragement and support. Her love is my greatest asset. I would like to express gratitude to my parents, Kelly and Carilee Harper for their constant loving support. My father Kelly, for teaching me that anything worth learning is worth learning well and my mother, Carilee, for teaching me to always give my best effort regardless of the expectations set by others. The examples of my older siblings, Travis Harper, KiLee Taylor, Lexi Ritchie, Dr. Kaid Harper, and Kasia Johnson have been a guide to me throughout my life in both professional and personal pursuits. I would be remiss if I did not also mention my parents-in-law, Philip and Etsuko Davis, and all of my siblings-in-law, Deborah Harper, Dr. Nathan Taylor, Michael Ritchie, Jenny Harper, Michael Johnson, Candice Davis, Chelsea Davis, and Shyanne Davis for their love and encouragement. I am lucky to have such an extensive family support system; I don't know where I'd be without them.

I would also like to express gratitude to all those who have played a role in my professional development. My advisor, Professor Evan Williams, for his active mentorship throughout my graduate tenure, in both teaching me the principles of mass spectrometry and instrumentation as well as thoroughly refining my scientific reading and writing skills. His availability and enthusiasm for discussing science has been 'instrumental' to the work presented in this dissertation. My colleagues in the Williams group have also been a key part of my graduate career. Among all, I must first mention Dr. Andrew Elliott, who trained me in my early graduate career, provided the basis on which my research is built, and who is also my friend. Second, Howard Lin, for his willingness to take on even the most tedious of tasks without complaint and his continued friendship despite moving on to his own graduate studies. My research would not have moved forward without the brilliant insights and hard work of these two people. I also wish to express gratitude to Dr. Daniel Mortensen, Dr. Richard Cooper, Dr. Matthew DiTucci, Dr. Anna Susa, Dr. Beryl Xia, and Jacob Jordan for giving the Williams group a friendly, collaborative atmosphere that made my graduate career truly enjoyable.

Chapter 1

Introduction

1.1 Overview

Mass spectrometry (MS) is considered the "gold standard" of analytical technology across a broad range of scientific disciplines ranging from physics to molecular biology. The fundamental nature of mass and charge make the mass-to-charge ratios (abbreviated as m/z) typically measured in mass spectrometry very useful in understanding molecular properties. Measuring the exact mass of a molecule makes it possible to unambiguously determine molecular formulas. Information about molecular structure can also be obtained by fragmentation and subsequent mass measurement of product ions. This strategy has proven particularly useful in the analysis of peptides and proteins because the primary amino acid sequence can be determined from the distribution of smaller peptide fragments.[1] Combined with advanced data analysis methods and chromatography, more than 10,000 unique proteins from a single cell line can be identified in ~100 min.[2] While fragmentation is very useful for these purposes, other information, such as higher order structure, ligand binding, and post-translational modifications, can be lost in the process. Using native MS, where biomolecular ions are generated from solutions in which they have their native or native-like structures, much of this information is retained and can be used to probe both the structure and function of these molecules.[3–12]

While there are many advantages to using native MS to study macromolecules, limitations in current MS instrumentation can make measurements of these large species difficult. Ions in native MS are typically produced by electrospray ionization (ESI), the technique best suited for producing minimally disrupted macromolecular ions.[13] Ions of large macromolecules formed by ESI are typically multiply charged. This can be advantageous for improved detection because a distribution of multiply charged ions results in multiple ion signal peaks at lower m/z values where most conventional MS instrumentation is more sensitive and better signal in charge detection-based instruments. The mass of the ion is determined either by deconvolving the m/z peak distribution or, if sufficient resolution is achieved, from isotope peak spacing. However, these methods rely on an ensemble measurement of the ions in sample and becomes increasingly difficult as the heterogeneity of the sample increases. Heterogeneity originating from either the intrinsic properties of an analyte or extrinsic factors such as salt adduction yields a wide distribution of ion masses and an even wider distribution of ion m/z values. Mixtures of analytes in the same size range can add even further complexity to these spectra. Ultimately, ability to resolve the charge states corresponding to a particular analyte mass can be lost due to overlapping m/z peaks and no direct mass measurement can be made. For relatively homogeneous samples analyzed using commercially available MS instrumentation, analytes up to ~1 MDa can typically be measured, but larger species, such as many viruses and viral capsids, are challenging to weigh

due to their intrinsic heterogeneity alone.[14–16] In the case of a heterogeneous mixture, such as large synthetic polymers, the analyte mass at which resolution is lost can be as low as ~40 kDa.[17–19]

One way to circumvent the problem of heterogeneity in MS is to measure the masses of individual ions rather than measuring a *m*/*z* spectrum of an ensemble of ions.[20,21] This method eliminates interferences from other ion signals, making it highly robust to heterogeneity. Unlike ensemble *m*/*z* spectra where the charge can be inferred from isotope or charge state spacing, independent measurements of both *m*/*z* and charge are required for each individual ion. Measuring the charge in addition to the *m*/*z* can provide a more detailed view of the ions in a sample because two ions with the same *m*/*z* but different charges may indicate differences in structure or identity. The accuracy to which both of these quantities can be measured is also an important consideration because a poor-quality measurement of either quantity results in highly uncertain masses. Measurement quality can often be improved using signal averaging for the same ion, but this gain in quality comes at a cost of longer measurement time. Measurements of many thousands of ions are necessary in order to characterize constituent analytes in a mixture and the dynamic range of this method depends on the number of ions measured. As a result, the time required to acquire a sufficient sample of ion data can be prohibitively long for single ion techniques. Individually tracking and calculating the mass of each ion can also be computationally intensive. Thus, despite the advantages of individual ion MS, these considerations have historically resulted in comparably minor scientific investment in individual ion MS techniques when compared to their ensemble counterparts.

Growing interest in increasingly complex and heterogeneous systems in molecular biology, biochemistry, and medicine as well as improved computing and electronics have recently revitalized the development of MS techniques for individual ion mass measurement. A wide range of individual ion MS techniques are currently under development. The work described in this dissertation is focused on the development of a multiplexed charge detection mass spectrometer and its applications. Chapter 2 presents a novel data analysis technique that allows the simultaneous and dynamic measurement of the *m*/*z*, charge, and energy of individual trapped ions. Chapter 3 demonstrates multiplexed individual ion measurements that significantly increase analysis speed in individual ion MS and further builds on the analysis techniques developed in Chapter 2. Chapter 4 uses simulated ion properties to determine the maximum extent of multiplexing and analysis speed possible using existing instrumentation. Chapter 5 describes the application of the technology developed in Chapters 2-4 to the analysis of aqueous nanodrops and viral capsids generated by ESI that originate from different solutions.

1.2 Single Molecule Mass Spectrometry

Several different techniques to measure the masses of individual molecules have been developed, each with their respective advantages and limitations. For time-of-flight (TOF) instruments, ion *m*/*z* is related to the time required for the molecule to reach the detector after an initial electrostatic acceleration and theoretically has no upper mass limit. However, detection sensitivity using a microchannel plate decreases significantly at the low velocities associated with

high *m*/*z* ions.[22,23] Cryodetector-TOF techniques address this sensitivity issue by measuring the incident kinetic energy of each molecule, a quantity that should theoretically scale linearly with the charge of the molecule.[24] However, the ion energy measured in practice for large molecules does not scale linearly with charge because factors such as fragmentation, impact product ion ejection, and surface deformation result in variable energy transfer.[25,26] The resulting uncertainty in charge measurement makes this technique difficult to use for large ions produced by ESI, which typically have a high number of charges, but singly and doubly charged polymer ions produced by matrix assisted laser desorption ionization (MALDI) have been measured at *m*/*z* over 1,000,000 Da.[27,28] Nanoelectromechanical systems (NEMS) measure the mass of individual particles via a change in the resonant oscillation frequency of a nanoscale vibrating cantilever that is caused by a molecule adsorbing to the cantilever surface.[29] Uniquely, NEMS does not require ionization of the analyte because the change in oscillation frequency is directly related to the mass of the adsorbed analyte.[30] However, NEMS is sensitive to the properties of each resonator, such as stiffness[31] and particle saturation,[32] as well as the position that each molecule adsorbs,[29,33,34] leading to low mass resolution (5m/Δm) and long experiment times.

Single ion mass measurements using conventional MS instrumentation have been made by measuring the ion charge in addition to the ion *m*/*z*. One approach determines ion charge by repeatedly changing the charge of a single ion. Each time the charge on the same ion is changed, the *m*/*z* is measured, yielding a set of charge states that can then be deconvolved similarly to ensemble *m*/*z* methods. This approach has been applied to individual trapped ions in both quadrupole ion trap (QIT)[35,36] and Fourier transform ion cyclotron resonance (FT-ICR)[37–39] mass spectrometers using both optical and chemical methods to induce changes in the ion charge. While high precision individual ion mass measurements have been achieved using these methods, the time required for these measurements is prohibitively long, ranging from many seconds to minutes per ion, making these methods impractical for acquiring data for the thousands of ions required to fully characterize a sample.

An alternative approach to determining the charge of individual ions is to quantitatively measure the current induced on an electrode by the near passage of the ion. Measurement of an induced signal is used in both FT-ICR and Orbitrap mass spectrometers for both ion ensemble and individual ion detection. In FT-ICR MS, measurement of individual ion charge is complicated by the positional variation of the ion within the trapping cell. Ions with different kinetic energies oscillate at different distances from the detection electrodes,[40] making it more difficult and time-consuming to calibrate the image current to the ion charge.[41,42] Like FT-ICR MS, the current induced in an Orbitrap mass spectrometer also depends on radial position of the ion but is more straightforwardly controlled and calibrated to the ion charge. A limitation of this technique is that the widths of the induced current distributions for individual ions are sufficiently broad that integer charge states cannot be assigned based on individual ion signal amplitude alone.[43,44] However, the high-resolution *m*/*z* measurement possible with the Orbitrap combined with the narrower intrinsic *m*/*z* linewidths associated with individual ion measurements make it possible to increase resolving power by a factor of ~20.[45] The high kinetic energies of ions in the Orbitrap also make their survival for the duration of the trapping period (typically between 0.5 – 3 s) highly dependent on

background pressures and the central electrode potential, although survival rates improve with increasing analyte mass.[44,46,47] Recent single ion Orbitrap work has reduced the typical operating pressure in the Orbitrap cell (~1×10^{-10} torr) by two orders of magnitude (~1×10^{-12} torr) to reduce these ion losses.[46] Using this modified Orbitrap instrumentation, multiplexed measurements of more than 100 ions for both large (>1 MDa)[44] and small (<1 MDa)[45,47,48] individual ions have been demonstrated and decrease the total acquisition time required to analyze a sample, but no details on total experiment length are currently available.

1.3 Charge Detection Mass Spectrometry

Charge detection mass spectrometry (CDMS) is technique specifically developed for the purposes of individual ion measurement. In CDMS, the charge on the ion is measured via induced current, similar to Orbitrap and FT-ICR detection methods. However, unlike these other methods, the ion passes through a conductive cylinder with dimensions (length ~4x greater than the inner diameter) such that the image charge induced by an ion is >99% of the actual charge of the ion and is minimally affected by the radial position of the ion.[49] Thus, the charge of the ion can be directly determined from the amplitude of the pulse generated by its passage. The temporal length of the pulse and the known length of the conductive cylinder also make it possible to determine the velocity of the ion. Energy selective ion optics are used to isolate ions with a narrow range of known kinetic energies. The ion m/z is then obtained from this kinetic energy and the measured ion velocity. The mass of each individual ion is determined from these independent measurements of both charge and m/z. Many individual ion mass measurements are then compiled to form a mass histogram representative of the different analytes in a sample. Advantages of this technique are its relative simplicity and the potential for faster individual ion measurements, because only a single pass of the ion through the conductive cylinder (typically 10-100 μs) is required for mass measurement.

1.3.1 Single Pass Charge Detection Mass Spectrometry

Single pass CDMS instruments have been used to measure the masses of a variety of analytes. Single pass CDMS was first developed in the 1960's to measure the mass of micron-sized ion particles with >10,000 fundamental charges (e) with a mass measurement error of ~20%.[50] Advances in detection electronics and instrumentation improved on initial CDMS experiments, reducing the limit of charge detection to 1500 e for measurements of cosmic dust particles.[51–53] Further improvements led to single pass CDMS with improved limits of detection (~300 e) and charge accuracy (~75 e) on various biomolecules, synthetic polymers, and nanoparticles.[54,55]

The relatively high uncertainties in the charge determined by single pass CDMS limit the mass accuracy and resolution that can be achieved. However, the uncertainty in CDMS measurements can be decreased by averaging repeated measurements of each individual ion. Signal averaging decreases the charge uncertainty by a factor of $n^{1/2}$, where n is the number of times each ion is measured. One approach to increasing the number of ion charge measurements

is to use multiple detection cylinders aligned along the axis of ion motion. Linear arrays of detection cylinders with up to 22 elements have been used, decreasing the limit of detection to ~100 *e* and charge uncertainty to ~10 *e*.[56] In theory, larger detector arrays could be used, but practical considerations such as array alignment/spacing and increased detection circuit capacitance limit this approach in improving CDMS uncertainties. Non-cylindrical detector arrays integrated into a printed circuit board address alignment and spacing concerns but have unproven charge detection sensitivity and accuracy.[57]

1.3.2 Ion Trap Charge Detection Mass Spectrometry

Another strategy to record multiple measurements of a single ion is to electrostatically trap the ion in the region containing the detection cylinder. The ion recirculates repeatedly through the detector and the number of measurements made is limited by time that the ion is stably trapped rather than the number of detectors. Trapped ion CDMS was first demonstrated using a pair of electrostatic ion mirrors on either side of a shielded detector tube.[58] Other designs using greater numbers of electrostatic ion mirrors or cone electrodes have also proven effective in ion trap CDMS.[59–62] In general, to trap an ion, the entrance-side electrode(s) are held at ground potential, allowing the ion to pass into the detection cylinder. In a self-triggered trapping scheme, ions with sufficient charge (~250 *e*) are detected as they make their first pass through the cylinder and this initial signal serves as a trigger to 'close' the trap by increasing the entrance mirror potential. Because detectable ion signal is required for this self-triggered trapping method, the limit of detection is not significantly lowered compared to single pass CDMS, but charge uncertainties as low as 2.3 *e* have been reported for an ion trapped for 450 passes (10 ms).[58] A CDMS instrument combining the array and ion trap methods achieved a slightly improved charge uncertainty of 2 *e* for ions trapped using self-triggered trapping and a 100 ms trapping period.[60] However, the larger field free detector region required for this combined array-trap instrument resulted in finer tolerances for ion trajectories, leading to shorter average trapping times. Self-triggered ion trapping leads to high trapping efficiency, i.e., an ion is almost always present in the trap when it is 'closed', but the requirement that an ion has sufficient charge to be detected on a single pass limits the size range of analytes that can be weighed. For polymers and denatured biomolecules, which are charged to a greater extent in their extended linear structures, analytes as small as ~2 MDa can be measured, but for native biomolecules and other spherical molecules that have higher *m*/*z*, this low mass cutoff increases to ~10 MDa.

Ions trapped in CDMS instruments induce a periodic signal pattern as they oscillate in and out of the detection cylinder. This pattern of induced charge resembles a rectangular pulse train, a waveform well-suited to analysis using Fourier transforms (FT). The fundamental ion oscillation frequency *f*, can be obtained from the FT and is related to the ion *m*/*z*:

$$\frac{m}{z} = \frac{C(E,V)}{f^2} \qquad (1.1)$$

where C is a function that depends on the trap geometry, ion energy (E), and electrostatic trapping potential (V). The ion charge is determined from the amplitude at the oscillation frequency in the magnitude FT spectrum. FT analysis of CDMS data for trapped ions makes it possible to significantly decrease the limit of detection for individual ions because the frequencies and amplitudes of ions with charge well below the time-domain noise are easily measured in the FT spectrum.

Using FT-based data analysis to decrease the limit of detection requires a different trapping scheme. Instead of closing the trap using the passage of an ion as the trigger, the trap is instead set to close and open at regular intervals. Unlike self-triggered trapping, this scheme does not guarantee an ion is present in the trap prior to closure, which can lead to reduced trapping efficiency and 'empty' time-domain data. However, initial implementation of this method reduced the limit of detection to ~30 e, significantly increasing the range of analytes that can be weighed using CDMS.[59] Subsequent improvements to FT-CDMS, including cryogenically cooled and improved detection electronics,[63–65] longer trapping periods (3 s),[66] improved trap designs,[62,67] calibration using an internal standard signal,[68] and improved data analysis techniques[66,69,70] using the amplitudes of both the fundamental and second harmonic frequencies have decreased the limit of detection to 1 e with a charge uncertainty of 0.174 e.[65] With this low charge uncertainty, the ability to resolve integer charge states has been demonstrated for ions with charge states up to ~500 e and a mass resolution of ~330 has been achieved.[71]

Because the charge can be unambiguously determined, uncertainty in the mass measurement in state-of-the-art CDMS primarily originates from the m/z measurement. Ion m/z is determined from the ion oscillation frequency, the ion energy, and calibration constants based on the electrostatic trap geometry and potential (Equation 1.1). Chapter 2 discusses a novel method for the dynamic, *in situ* measurement of trapped ion energies. This is an important development in CDMS technology because energy-selective ion optics are typically used to admit only a narrow band of ion energies into the CDMS detector. The width of this energy distribution largely determines the uncertainty in the m/z measurement but narrowing the energy distribution results in reduced ion transmission. *In situ* measurement of ion energies is accomplished by measuring the amplitude ratio of the fundamental and second harmonic frequencies, a quantity that is directly related to the duty cycle of the periodic ion signal. For a given ion trap geometry, the measured duty cycle can be calibrated to the ion energy, making it possible to determine the energy of each ion at any time during the trapping period. Changes in ion energy due to collisions with background gas, solvent evaporation, and fragmentation can also be monitored. Chapters 2,3, and 5 highlight some applications of this method.

An additional consideration in the development of CDMS technology is the balance between the time required to acquire enough individual ion data and the mass accuracy of each individual measurement. This balance can be tuned for different analytes in ion trap CDMS with a user-determined trapping period length but was fundamentally limited by the requirement that only one ion could be measured at a time. A review of CDMS states that "…multiple ion trapping events cannot be analyzed because two highly charged ions trapped together interact and perturb

the oscillation frequencies. Hence, only single ion trapping events are useful."[72] In order to avoid 'empty' or multiple ion trapping events, the ion current must be carefully regulated to maximize the number of events containing only a single ion.[73] However, even under optimum conditions, a single ion is trapped in only 37% of measurements. This means that nearly two-thirds of all acquisition time is wasted and a reasonably balanced mass histogram of ~6700 ions and 100 ms trapping periods takes about 30 min to acquire.[72] Higher resolution data or complex samples requiring higher ion counts extend total measurement times further. While faster than other high accuracy single ion MS techniques, these CDMS experiments are still significantly slower than ensemble MS measurements.

Chapters 3 and 4 detail multiplexing methods used to increase CDMS analysis speed without reducing the mass accuracy of each measurement. In contrast to simulations that suggest ion-ion interactions significant perturb ion oscillation frequencies and overall measurement accuracy,[74] Chapter 3 demonstrates that up to 13 simultaneously trapped ions can be individually measured without measurable degradation in mass accuracy compared to measurements where only a single ion was trapped. Overall, an order of magnitude reduction in experiment time is demonstrated. The data analysis methods necessary to simultaneously analyze multiple ion signals in a single trapping event are also discussed. Chapter 4 more thoroughly discusses the maximum multiplexing possible using current instrumentation. Simulations of FT-CDMS data using variable ion mass, charge, and energy are used to determine the optimum number of simultaneously trapped ions to maximize data acquisition efficiency. Compared to single ion only CDMS, analyte dependent improvements in data acquisition speed ranging from ~50x to ~150x may be possible to achieve, which would reduce the measurement time of a sample to less than 1 min.

1.4 Applications of Charge Detection Mass Spectrometry

1.4.1 Polymer of Charge Detection Mass Spectrometry

High molecular weight synthetic polymers and nanoparticles are challenging to analyze using ESI and ensemble MS techniques owing to the large number of different molecular masses typically present in single sample. This intrinsic heterogeneity ultimately results in unresolved charge states and has limited conventional ESI-based MS analysis of polymer molecules to masses less than ~40 kDa.[17–19] In contrast, CDMS has been used to obtain the masses of synthetic polymers such as polyethylene glycol (PEG) weighing up to ~30 MDa,[61,67,75,76] ~100 MDa amphiphilic block copolymers,[77] ~300 MDa polystyrene nanospheres,[60,78] and composite nanoparticles weighing up to ~50 GDa.[79–82] These samples typically have broad mass distributions with widths that can also be characterized by CDMS, which can be useful in understanding the heterogeneity inherent in polymerization processes and other polymer properties. CDMS methods have been used to measure the m/z and velocity of nanoparticle ions before and after impact with a surface, making it possible to characterize the collision elasticity and scattering trajectories.[83,84] Individual PEG ions trapped in a CDMS instrument have been investigated with infrared multiple photon dissociation and information about ion heating and fragmentation was obtained by monitoring the charge of the ion during the irradiation/trapping period.[61,76] However, the mass of the fragment

ions could not be measured due to changes in ion energy associated with each fragmentation event. Using an energy measurement method similar to the one described in Chapter 2, the mass and charge of a ~8 MDa PEG ion was monitored over the course of 4 s trapping period and six successive fragmentation events were observed.[67] The extent of solvent evaporation and energy lost to collisions with background gas throughout the trapping period was also monitored and used to obtain information about the initial and fragmented PEG ion structure.[67] In Chapter 2, the rate of energy loss to background collisions for both a ~3 MDa and a ~4 MDa PEG ion was monitored over a 500 ms period and used to determine approximate cross sections for each ion. Surprisingly, the lower mass ion exhibited a greater rate of energy loss consistent with a larger cross section, a result that suggests that these large polymers can take on a wide variety of conformations. In general, the robustness of CDMS to highly heterogeneous, polydisperse samples make the technique a uniquely powerful tool in the characterization of large polymers and nanoparticles.

1.4.2 Native MS of Large Biomolecules

Sample heterogeneity generally increases with analyte mass in native MS. Thus, ensemble MS techniques that rely on resolvable charge states in a m/z spectrum for mass measurement are increasingly limited at high masses. Poor resolution as a result of the intrinsic heterogeneity of sample and extrinsic factors such as the extent of analyte desolvation and adduction can be countered by extensive analyte purification, thorough buffer exchange, and activating instrumental conditions. Using these methods, mass measurements of homogeneous virus capsids weighing as much as 18 MDa have been demonstrated.[14] In these cases, the high mass measuring accuracy available in ensemble MS is a distinct advantage. However, more typical solution conditions and less pure mixtures of analytes can make mass measurements difficult or even impossible using ensemble MS even at significantly lower mass.

Native CDMS measurements of small proteins and protein complexes have been performed to demonstrate limits of detection and for calibration purposes, but these measurements are typically outperformed in mass resolution and accuracy by ensemble MS techniques. However, because CDMS measurements do not rely on resolving charge states in m/z space, the technique is well suited to the analysis of high-mass (>1 MDa) biomolecules and heterogeneous mixtures. Measurements of the masses of viruses and viral capsids up to 50 MDa have been routinely accomplished using CDMS.[55,85–93] CDMS analyses have also provided insight into virus assembly and disassembly mechanisms,[94,95] including time-dependent measurements of the assembly process.[96] Samples of more naturally heterogeneous biomolecules, such as DNA,[54,58,97,98] amyloid fibrils,[99,100] lipoproteins,[101] and exosomes[102] have also been characterized using CDMS. In Chapter 3, individual ions of ribulose-1,5-bisphosphate carboxylase/oxygenase (RuBisCO) and its aggregates are measured using native CDMS. This analysis includes the measurement of the loss of a minimally charged single protein subunit from the RuBisCO protein complex after hundreds of milliseconds, a fragmentation mechanism not typically observed in collision induced dissociation experiments using conventional MS techniques that require rapid dissociation processes. Chapter 5 includes the measurement of the bacteriophage MS2 virus-like particles with variable cargo loading using CDMS and at least two distinct masses within a heterogeneous sample are identified.

1.4.3 Nanodrop Charging in Electrospray Ionization

The exact mechanism(s) by which gaseous ions are produced in ESI is still an active matter of debate. In ESI, highly charged droplets shrink via evaporation of the volatile solvent. As a droplet decreases in size, the charge-charge repulsion at the surface of the droplet increases, ultimately exceeding the ability of the droplet to remain intact and a Coulombically-driven fission event occurs. This eventuality was first formalized by Lord Rayleigh in the Rayleigh Equation (1.2):[103]

$$Z_R = 8\pi(\varepsilon_0 \gamma R^3)^{1/2} \qquad (1.2)$$

where the Rayleigh fission limit charge, Z_R, is related to the surface tension of the solvent, γ, and droplet radius, R, with ε_0 as the permittivity of free space. Fission events for levitated large droplets (>1 μm) have been observed using phase Doppler interferometry[104] and high-speed microscopy.[105] However, the fate of smaller droplets (10 – 100's of nm) generated by these fission events is still uncertain because they are too small to be probed using optical techniques. Two long-standing models, the ion evaporation model (IEM) and the charge residue model (CRM) have been used to explain the fate of these of these nanodrops. The IEM, which predicts the emission of minimally solvated ions from the surface of the droplet, is favored for the ionization of small molecules.[106,107] The CRM predicts that Rayleigh fission-like events occur until a small droplet approaching the size of the analyte is formed, followed by the evaporation of the remaining solvent and subsequent condensation of the remaining droplet charge onto to the analyte molecule(s).[108] The CRM is the favored mechanism in native MS because the charge states observed for large proteins and macromolecular complexes follow the trend in charging predicted by the Rayleigh charge on a droplet of similar size to the analyte.[109]

The ability of ESI to kinetically trap the solution-phase structure for even weakly bound, non-covalent macromolecular complexes has led to numerous research applications, particularly with respect to large biomolecules. Studies investigating complexes consisting of proteins, nucleotides, and lipids[110–115] and their respective stoichiometries,[13,116,117] assembly pathways,[118,119] binding affinities,[120] and topologies[121,122] have been enabled by ESI. For larger molecules, some structural changes, such as compaction, have been observed after ions have transitioned into the gas phase,[123] casting some doubt on the preservation of the solution phase structure of these macromolecules. However, this is also a matter of ongoing investigation and debate.[124]

Chapter 5 demonstrates the use of CDMS to measure a broad distribution of nanodrop masses (1-10 MDa) and sizes (15-32 nm) originating from aqueous solutions of various volatile and non-volatile solutes. The extent of nanodrop charging observed is dependent on the original solution identity and nanodrop charging relative to the Rayleigh limit generally decreases with decreased solute ion solvation energy. Discharging events corresponding to singly charged ion emission (an IEM process) are directly observed. MS2 ions originating from solutions containing significant concentrations of non-volatile salts exhibit differences in adduction and overall charge when compared to ions generated from the volatile buffer solutions typically preferred in native

MS. This phenomenon is important to consider because understanding the biologically relevant structure and function of a biomolecule is a primary objective of native MS experiments. Evidence for the solution-phase compaction of the MS2 capsid inside of the nanodrop prior to gaseous ion formation is also presented.

1.5 References

(1) Loo, J. A.; Edmonds, C. G.; Smith, R. D. Tandem Mass Spectrometry of Very Large Molecules: Serum Albumin Sequence Information from Multiply Charged Ions Formed by Electrospray Ionization. *Anal. Chem.* **1991**, *63* (21), 2488–2499.

(2) Meier, F.; Geyer, P. E.; Virreira Winter, S.; Cox, J.; Mann, M. BoxCar Acquisition Method Enables Single-Shot Proteomics at a Depth of 10,000 Proteins in 100 Minutes. *Nat. Methods* **2018**, *15* (6), 440–448.

(3) Ganem, B.; Li, Y. T.; Henion, J. D. Detection of Noncovalent Receptor-Ligand Complexes by Mass Spectrometry. *J. Am. Chem. Soc.* **1991**, *113* (16), 6294–6296.

(4) Katta, V.; Chait, B. T. Observation of the Heme—Globin Complex in Native Myoglobin by Electrospray-Ionization Mass Spectrometry. *J. Am. Chem. Soc.* **1991**, *113* (22), 8534–8535.

(5) Clemmer, D. E.; Hudgins, R. R.; Jarrold, M. F. Naked Protein Conformations: Cytochrome c in the Gas Phase. *J. Am. Chem. Soc.* **1995**, *117* (40), 10141–10142.

(6) Myung, S.; Badman, E. R.; Lee, Y. J.; Clemmer, D. E. Structural Transitions of Electrosprayed Ubiquitin Ions Stored in an Ion Trap over ~10 Ms to 30 S. *J. Phys. Chem. A* **2002**, *106* (42), 9976–9982.

(7) Van Den Heuvel, R. H. H.; Heck, A. J. R. Native Protein Mass Spectrometry: From Intact Oligomers to Functional Machineries. *Curr. Opin. Chem. Biol.* **2004**, *8* (5), 519–526.

(8) Ruotolo, B. T.; Giles, K.; Campuzano, I.; Sandercock, A. M.; Bateman, R. H.; Robinson, C. V. Evidence for Macromolecular Protein Rings in the Absence of Bulk Water. *Science (80-.).* **2005**, *310* (5754), 1658–1661.

(9) Voronina, L.; Rizzo, T. R. Spectroscopic Studies of Kinetically Trapped Conformations in the Gas Phase: The Case of Triply Protonated Bradykinin. *Phys. Chem. Chem. Phys.* **2015**, *17* (39), 25828–25836.

(10) Synowsky, S. A.; van den Heuvel, R. H. H.; Mohammed, S.; Pijnappel, W. W. M. P.; Heck, A. J. R. Probing Genuine Strong Interactions and Post-Translational Modifications in the Heterogeneous Yeast Exosome Protein Complex. *Mol. Cell. Proteomics* **2006**, *5* (9), 1581–1592.

(11) Ryan, C. M.; Souda, P.; Bassilian, S.; Ujwal, R.; Zhang, J.; Abramson, J.; Ping, P.; Durazo, A.; Bowie, J. U.; Hasan, S. S.; Baniulis, D.; Cramer, W. A.; Faull, K. F.; Whitelegge, J. P. Post-Translational Modifications of Integral Membrane Proteins Resolved by Top-down Fourier Transform Mass Spectrometry with Collisionally Activated Dissociation. *Mol. Cell. Proteomics* **2010**, *9* (5), 791–803.

(12) Catherman, A. D.; Skinner, O. S.; Kelleher, N. L. Top Down Proteomics: Facts and

Perspectives. *Biochem. Biophys. Res. Commun.* **2014**, *445* (4), 683–693.

(13) Loo, J. A. Electrospray Ionization Mass Spectrometry: A Technology for Studying Noncovalent Macromolecular Complexes. *Int. J. Mass Spectrom.* **2000**, *200* (1–3), 175–186.

(14) Snijder, J.; Rose, R. J.; Veesler, D.; Johnson, J. E.; Heck, A. J. R. Studying 18 MDa Virus Assemblies with Native Mass Spectrometry. *Angew. Chemie - Int. Ed.* **2013**, *52* (14), 4020–4023.

(15) Lössl, P.; Snijder, J.; Heck, A. J. R. Boundaries of Mass Resolution in Native Mass Spectrometry. *J. Am. Soc. Mass Spectrom.* **2014**, *25* (6), 906–917.

(16) Weiss, V. U.; Bereszczazk, J. Z.; Havlik, M.; Kallinger, P.; Gösler, I.; Kumar, M.; Blaas, D.; Marchetti-Deschmann, M.; Heck, A. J. R.; Szymanski, W. W.; Allmaier, G. Analysis of a Common Cold Virus and Its Subviral Particles by Gas-Phase Electrophoretic Mobility Molecular Analysis and Native Mass Spectrometry. *Anal. Chem.* **2015**, *87* (17), 8709–8717.

(17) Malmstrøm, J. Characterization of 40 KDa Poly(Ethylene Glycol) Polymers by Proton Transfer Reaction QTOF Mass Spectrometry and 1H-NMR Spectroscopy. *Anal. Bioanal. Chem.* **2012**, *403* (4), 1167–1177.

(18) Robb, D. B.; Brown, J. M.; Morris, M.; Blades, M. W. Method of Atmospheric Pressure Charge Stripping for Electrospray Ionization Mass Spectrometry and Its Application for the Analysis of Large Poly(Ethylene Glycol)S. *Anal. Chem.* **2014**, *86* (19), 9644–9652.

(19) Ozeki, Y.; Omae, M.; Kitagawa, S.; Ohtani, H. Electrospray Ionization-Ion Mobility Spectrometry-High Resolution Tandem Mass Spectrometry with Collision-Induced Charge Stripping for the Analysis of Highly Multiply Charged Intact Polymers. *Analyst* **2019**, *144* (10), 3428–3435.

(20) Chang, H. C. Ultrahigh-Mass Mass Spectrometry of Single Biomolecules and Bioparticles. *Annu. Rev. Anal. Chem.* **2009**, *2*, 169–185.

(21) Keifer, D. Z.; Jarrold, M. F. Single-Molecule Mass Spectrometry. *Mass Spectrom. Rev.* **2017**, *36* (6), 715–733.

(22) Fraser, G. W. The Ion Detection Efficiency of Microchannel Plates (MCPs). *Int. J. Mass Spectrom.* **2002**, *215* (1–3), 13–30.

(23) Chen, X.; Westphall, M. S.; Smith, L. M. Mass Spectrometric Analysis of DNA Mixtures: Instrumental Effects Responsible for Decreased Sensitivity with Increasing Mass. *Anal. Chem.* **2003**, *75* (21), 5944–5952.

(24) Twerenbold, D. Biopolymer Mass Spectrometer with Cryogenic Particle Detectors. *Nucl. Instruments Methods Phys. Res. Sect. A Accel. Spectrometers, Detect. Assoc. Equip.* **1996**, *370* (1), 253–255.

(25) Hilton, G. C.; Martinis, J. M.; Wollman, D. A.; Irwin, K. D.; Dulcie, L. L.; Gerber, D.; Gillevet, P. M.; Twerenbold, D. Impact Energy Measurement in Time-of-Flight Mass Spectrometry with Cryogenic Microcalorimeters. *Nature* **1998**, *391* (6668), 672–675.

(26) Frank, M.; Labov, S. E.; Westmacott, G.; Benner, W. H. Energy-Sensitive Cryogenic Detectors for High-Mass Biomolecule Mass Spectrometry. *Mass Spectrom. Rev.* **1999**, *18* (3–4), 155–186.

(27) Wenzel, R. J.; Matter, U.; Schultheis, L.; Zenobi, R. Analysis of Megadalton Ions Using Cryodetection MALDI Time-of-Flight Mass Spectrometry. *Anal. Chem.* **2005**, *77* (14), 4329–4337.

(28) Aksenov, A. A.; Bier, M. E. The Analysis of Polystyrene and Polystyrene Aggregates into the Mega Dalton Mass Range by Cryodetection MALDI TOF MS. *J. Am. Soc. Mass Spectrom.* **2008**, *19* (2), 219–230.

(29) Hanay, M. S.; Kelber, S. I.; O'Connell, C. D.; Mulvaney, P.; Sader, J. E.; Roukes, M. L. Inertial Imaging with Nanomechanical Systems. *Nat. Nanotechnol.* **2015**, *10* (4), 339–344.

(30) Sage, E.; Brenac, A.; Alava, T.; Morel, R.; Dupré, C.; Hanay, M. S.; Roukes, M. L.; Duraffourg, L.; Masselon, C.; Hentz, S. Neutral Particle Mass Spectrometry with Nanomechanical Systems. *Nat. Commun.* **2015**, *6* (1), 1–5.

(31) Gil-Santos, E.; Ramos, D.; Martínez, J.; Fernández-Regúlez, M.; García, R.; San Paulo, Á.; Calleja, M.; Tamayo, J. Nanomechanical Mass Sensing and Stiffness Spectrometry Based on Two-Dimensional Vibrations of Resonant Nanowires. *Nat. Nanotechnol.* **2010**, *5* (9), 641–645.

(32) Hanay, M. S.; Kelber, S.; Naik, A. K.; Chi, D.; Hentz, S.; Bullard, E. C.; Colinet, E.; Duraffourg, L.; Roukes, M. L. Single-Protein Nanomechanical Mass Spectrometry in Real Time. *Nat. Nanotechnol.* **2012**, *7* (9), 602–608.

(33) Dohn, S.; Svendsen, W.; Boisen, A.; Hansen, O. Mass and Position Determination of Attached Particles on Cantilever Based Mass Sensors. *Rev. Sci. Instrum.* **2007**, *78* (10), 103303.

(34) Sader, J. E.; Hanay, M. S.; Neumann, A. P.; Roukes, M. L. Mass Spectrometry Using Nanomechanical Systems: Beyond the Point-Mass Approximation. *Nano Lett.* **2018**, *18* (3), 1608–1614.

(35) Schlemmer, S.; Illemann, J.; Wellert, S.; Gerlich, D. Nondestructive High-Resolution and Absolute Mass Determination of Single Charged Particles in a Three-Dimensional Quadrupole Trap. *J. Appl. Phys.* **2001**, *90* (10), 5410–5418.

(36) Howder, C. R.; Bell, D. M.; Anderson, S. L. Optically Detected, Single Nanoparticle Mass Spectrometer with Pre-Filtered Electrospray Nanoparticle Source. *Rev. Sci. Instrum.* **2014**, *85* (1), 014104.

(37) Smith, R. D.; Cheng, X.; Brace, J. E.; Hofstadler, S. A.; Anderson, G. A. Trapping, Detection and Reaction of Very Large Single Molecular Ions by Mass Spectrometry. *Nature* **1994**, *369* (6476), 137–139.

(38) Bruce, J. E.; Cheng, X.; Bakhtiar, R.; Wu, Q.; Hofstadler, S. A.; Anderson, G. A.; Smith, R. D. Trapping, Detection, and Mass Measurement of Individual Ions in a Fourier Transform Ion Cyclotron Resonance Mass Spectrometer. *J. Am. Chem. Soc.* **1994**, *116* (17), 7839–7847.

(39) Cheng, X.; Bakhtiar, R.; Van Orden, S.; Smith, R. D. Charge-State Shifting of Individual Multiply-Charged Ions of Bovine Albumin Dimer and Molecular Weight Determination Using an Individual-Ion Approach. *Anal. Chem.* **1994**, *66* (13), 2084–2087.

(40) Marshall, A. G.; Hendrickson, C. L.; Jackson, G. S. Fourier Transform Ion Cyclotron Resonance Mass Spectrometry: A Primer. *Mass Spectrom. Rev.* **1998**, *17* (1), 1–35.

(41) Chen, R.; Cheng, X.; Mitchell, D. W.; Hofstadler, S. A.; Wu, Q.; Rockwood, A. L.; Sherman, M. G.; Smith, R. D. Trapping, Detection, and Mass Determination of Coliphage T4 DNA Ions of 108 DA by Electrospray Ionization Fourier Transform Ion Cyclotron Resonance Mass Spectrometry. *Anal. Chem.* **1995**, *67* (7), 1159–1163.

(42) Chen, R.; Wu, Q.; Mitchell, D. W.; Hofstadler, S. A.; Rockwood, A. L.; Smith, R. D. Direct Charge Number and Molecular Weight Determination of Large Individual Ions by Electrospray Ionization Fourier Transform Ion Cyclotron Resonance Mass Spectrometry. *Anal. Chem.* **1994**, *66* (22), 3964–3969.

(43) Rose, R. J.; Damoc, E.; Denisov, E.; Makarov, A.; Heck, A. J. R. High-Sensitivity Orbitrap Mass Analysis of Intact Macromolecular Assemblies. *Nat. Methods* **2012**, *9* (11), 1084–1086.

(44) Wörner, T. P.; Snijder, J.; Bennett, A.; Agbandje-McKenna, M.; Makarov, A. A.; Heck, A. J. R. Resolving Heterogeneous Macromolecular Assemblies by Orbitrap-Based Single-Particle Charge Detection Mass Spectrometry. *Nat. Methods* **2020**, *17* (4), 395–398.

(45) Kafader, J. O.; Melani, R. D.; Senko, M. W.; Makarov, A. A.; Kelleher, N. L.; Compton, P. D. Measurement of Individual Ions Sharply Increases the Resolution of Orbitrap Mass Spectra of Proteins. *Anal. Chem.* **2019**, *91* (4), 2776–2783.

(46) Kafader, J. O.; Beu, S. C.; Early, B. P.; Melani, R. D.; Durbin, K. R.; Zabrouskov, V.; Makarov, A. A.; Maze, J. T.; Shinholt, D. L.; Yip, P. F.; Kelleher, N. L.; Compton, P. D.; Senko, M. W. STORI Plots Enable Accurate Tracking of Individual Ion Signals. *J. Am. Soc. Mass Spectrom.* **2019**, *30* (11), 2200–2203.

(47) Kafader, J. O.; Melani, R. D.; Durbin, K. R.; Ikwuagwu, B.; Early, B. P.; Fellers, R. T.; Beu, S. C.; Zabrouskov, V.; Makarov, A. A.; Maze, J. T.; Shinholt, D. L.; Yip, P. F.; Tullman-Ercek, D.; Senko, M. W.; Compton, P. D.; Kelleher, N. L. Multiplexed Mass Spectrometry of Individual Ions Improves Measurement of Proteoforms and Their Complexes. *Nat. Methods* **2020**, *17* (4), 391–394.

(48) Kafader, J. O.; Durbin, K. R.; Melani, R. D.; Des Soye, B. J.; Schachner, L. F.; Senko, M. W.; Compton, P. D.; Kelleher, N. L. Individual Ion Mass Spectrometry Enhances the Sensitivity and Sequence Coverage of Top-Down Mass Spectrometry. *J. Proteome Res.* **2020**, *19* (3), 1346–1350.

(49) Weinheimer, A. J. The Charge Induced on a Conducting Cylinder by a Point Charge and Its Application to the Measurement of Charge on Precipitation. *J. Atmos. Ocean. Technol.* **1988**, *5* (2), 298–304.

(50) Shelton, H.; Hendricks, C. D.; Wuerker, R. F. Electrostatic Acceleration of Microparticles to Hypervelocities. *J. Appl. Phys.* **1960**, *31* (7), 1243–1246.

(51) Hendricks, C. D. Charged Droplet Experiments. *J. Colloid Sci.* **1962**, *17* (3), 249–259.

(52) Keaton, P. W.; Idzorek, G. C.; Rowton, L. J.; Seagrave, J. D.; Stradling, G. L.; Bergeson, S. D.; Collopy, M. T.; Curling, H. L.; McColl, D. B.; Smith, J. D. A Hypervelocity - Microparticle - Impacts Laboratory with 100-Km/s Projectiles. *Int. J. Impact Eng.* **1990**, *10* (1–4), 295–308.

(53) Stradling, G. L.; Idzorek, G. C.; Shafer, B. P.; Curling, H. L.; Collopy, M. T.; Blossom, A. A. H.; Fuerstenau, S. Ultra-High Velocity Impacts: Cratering Studies of Microscopic Impacts from 3 Km/s to 30 Km/S. *Int. J. Impact Eng.* **1993**, *14* (1–4), 719–727.

(54) Fuerstenau, S. D.; Benner, W. H. Molecular Weight Determination of Megadalton DNA Electrospray Ions Using Charge Detection Time-of-flight Mass Spectrometry. *Rapid Commun. Mass Spectrom.* **1995**, *9* (15), 1528–1538.

(55) Fuerstenau, S. D.; Benner, W. H.; Thomas, J. J.; Brugidou, C.; Bothner, B.; Siuzdak, G. Mass Spectrometry of an Intact Virus. *Angew. Chemie - Int. Ed.* **2001**, *40* (3), 541–544.

(56) Smith, J. W.; Siegel, E. E.; Maze, J. T.; Jarrold, M. F. Image Charge Detection Mass Spectrometry: Pushing the Envelope with Sensitivity and Accuracy. *Anal. Chem.* **2011**, *83* (3), 950–956.

(57) Barney, B. L.; Daly, R. T.; Austin, D. E. A Multi-Stage Image Charge Detector Made from Printed Circuit Boards. *Rev. Sci. Instrum.* **2013**, *84* (11), 114101.

(58) Benner, W. H. A Gated Electrostatic Ion Trap to Repetitiously Measure the Charge and m/z of Large Electrospray Ions. *Anal. Chem.* **1997**, *69* (20), 4162–4168.

(59) Contino, N. C.; Jarrold, M. F. Charge Detection Mass Spectrometry for Single Ions with a Limit of Detection of 30 Charges. *Int. J. Mass Spectrom.* **2013**, *345–347*, 153–159.

(60) Elliott, A. G.; Merenbloom, S. I.; Chakrabarty, S.; Williams, E. R. Single Particle Analyzer of Mass: A Charge Detection Mass Spectrometer with a Multi-Detector Electrostatic Ion Trap. *Int. J. Mass Spectrom.* **2017**, *414*, 45–55.

(61) Doussineau, T.; Yu Bao, C.; Clavier, C.; Dagany, X.; Kerleroux, M.; Antoine, R.; Dugourd, P. Infrared Multiphoton Dissociation Tandem Charge Detection-Mass Spectrometry of Single Megadalton Electrosprayed Ions. *Rev. Sci. Instrum.* **2011**, *82* (8), 084104.

(62) Hogan, J. A.; Jarrold, M. F. Optimized Electrostatic Linear Ion Trap for Charge Detection Mass Spectrometry. *J. Am. Soc. Mass Spectrom.* **2018**, *29* (10), 2086–2095.

(63) Contino, N. C.; Pierson, E. E.; Keifer, D. Z.; Jarrold, M. F. Charge Detection Mass Spectrometry with Resolved Charge States. *J. Am. Soc. Mass Spectrom.* **2013**, *24* (1), 101–108.

(64) Pierson, E. E.; Contino, N. C.; Keifer, D. Z.; Jarrold, M. F. Charge Detection Mass Spectrometry for Single Ions with an Uncertainty in the Charge Measurement of 0.65 E. *J. Am. Soc. Mass Spectrom.* **2015**, *26* (7), 1213–1220.

(65) Todd, A. R.; Alexander, A. W.; Jarrold, M. F. Implementation of a Charge-Sensitive Amplifier without a Feedback Resistor for Charge Detection Mass Spectrometry Reduces

Noise and Enables Detection of Individual Ions Carrying a Single Charge. *J. Am. Soc. Mass Spectrom.* **2020**, *31* (1), 146–154.

(66) Keifer, D. Z.; Shinholt, D. L.; Jarrold, M. F. Charge Detection Mass Spectrometry with Almost Perfect Charge Accuracy. *Anal. Chem.* **2015**, *87* (20), 10330–10337.

(67) Elliott, A. G.; Harper, C. C.; Lin, H. W.; Williams, E. R. Mass, Mobility and MSN Measurements of Single Ions Using Charge Detection Mass Spectrometry. *Analyst* **2017**, *142* (15), 2760–2769.

(68) Todd, A. R.; Jarrold, M. F. Dynamic Calibration Enables High-Accuracy Charge Measurements on Individual Ions for Charge Detection Mass Spectrometry. *J. Am. Soc. Mass Spectrom.* **2020**, *31* (6), 1241–1248.

(69) Harper, C. C.; Elliott, A. G.; Lin, H. W.; Williams, E. R. Determining Energies and Cross Sections of Individual Ions Using Higher-Order Harmonics in Fourier Transform Charge Detection Mass Spectrometry (FT-CDMS). *J. Am. Soc. Mass Spectrom.* **2018**, *29* (9), 1861–1869.

(70) Elliott, A. G.; Harper, C. C.; Lin, H. W.; Williams, E. R. Effects of Individual Ion Energies on Charge Measurements in Fourier Transform Charge Detection Mass Spectrometry (FT-CDMS). *J. Am. Soc. Mass Spectrom.* **2019**, *30* (6), 946–955.

(71) Todd, A. R.; Barnes, L. F.; Young, K.; Zlotnick, A.; Jarrold, M. F. Higher Resolution Charge Detection Mass Spectrometry. *Anal. Chem.* **2020**, *92* (16), 11357–11364.

(72) Keifer, D. Z.; Pierson, E. E.; Jarrold, M. F. Charge Detection Mass Spectrometry: Weighing Heavier Things. *Analyst* **2017**, *142* (10), 1654–1671.

(73) Draper, B. E.; Jarrold, M. F. Real-Time Analysis and Signal Optimization for Charge Detection Mass Spectrometry. *J. Am. Soc. Mass Spectrom.* **2019**, *30* (6), 898–904.

(74) Botamanenko, D. Y.; Jarrold, M. F. Ion-Ion Interactions in Charge Detection Mass Spectrometry. *J. Am. Soc. Mass Spectrom.* **2019**, *30* (12), 2741–2749.

(75) Doussineau, T.; Kerleroux, M.; Dagany, X.; Clavier, C.; Barbaire, M.; Maurelli, J.; Antoine, R.; Dugourd, P. Charging Megadalton Poly(Ethylene Oxide)s by Electrospray Ionization. A Charge Detection Mass Spectrometry Study. *Rapid Commun. Mass Spectrom.* **2011**, *25* (5), 617–623.

(76) Halim, M. A.; Clavier, C.; Dagany, X.; Kerleroux, M.; Dugourd, P.; Dunbar, R. C.; Antoine, R. Infrared Laser Dissociation of Single Megadalton Polymer Ions in a Gated Electrostatic Ion Trap: The Added Value of Statistical Analysis of Individual Events. *Phys. Chem. Chem. Phys.* **2018**, *20* (17), 11959–11966.

(77) Doussineau, T.; Bao, C. Y.; Antoine, R.; Dugourd, P.; Zhang, W.; D'Agosto, F.; Charleux, B. Direct Molar Mass Determination of Self-Assembled Amphiphilic Block Copolymer Nanoobjects Using Electrospray-Charge Detection Mass Spectrometry. *ACS Macro Lett.* **2012**, *1* (3), 414–417.

(78) Draper, B. E.; Anthony, S. N.; Jarrold, M. F. The FUNPET—a New Hybrid Ion Funnel-Ion Carpet Atmospheric Pressure Interface for the Simultaneous Transmission of a Broad Mass

Range. *J. Am. Soc. Mass Spectrom.* **2018**, *29* (11), 2160–2172.

(79) Doussineau, T.; Santacreu, M.; Antoine, R.; Dugourd, P.; Zhang, W.; Chaduc, I.; Lansalot, M.; D'Agosto, F.; Charleux, B. The Charging of Micellar Nanoparticles in Electrospray Ionization. *ChemPhysChem* **2013**, *14* (3), 603–609.

(80) Ouadah, N.; Doussineau, T.; Hamada, T.; Dugourd, P.; Bordes, C.; Antoine, R. Correlation between the Charge of Polymer Particles in Solution and in the Gas Phase Investigated by Zeta-Potential Measurements and Electrospray Ionization Mass Spectrometry. *Langmuir* **2013**, *29* (46), 14074–14081.

(81) Doussineau, T.; Désert, A.; Lambert, O.; Taveau, J. C.; Lansalot, M.; Dugourd, P.; Bourgeat-Lami, E.; Ravaine, S.; Duguet, E.; Antoine, R. Charge Detection Mass Spectrometry for the Characterization of Mass and Surface Area of Composite Nanoparticles. *J. Phys. Chem. C* **2015**, *119* (20), 10844–10849.

(82) Viodé, A.; Dagany, X.; Kerleroux, M.; Dugourd, P.; Doussineau, T.; Charles, L.; Antoine, R. Coupling of Size-Exclusion Chromatography with Electrospray Ionization Charge-Detection Mass Spectrometry for the Characterization of Synthetic Polymers of Ultra-High Molar Mass. *Rapid Commun. Mass Spectrom.* **2016**, *30* (1), 132–136.

(83) Adamson, B. D.; Miller, M. E. C.; Continetti, R. E. The Aerosol Impact Spectrometer: A Versatile Platform for Studying the Velocity Dependence of Nanoparticle-Surface Impact Phenomena. *EPJ Tech. Instrum.* **2017**, *4* (1), 1–17.

(84) Miller, M. E. C.; Mezher, M.; Continetti, R. E. Tapered Image Charge Detector for Measuring Velocity Distributions of Submicrometer Particle Scattering. *Rev. Sci. Instrum.* **2020**, *91* (6), 063305.

(85) Pierson, E. E.; Keifer, D. Z.; Kukreja, A. A.; Wang, J. C. Y.; Zlotnick, A.; Jarrold, M. F. Charge Detection Mass Spectrometry Identifies Preferred Non-Icosahedral Polymorphs in the Self-Assembly of Woodchuck Hepatitis Virus Capsids. *J. Mol. Biol.* **2016**, *428* (2), 292–300.

(86) Keifer, D. Z.; Pierson, E. E.; Hogan, J. A.; Bedwell, G. J.; Prevelige, P. E.; Jarrold, M. F. Charge Detection Mass Spectrometry of Bacteriophage P22 Procapsid Distributions above 20 MDa. *Rapid Commun. Mass Spectrom.* **2014**, *28* (5), 483–488.

(87) Pierson, E. E.; Keifer, D. Z.; Asokan, A.; Jarrold, M. F. Resolving Adeno-Associated Viral Particle Diversity with Charge Detection Mass Spectrometry. *Anal. Chem.* **2016**, *88* (13), 6718–6725.

(88) Keifer, D. Z.; Motwani, T.; Teschke, C. M.; Jarrold, M. F. Acquiring Structural Information on Virus Particles with Charge Detection Mass Spectrometry. *J. Am. Soc. Mass Spectrom.* **2016**, *27* (6), 1028–1036.

(89) Keifer, D. Z.; Motwani, T.; Teschke, C. M.; Jarrold, M. F. Measurement of the Accurate Mass of a 50 MDa Infectious Virus. *Rapid Commun. Mass Spectrom.* **2016**, *30* (17), 1957–1962.

(90) Dunbar, C. A.; Callaway, H. M.; Parrish, C. R.; Jarrold, M. F. Probing Antibody Binding to Canine Parvovirus with Charge Detection Mass Spectrometry. *J. Am. Chem. Soc.* **2018**,

140 (46), 15701–15711.

(91) Keifer, D. Z.; Alexander, A. W.; Jarrold, M. F. Spontaneous Mass and Charge Losses from Single Multi-Megadalton Ions Studied by Charge Detection Mass Spectrometry. *J. Am. Soc. Mass Spectrom.* **2017**, *28* (3), 498–506.

(92) O'Connor, D. M.; Lutomski, C.; Jarrold, M. F.; Boulis, N. M.; Donsante, A. Lot-to-Lot Variation in Adeno-Associated Virus Serotype 9 (AAV9) Preparations. *Hum. Gene Ther. Methods* **2019**, *30* (6), 214–225.

(93) Dunbar, C. A.; Rayaprolu, V.; Wang, J. C. Y.; Brown, C. J.; Leishman, E.; Jones-Burrage, S.; Trinidad, J. C.; Bradshaw, H. B.; Clemmer, D. E.; Mukhopadhyay, S.; Jarrold, M. F. Dissecting the Components of Sindbis Virus from Arthropod and Vertebrate Hosts: Implications for Infectivity Differences. *ACS Infect. Dis.* **2019**, *5* (6), 892–902.

(94) Bond, K. M.; Lyktey, N. A.; Tsvetkova, I. B. Disassembly Intermediates of the Brome Mosaic Virus Identified by Charge Detection Mass Spectrometry. *J. Phys. Chem. B* **2020**, *124* (11), 2124–2131.

(95) Lutomski, C. A.; Lyktey, N. A.; Zhao, Z.; Pierson, E. E.; Zlotnick, A.; Jarrold, M. F. Hepatitis B Virus Capsid Completion Occurs through Error Correction. *J. Am. Chem. Soc.* **2017**, *139* (46), 16932–16938.

(96) Lutomski, C. A.; Lyktey, N. A.; Pierson, E. E.; Zhao, Z.; Zlotnick, A.; Jarrold, M. F. Multiple Pathways in Capsid Assembly. *J. Am. Chem. Soc.* **2018**, *140* (17), 5784–5790.

(97) Doussineau, T.; Paletto, P.; Dugourd, P.; Antoine, R. Multiphoton Dissociation of Electrosprayed Megadalton-Sized DNA Ions in a Charge-Detection Mass Spectrometer. *J. Am. Soc. Mass Spectrom.* **2014**, *26* (1), 7–13.

(98) Doussineau, T.; Antoine, R.; Santacreu, M.; Dugourd, P. Pushing the Limit of Infrared Multiphoton Dissociation to Megadalton-Size DNA Ions. *J. Phys. Chem. Lett.* **2012**, *3* (16), 2141–2145.

(99) Doussineau, T.; Mathevon, C.; Altamura, L.; Vendrely, C.; Dugourd, P.; Forge, V.; Antoine, R. Mass Determination of Entire Amyloid Fibrils by Using Mass Spectrometry. *Angew. Chemie - Int. Ed.* **2016**, *55* (7), 2340–2344.

(100) Pansieri, J.; Halim, M. A.; Vendrely, C.; Dumoulin, M.; Legrand, F.; Sallanon, M. M.; Chierici, S.; Denti, S.; Dagany, X.; Dugourd, P.; Marquette, C.; Antoine, R.; Forge, V. Mass and Charge Distributions of Amyloid Fibers Involved in Neurodegenerative Diseases: Mapping Heterogeneity and Polymorphism. *Chem. Sci.* **2018**, *9* (10), 2791–2796.

(101) Lutomski, C. A.; Gordon, S. M.; Remaley, A. T.; Jarrold, M. F. Resolution of Lipoprotein Subclasses by Charge Detection Mass Spectrometry. *Anal. Chem.* **2018**, *90* (11), 6353–6356.

(102) Brown, B. A.; Zeng, X.; Todd, A. R.; Barnes, L. F.; Winstone, J. M. A.; Trinidad, J. C.; Novotny, M. V.; Jarrold, M. F.; Clemmer, D. E. Charge Detection Mass Spectrometry Measurements of Exosomes and Other Extracellular Particles Enriched from Bovine Milk. *Anal. Chem.* **2020**, *92* (4), 3285–3292.

(103) Rayleigh, Lord. XX. On the Equilibrium of Liquid Conducting Masses Charged with Electricity. *London, Edinburgh, Dublin Philos. Mag. J. Sci.* **1882**, *14* (87), 184–186.

(104) Smith, J. N.; Flagan, R. C.; Beauchamp, J. L. Droplet Evaporation and Discharge Dynamics in Electrospray Ionization. *J. Phys. Chem. A* **2002**, *106* (42), 9957–9967.

(105) Duft, D.; Achtzehn, T.; Müller, R.; Huber, B. A.; Leisner, T. Coulomb Fission: Rayleigh Jets from Levitated Microdroplets. *Nature* **2003**, *421* (6919), 128.

(106) Iribarne, J. V.; Thomson, B. A. On the Evaporation of Small Ions from Charged Droplets. *J. Chem. Phys.* **1976**, *64* (6), 2287–2294.

(107) Kebarle, P.; Peschke, M. On the Mechanisms by Which the Charged Droplets Produced by Electrospray Lead to Gas Phase Ions. *Anal. Chim. Acta* **2000**, *406* (1), 11–35.

(108) Dole, M.; Mack, L. L.; Hines, R. L.; Chemistry, D. O.; Mobley, R. C.; Ferguson, L. D.; Alice, M. B. Molecular Beams of Macroions. *J. Chem. Phys.* **1968**, *49* (5), 2240–2249.

(109) Fernandez De La Mora, J. Electrospray Ionization of Large Multiply Charged Species Proceeds via Dole's Charged Residue Mechanism. *Anal. Chim. Acta* **2000**, *406* (1), 93–104.

(110) Veenstra, T. D. Electrospray Ionization Mass Spectrometry in the Study of Biomolecular Non-Covalent Interactions. *Biophys. Chem.* **1999**, *79* (2), 63–79.

(111) Ruotolo, B. T.; Benesch, J. L. P.; Sandercock, A. M.; Hyung, S. J.; Robinson, C. V. Ion Mobility-Mass Spectrometry Analysis of Large Protein Complexes. *Nat. Protoc.* **2008**, *3* (7), 1139–1152.

(112) Sharon, M. How Far Can We Go with Structural Mass Spectrometry of Protein Complexes? *J. Am. Soc. Mass Spectrom.* **2010**, *21* (4), 487–500.

(113) Laganowsky, A.; Reading, E.; Allison, T. M.; Ulmschneider, M. B.; Degiacomi, M. T.; Baldwin, A. J.; Robinson, C. V. Membrane Proteins Bind Lipids Selectively to Modulate Their Structure and Function. *Nature* **2014**, *510* (7503), 172–175.

(114) Pedro, L.; Quinn, R. J. Native Mass Spectrometry in Fragment-Based Drug Discovery. *Molecules* **2016**, *21* (8).

(115) Schmidt, C.; Kramer, K.; Urlaub, H. Investigation of Protein-RNA Interactions by Mass Spectrometry-Techniques and Applications. *J. Proteomics* **2012**, *75* (12), 3478–3494.

(116) Heck, A. J. R.; Van Den Heuvel, R. H. H. Investigation of Intact Protein Complexes by Mass Spectrometry. *Mass Spectrom. Rev.* **2004**, *23* (5), 368–389.

(117) Hernández, H.; Robinson, C. V. Determining the Stoichiometry and Interactions of Macromolecular Assemblies from Mass Spectrometry. *Nat. Protoc.* **2007**, *2* (3), 715–726.

(118) Painter, A. J.; Jaya, N.; Basha, E.; Vierling, E.; Robinson, C. V.; Benesch, J. L. P. Real-Time Monitoring of Protein Complexes Reveals Their Quaternary Organization and Dynamics. *Chem. Biol.* **2008**, *15* (3), 246–253.

(119) Kintzer, A. F.; Sterling, H. J.; Tang, I. I.; Abdul-Gader, A.; Miles, A. J.; Wallace, B. A.; Williams, E. R.; Krantz, B. A. Role of the Protective Antigen Octamer in the Molecular

Mechanism of Anthrax Lethal Toxin Stabilization in Plasma. *J. Mol. Biol.* **2010**, *399* (5), 741–758.

(120) Rostom, A. A.; Tame, J. R. H.; Ladbury, J. E.; Robinson, C. V. Specificity and Interactions of the Protein OppA: Partitioning Solvent Binding Effects Using Mass Spectrometry. *J. Mol. Biol.* **2000**, *296* (1), 269–279.

(121) Heck, A. J. R. Native Mass Spectrometry: A Bridge between Interactomics and Structural Biology. *Nat. Methods* **2008**, *5* (11), 927–933.

(122) Sharon, M.; Robinson, C. V. The Role of Mass Spectrometry in Structure Elucidation of Dynamic Protein Complexes. *Annu. Rev. Biochem.* **2007**, *76*, 167–193.

(123) Hogan, C. J.; Ruotolo, B. T.; Robinson, C. V.; Fernandez De La Mora, J. Tandem Differential Mobility Analysis-Mass Spectrometry Reveals Partial Gas-Phase Collapse of the GroEL Complex. *J. Phys. Chem. B* **2011**, *115* (13), 3614–3621.

(124) Leney, A. C.; Heck, A. J. R. Native Mass Spectrometry: What Is in the Name? *J. Am. Soc. Mass Spectrom.* **2017**, *28* (1), 5–13.

Chapter 2

Determining Energies and Cross Sections of Individual Ions using Higher Order Harmonics in Fourier Transform Charge Detection Mass Spectrometry (FT-CDMS)

This chapter is reproduced with permission from:

Conner C. Harper, Andrew G. Elliott, Haw-Wei Lin, and Evan R. Williams

"Determining Energies and Cross Sections of Individual Ions using Higher Order Harmonics in Fourier Transform Charge Detection Mass Spectrometry (FT-CDMS)" *J. Am. Soc. Mass Spectrom.* **2018**, *29* (9), 1861–1869.

© 2018 American Society for Mass Spectrometry

2.1 Abstract

A general method for *in situ* measurements of the energy of individual ions trapped and weighed using charge detection mass spectrometry (CDMS) is described. Highly charged (>300 *e*), individual polyethylene glycol (PEG) ions are trapped and oscillate within an electrostatic trap, producing a time domain signal. A segmented Fourier transform (FT) of this signal yields the temporal evolution of the fundamental and harmonic frequencies of ion motion throughout the 500 ms trap time. The ratio of the fundamental frequency and second harmonic (HAR) depends on the ion energy, which is an essential parameter for measuring ion mass in CDMS. This relationship is calibrated using simulated ion signals and the calibration is compared to the HAR values measured for PEG ion signals where the ion energy was also determined using an independent method that requires that the ions be highly charged (>300 *e*). The mean error of 0.6% between the two measurements indicates that HAR is an accurate means of ion energy determination that does not depend on ion size or charge. The HAR is determined dynamically over the entire trapping period, making it possible to observe the change in ion energy that takes place as solvent evaporates from the ion and collisions with background gas occur. This method makes it possible to measure mass changes, either from solvent evaporation or from molecular fragmentation (MS^n), as well as the cross sections of ions measured using CDMS..

2.2 Introduction

Multiply charged ions of a wide variety of polymers and noncovalent complexes can be formed directly from solution with electrospray ionization (ESI). In conventional mass spectrometry (MS) measurements, the mass-to-charge ratios (m/z) of ensembles of ions are measured and information about the charge states are obtained from the spacings of isotopic peaks

or from spacings in the charge-state distributions of ions of the same mass. Charge-state distributions have been resolved for molecular complexes up to ~20 MDa in size.[1] However, sample heterogeneity and adduction often limit the ability to resolve charge states, making mass measurements difficult or impossible even for much smaller molecules.[2] An alternative to conventional MS techniques that eliminates the problem of sample heterogeneity is to simultaneously measure both the *m*/*z* and charge of individual ions. Single ion techniques have been implemented in Fourier transform ion cyclotron resonance[3,4] and quadrupole ion trap[5–10] instruments to measure the masses of large (MDa) ions. However, these techniques have not gained widespread use due to the long times required for each ion measurement.

Charge detection mass spectrometry (CDMS) has undergone significant recent developments that make it an excellent choice for measuring masses of large molecules in complex mixtures that are not readily amenable to analysis with more conventional methods. In CDMS, an ion is passed through a conductive cylinder resulting in an induced charge pulse in the detection circuit that has an amplitude which is proportional to the charge of the ion. The *m*/*z* of an ion with a known kinetic energy is determined from its measured velocity. CDMS instruments in which the ion passes once through a single detector tube have been used to measure the mass and charge of cosmic dust,[11–13] synthetic polymers,[14] viruses,[15] DNA,[16,17] and nanoparticles.[18,19] However, the uncertainty in the measured charge using a single-pass instrument is high (>75 *e*), leading to correspondingly large uncertainties in mass measurement.[15] To increase the signal-to-noise ratios of these measurements and improve the accuracy of charge measurement, Benner[20] used an electrostatic ion trap to recirculate ions through the conductive detection cylinder, which reduced the charge uncertainty to 2.3 *e* for an ion trapped for 450 passes. Dugourd and co-workers[21–24] used an ion-trapping CDMS instrument based on the design of Benner to obtain the mass and charge of polyethylene glycol (PEG) and DNA precursor ions in single ion photodissociation experiments. Multiple detection electrodes have been incorporated into CDMS traps to improve signal averaging by increasing the number of measurements on each pass between the trapping electrodes and have been used to measure the mass distributions of synthetic polymers and nanoparticles as large as ~300 MDa.[25] In lieu of direct velocity measurements, Contino and Jarrold[26] demonstrated that the frequency of the periodic signal generated by a trapped ion measured using a Fourier transform (FT) can be used to determine the *m*/*z* of the ion and the amplitude measured at that frequency can be used to determine the charge of the ion. Using this technique, Jarrold and co-workers[27–34] have investigated pyruvate kinase multimers with masses ranging from 0.25-1.5 MDa and the assembly mechanisms of several viruses with masses ranging from 2-50 MDa.

The overall uncertainty in mass measurement in CDMS depends on the uncertainty in both the charge and *m*/*z* measurement. Uncertainty in the charge measurement can be reduced significantly by trapping the ion for longer times. By cryogenically cooling their detection electronics, optimizing CDMS instrumentation for longer ion trapping times and using improved FT analysis techniques, Jarrold and co-workers[26,35,36] have significantly improved the limits of detection (~7 *e*) and the precision of charge measurement in ion-trapping CDMS, with uncertainties as low as 0.196 *e* rmsd for ions trapped for 3 s. With this substantial reduction to charge uncertainties measured for ions using CDMS, uncertainty in ion mass is largely determined by the uncertainty in *m*/*z*.[36] The distribution of ion energy per charge (eV/*z*) admitted into the CDMS trap currently limits this *m*/*z* uncertainty.[35,37] A dual hemispherical deflection analyzer[26] (0.6% eV/*z* FWHM) and turning quadrupole[38] (2% eV/*z* FWHM) have both been utilized to decrease the width of the initial ion energy distribution prior to trapping.

More recent work on CDMS instrumentation and analysis has shown that the oscillation frequency and energy per charge of an ion gradually change over the course of the trapping period, which can significantly increase the uncertainty in *m*/*z* measurements.[37–39] This change is a result of collisions with background gas and, for larger ions, solvent evaporation from the intact ion that occurs during the early stages of the trapping period. Both of these effects result in decreased ion energy per charge and increased ion oscillation frequency.[38,39] Ion fragmentation, in contrast, can yield large, sudden changes in the energy per charge of the ion and ion oscillation frequency.[38,39] Keifer et al.[39] observed that hepatitis B virus capsids (~4 MDa) gradually increased in frequency and primarily attributed this effect to solvent mass loss. They also observed sudden jumps in ion frequency corresponding to loss of 1 kDa that they attributed to solvated ion loss. Elliott et al.[38] quantified a relationship between the ion energy per charge and the turning-time ratio (TTR), the ratio of the time required for an ion to turn around in the trapping potential and the time required to pass through the detection cylinder, measured from the separation between pulses in the time domain signal. Using this relationship, ion energy per charge was determined for each 10 ms segment of a PEG ion trapped for 4 s, enabling the accurate determination of the ion mass in each 10 ms segment even after six fragmentation events, solvent evaporation, and background collisions drastically changed the ion energy per charge from its initial value. Because the energy of each fragment ion can be measured, the masses of each fragment ion can be obtained as well.[38] With this method, MS^7 measurements of a single ion initially trapped in a CDMS instrument have been demonstrated.[38] The energy lost to background collisions for the precursor ion and the final fragment ion was also measured and used to gain information about the collision cross sections of these ions.[38] This method to measure ion energies via their TTR requires that the signal be higher than the noise in the time domain signal (~300 *e*).[38] An alternative method was introduced to measure the collision induced decrease in energy per charge of protein ions trapped in a CDMS instrument with masses ranging from 8.6 kDa to 66.5 kDa and charges from +8 to +53.[37] This energy measurement method uses a relationship between frequency change and ion energy per charge that requires that the analyte ion *m*/*z* be known, which, in turn, requires resolved charge states in the mass histogram. The total energy losses measured for these protein ions correlate well with collision cross sections measured using drift ion mobility.[37] This indicates that measurements of the time evolution of energy per charge of single ions can provide information about ion shape similar to that gained using conventional ion mobility techniques despite the significant differences in these methods.

In this work, a method using the higher-order harmonics of the FT of the CDMS ion signal to determine ion energy per charge is demonstrated. This method does not require that the analyte ion have sufficient charge to produce signal above the noise level in the time domain and it does not require the ion to have a known *m*/*z*, making this method more universally applicable than previous methods[37,38] used for ion energy determination. The unconstrained nature of this ion energy measurement largely precludes the need for ion energy selection prior to the trapping and analyzing the masses of individual ions. Because this ion energy measurement is made dynamically *in situ*, the change in energy over time can be monitored to gain ion cross sections, mass changes due to solvent evaporation, and mass changes due to molecular fragmentation.

2.3 Experimental

Experiments were performed using a home-built charge detection mass spectrometer that has been described in detail previously.[38] Briefly, ions are formed by nanoelectrospray ionization using borosilicate capillaries and enter the instrument through a modified Z-Spray source (Waters, Milford, MA, USA). Ions then travel through two RF-only quadrupole ion guides and an energy selective turning quadrupole (Ardara Technologies, Ardara, PA, USA). The turning quadrupole directs the energy selected ions into the electrostatic cone trap that contains the detection cylinder. The pressure in the vacuum chamber housing the electrostatic cone trap is approximately 5×10^{-9} Torr. Polyethylene glycol (PEG) with a nominal molecular weight of 4 MDa was obtained from Sigma-Aldrich (St. Louis, MO, USA) and was prepared at a concentration of 120 nM in 50:50 water–methanol and used without further purification.

Ions induce a charge pulse when passing through the detection cylinder. These pulses are amplified by a CoolFET charge sensitive preamplifier and a linear voltage amplifier (Amptek, Bedford, MA, USA). An additional shaping amplifier (Amptek, Bedford, MA, USA) is also used in a second detection channel and has been described previously.[38] PEG ions studied in this work have sufficient charge (>300 *e*) that the signal of a single ion that passes through the detection cylinder one time is above the noise in the time domain signal recorded in the shaped channel, which is used to control the ion trap. The entrance of an ion into the detection cylinder triggers the raising of the potential of the front electrode of the trap to equal that of the back electrode for a specifiable time (500 ms in these experiments). The time domain signal generated by a trapped, oscillating ion is analyzed offline by a LabVIEW program described previously[25] that finds peaks of consistent size and spacing in the signal from the shaped channel. Data from ions trapped for less than 5 ms were discarded. All FT analysis is performed using the unshaped channel, with another LabVIEW program that performs a 5 ms segmented FT and records the amplitudes of both the fundamental and second harmonic peaks as well as the ion frequency for each segment. With the minimum trapping time set to 5 ms, the average trapping time for the ions measured here was 254 ms, with 21% of ions trapped for the 500 ms maximum trapping time.

2.4 Results and Discussion

2.4.1 Individual Ion Energies from Ratio of Harmonic Amplitudes

In CDMS, analyte ions pass through a detection tube and the charge pulse induced by the ion is measured. In trapped ion FT-CDMS, ions are recirculated through the detection tube inside an electrostatic trap, producing a regular series of pulses well suited to analysis by FT. The relative amplitudes of the fundamental frequency and harmonic frequencies in a FT of a pulse train depends on the pulse shape and duty cycle of the periodic signal. CDMS signals resemble an ideal pulse train, where the time spent by an ion inside the tube is the "on" portion of the cycle and time spent outside the tube is "off". For signals with the shape of an ideal pulse train, the relationship between the FT amplitude of the *n*th harmonic frequency, a_n, the time domain amplitude (A), and the duty cycle (d) is given by Equation 2.1.[40]

$$a_n = \frac{2A}{n\pi} sin(n\pi d) \tag{2.1}$$

The time domain signals for two ideal pulse trains of the same frequency with duty cycles of 0.3 and 0.4 are shown in Figure 2.1 along with the corresponding harmonic frequency amplitudes obtained from the FT of the time domain signals. The two pulse trains have markedly different

distributions of amplitude among the harmonic frequencies that result from the different duty cycles. Because specific distributions of harmonic intensities correspond to specific duty cycles, they can be used as a "fingerprint" that characterizes the duty cycle in the time domain signal.

The ratio of the amplitudes of any two harmonic frequencies can be calculated from Equation 2.1. This ratio does not depend on the time domain amplitude, A. The equation for the ratio of the first and second harmonics is a special case that can be simplified significantly and is given by Equation 2.2.

$$\frac{a_1}{a_2} = \sec(\pi d) \tag{2.2}$$

This equation for the ratio of the first two harmonic amplitudes is one illustration of the fundamental relationship between the ratio of any two harmonic amplitudes in the FT of a pulse train and its duty cycle. Hereafter, the ratio of a_1 and a_2 given by Equation 2.2 will be used exclusively and will be referred to as the harmonic amplitude ratio (HAR). Any other ratio of harmonic frequency amplitudes can also be mathematically related to the duty cycle. However, the first and second are the two largest harmonics for duty cycles observed in the CDMS instrument used here, so defining the HAR with these peaks maximizes the signal-to-noise ratio (S/N) for determining these values from experimental data.

The pulse train produced by an ion trapped in a CDMS instrument has been characterized using the TTR, which is the ratio of the time an ion spends outside the detection cylinder to the time spent inside the detection cylinder.[38] The duty cycle is related to the TTR, and appropriate substitution in Equation 2.2 yields a relationship between HAR and TTR for an ideal pulse train that is given by Equation 2.3.

$$HAR = \sec\left(\frac{\pi}{TTR+}\right) \tag{2.3}$$

The relationship between the TTR and the energy per charge for a single ion, including the effects of ions injected off-axis and at angles resulting in off-center axis trajectories, has been characterized previously using SIMION ion trajectory simulations for the trap geometry employed here and a trap potential of 330 V.[38] In this study, SIMION simulations were performed over a range of trap potentials from 100-500 V on ions traveling along the longitudinal trap axis to characterize the ion energy per charge/TTR relationship over a broader set of instrumental conditions. The relationship between ion energy per charge and TTR depends on the trap potential, but the ratio of the trap potential to the ion energy per charge yields a constant TTR value. Thus, the ion energy per charge can be determined for any ion from the applied trap potential and the measured TTR. This result makes ion energy selection prior to the trap unnecessary for accurate single ion mass measurements because the energy per charge of each ion can be measured dynamically *in situ*. Further information about the SIMION simulations is provided in the Supporting Information.

For the ion trap geometry used here, the stable range of ion TTRs is ~1.7 – 2.4, over which Equation 2.3 is continuous. For different trap geometries with a stable TTR range where Equation 2.3 is not continuous, a different set of harmonic frequency amplitudes could be used. Thus, for a known trap geometry, the HAR measured in the FT can be directly related to the energy per charge of an unknown ion. A previous method used to determine ion energy per charge required that the signal induced by an ion is above the noise in the time domain.[38] This requirement for an

observable signal directly in the time domain spectrum restricts this prior method to large ions that have sufficient charge (~300 charges).[38] An advantage of this new method, in which the ion energy is obtained from the HAR, is that it does not require that the time domain signal induced by a single ion produce observable signal above the noise but rather only that the first and second harmonic be observable in the FT of the signal. This makes it possible to apply this method to smaller ions with many fewer charges. Another method demonstrated previously makes it possible to determine ion energies for low charge ions, but this method requires known ion *m*/*z* values obtained from resolved charge states of proteins with known mass.[37] The HAR measurement can be used to determine the energy per charge of ions without any prior knowledge of the ion *m*/*z* and charge state, making this method more generally applicable to ions of any size or charge.

2.4.2 Ion Signal Simulation

The dimensions of the ion trap, the ion velocity, and the RC time constant associated with the electronic components of the detector can affect the shape and amplitude of the pulse train generated by a trapped ion. In this work, a SIMION simulation similar to that performed by Alexander et al.[41] was used to simulate the shape of the pulse induced by an ion passing through a cylindrical detection tube with the same dimensions and surroundings used in the experiments. This pulse shape was then appropriately scaled by the simulated ion velocity derived from a specified frequency and TTR. A simulated pulse train 25 ms in length was generated by concatenating copies of the pulse shape at the simulated ion frequency then sampled at 5 MHz, which was chosen to match the sampling rate typically used in these CDMS experiments. Finally, a simulated RC constant of 20 μs was applied across the entire transient using an iterative method described by Weinheimer.[42] A RC constant of 20 μs was determined from the decay of the output signal after charge pulses were applied to the detection circuit of the CDMS instrument used here. The FT of these simulated pulse trains was then used to calculate the HAR.

A single pulse of this simulated signal is compared to an ideal pulse of the same duration in Figure 2.2 (inset). The significantly different pulse shape compared to an ideal waveform results in small perturbations to the harmonic amplitudes in the FT described by Equation 2.1. As a result, the relationship between HAR and TTR is also affected. To quantify this effect, simulated ion signals were generated at intervals of 0.05 TTR over the range of TTRs that are stable in the CDMS ion trap used here (1.70-2.40 TTR) and at a frequency of 40 kHz. The HARs measured for the simulated signals were compared to the calculated HARs of ideal pulse trains over the same range of TTR. The HAR values for the simulated ion signal are slightly greater than those of the ideal pulse train (Figure 2.2). Because the perturbed mathematical relationship between TTR and HAR for the simulated ion signal is not straightforward to derive, a 3rd order polynomial fit was instead used to model the data and is given in Equation 2.4.

$$HAR = -1.1653 \times TTR^3 + 8.3686 \times TTR^2 - 20.724 \times TTR + 19.309 \qquad (2.4)$$

Although the functional form of this fit may not be appropriate for extrapolation outside the range of TTR simulated (1.7-2.4), the R^2 value (0.99996) indicates an excellent fit within this range.

2.4.3 Comparison of Model to Signals of PEG Ions

To validate this model for the signals of trapped ions, the TTR predicted using the HAR of real ion signal must be compared to an independent measurement of TTR. The TTR can be readily obtained from analysis of the data as long as ions have enough charge to produce a signal above

the noise in the time domain signal.[38] Obtaining the TTR this way provides a reasonably accurate measurement of energy per charge, with an uncertainty of ~1% that mainly originates from ions that have trajectories that are slightly off-center.[38]

In this work, the TTR was measured using this time-domain method for 3,538 segments of PEG ion signal 5 ms in length taken from 82 individual PEG ions. The HAR measured in the FT of each 5 ms segment was also recorded. Although ions that have a broad range of frequencies were detected, only segments with an average frequency between 39.5-40.5 kHz were included in this analysis in order to match the simulated ion signal frequency of 40 kHz. The shape of the waveform does depend slightly on frequency. However, the relationship between HAR and TTR at a single frequency is sufficient to illustrate this method. A 5 ms FT segment length was chosen to minimize broadening of the FT peaks owing to the slow frequency shift that occurs because of ion collisions with background gas. This broadening attenuates higher order harmonics disproportionately more than the fundamental frequency, leading to inflated HAR values. This effect constrains the length of the time segment that can be transformed and used to obtain accurate ion TTR values. However, the same effect means that HAR values are also sensitive to sudden changes in ion oscillation frequency that have been observed previously.[37,38] These sudden changes in ion frequency, caused by ion trajectory instability or fragmentation, can broaden or even split the FT peak for a single ion within a 5 ms segment, resulting in artificially lowered amplitudes and anomalously high values of the HAR. To filter out these errant data points, the HARs measured for each 5 ms segment of a single ion signal are fit using a bisquare linear regression that iteratively reduces the weight of outliers in a least squares regression. Segments with a HAR value more than three standard deviations away from the fit value are discarded. This process is reiterated with the remaining HAR values until there are no outliers; for the ions studied here, ~6% of segments were discarded by this procedure.

PEG ions with a wide range of TTR values (~1.8-2.4) near the selected 40 kHz oscillation frequency were generated by broadening the energy range of the PEG ions admitted to the trap by the turning quadrupole to be similar in width to the energy distribution produced in the ion source. Different ion source conditions were used to produce different distributions of ion energy that cover the range investigated here. Ion segments were binned in increments of 0.01 TTR and the mean HAR values are plotted in Figure 2.3 for bins containing more than 20 ion segments. The bin size of 0.01 TTR closely approximates the average uncertainty in the time domain measurement of the TTR of ions at 40 kHz. The error bars shown represent one standard deviation in the distribution of HAR of ions within each bin. The simulated signal fit given by Equation 2.4 is also shown and matches well with the trend observed for real ion signal. The gap in the experimental data from 1.95-2.00 TTR is not due to an uneven sampling of PEG ion energies; ions in this range are unstable and are quickly lost from the trap. A possible explanation for this observation is an imperfection in the experimental potential surface that results in unstable trajectories at the ion energies represented by this range of TTR. The mean deviation from the fit is +0.6% and the standard deviation for all the individual 5 ms segments is 1.7%. The mean deviation is much lower than the statistical spread of the data due to noise in the experimental data. The positive mean deviation observed may be due to the small amount of frequency shift caused by collisions with background gas that occur during the 5 ms data segments. This frequency shift disproportionally broadens the different harmonic peaks in the FT, leading to a slightly increased HAR value. Overall, this analysis indicates that using the simulated signal fit for HAR is a good

model for the experimental signal. Importantly, it demonstrates that the TTR and, by extension, the energy per charge of an ion can be measured directly and accurately using the HAR alone.

This new method of using the HAR to obtain TTR values results in slightly higher standard deviation in the TTR measured for each 5 ms segment of a trapped ion (1.7%) compared to inherent uncertainty in the TTR-energy calibration owing to different possible ion trajectories (~1%), but this limitation can largely be overcome by taking advantage of long total trapping times for ions. Figure 2.4 shows a plot of the energy per charge measured using the HAR at each of the 5 ms segments for two PEG ions trapped for 500 ms. The charges measured for ion #1, shown in red, and ion #2, shown in black, are 893 ± 1 and 1262 ± 1 charges, respectively, and do not change significantly during the trapping period. The energy per charge for both ions decreases with time. This decrease in the energy per charge of the ions is consistent with previous results for single small protein ions[37] and PEG ions[38] where energy loss was measured using known ion m/z or time domain analysis, respectively. These decreases in ion energy per charge can be fit using a linear regression (shown in Figure 2.4) with slopes of -0.021 and -0.013 eV/z·ms, intercepts of 220.4 and 216.9 eV/z, and standard errors of 1.9 and 1.4 eV/z for ion #1 and #2, respectively. Using these intercept energies and the initial ion frequencies (39.406 and 39.423 kHz, respectively), the initial m/z's were determined to be 3544 ± 31 and 3602 ± 24 Da/z, for ions #1 and #2, respectively. From the independent m/z and charge measurements, the initial masses of these two ions were determined to be 3.15 ± 0.03 and 4.54 ± 0.03 MDa, respectively. The final masses measured for these ions, obtained from the ion energy per charge determined from each fit at 500 ms, were 2.99 ± 0.02 and 4.39 ± 0.02 MDa. Thus, these ions lost 0.16 ± 0.04 and 0.15 ± 0.03 MDa during the time that they were trapped, consistent with solvent evaporation from these ions.[38]

The standard deviation of the fit in energy per charge is 0.88% and 0.63%, respectively, of the initial energy of each ion. This is significantly lower than the 1.7% uncertainty associated with each individual 5 ms segment. Because neither the time domain or HAR method for obtaining ion energies account for the ~1% uncertainty associated with off-center trajectories, any error in the fit that is below 1%, as is the case for these PEG ion energies measured using HAR, is no longer the dominant limitation in obtaining accurate ion energies. For lower charge analytes that induce smaller signals and have correspondingly higher relative uncertainties in the amplitudes measured for each harmonic, the standard uncertainty in these measurements can be decreased by using longer ion trapping times, although a more sophisticated fitting function may be necessary to accurately reflect the change in the TTR over time. Jarrold et al.[39] used an exponential function to model ion energy loss in CDMS over a 3 s time period. However, the relatively small percentage of energy loss and much shorter 500 ms ion trapping time used justify the simpler linear regression fits used here.

2.4.3 Ion Cross Sections from Energy Loss Measurements

Measuring the energy per charge of each ion directly as a function of time has several advantages in CDMS measurements. Accurate ion energy measurements in CDMS can be used to increase the accuracy of mass measurements when ions with a relatively broad range of energies are introduced into the trap making it possible to increase the ion throughput for dilute samples where few ions are formed. Mass losses due to fragmentation events and solvent evaporation can change ion energies during a trapping period; measurements of ion energy make it possible to quantify these mass changes. Ion energy measurements also have the potential to provide

information about the cross sections of individual ions that are weighed in the trap. For previous work on small protein ions ranging from 8-65 kDa, the total ion energy loss over a 500 ms period was shown to be linearly correlated with the collision cross sections measured using more conventional ion mobility measurements on ensembles of ions, suggesting that ion energy loss can be used to obtain a measure of the collision cross section of ions in CDMS.[37]

The total energy loss was determined for the PEG ions studied here by taking the difference of the energy per charge fit at 0 and 500 ms and multiplying by the total charge; ion #1 lost 8.7 keV and ion #2 lost 7.8 keV over the course of the trapping period. These total energy losses are the sum of two energy loss mechanisms: collisions with background gas that reduce ion kinetic energy and solvent evaporation that changes the ion mass. Previous work using a SIMION simulation of an ion that lost a constant mass per unit time but experienced no collisions with background gas demonstrated that these two mechanisms for energy loss can be deconvolved.[38] Using additional SIMION simulations, this method has been generalized by determining the relationship between the percentage of mass lost and the percentage energy lost by ions with a range of TTRs that span the stable range of the current trap geometry (1.7-2.4). Ions with a higher TTR lose more energy for the same relative mass loss than ions at lower TTR. Additional detail on these SIMION simulations is provided in the Supporting Information.

For the PEG ions studied here, mass losses account for 6.4 and 5.7 keV of the total energy lost for each ion, respectively. The remaining 2.3 and 2.1 keV of energy lost from each ion is due to collisions with background gas. Extrapolation of the linear correlation between ion energy and collision cross section observed previously[37] yields cross section values of 1150 and 1060 nm^2 for ions 1 and 2, respectively. Uetrecht et al.[43] previously determined collision cross sections of 680-710 nm^2 and 870-910 nm^2 for hepatitis B virus (HBV) capsid conformers weighing 3.01 and 4.02 MDa ($T = 3$ and $T = 4$ capsids, respectively). These cross section values are lower than those of the PEGs of similar mass measured here, but the differing charge and structure of the HBV ion is consistent with this difference. The HBV ions measured had average charges of 140 and 160 for the $T = 3$ and $T = 4$, capsids, respectively and exhibit compact icosahedral structures.[43] In contrast, the PEG ions measured here have 893 and 1262 charges and, as a single chain polymer, a much less compact structure is expected. Both effects could contribute to a more disorganized, less compact structure that yields the higher cross section values observed. It is also important to note that the absolute accuracy of the cross section values determined for PEG is almost certainly limited by extrapolating a trend observed previously for much smaller ions. However, the relative cross sections determined by collisional energy loss are limited only by the precision of the energy and charge values measured. Because of the larger cross section and smaller mass observed for ion #1, we conclude that ion #1 is much less dense than ion #2, indicating that the shapes of the two ions are significantly different. Additional experiments are underway to improve the cross section calibration by measuring CDMS energy losses for large molecules and macromolecular complexes for which accurate cross section values have been determined using more conventional ion mobility techniques. However, these results demonstrate that the new CDMS methods developed here make it possible to simultaneously measure the mass, charge, and cross section of individual ions of virtually any size.

2.5 Conclusions

A fundamental relationship between the TTR of the pulse train produced by an ion trapped in a CDMS instrument and the corresponding FT harmonic amplitudes makes it possible to

measure the ion energy using only the FT of the ion signal. Simulated ion signals accounting for non-ideal pulse train characteristics are used to calibrate the relationship between the HAR and TTR. The validity of this calibration is confirmed by comparison to PEG ions for which the TTR is measured using a method independent from the measured HAR. The mean deviation between the TTR determined for each 5 ms segment of PEG signal using the HAR and the independent TTR measurement is 0.6%, much less than the ~1% uncertainty[38] in converting TTR measurements to ion energies that stems from the range of possible ion trajectories within the trap.

The energy per charge of two PEG ions trapped for 500 ms is monitored using the HAR over their respective trapping times. A fit of these values over time decreases the uncertainty associated with both the initial energy and mass measurement. Both ions show significant decreases in energy per charge over time due to solvent evaporation and collisions with background gas. Notably, the PEG ion with lower initial mass (3.15 MDa) loses more total energy than the higher initial mass ion (4.54 MDa). Combined with the greater mass loss for the smaller ion, this disproportional loss of energy suggests that the low mass PEG ion exhibits a less dense gas phase conformation than the high mass ion. This observation also demonstrates that energies determined using HARs can be used to gain information about single ion cross sections. Because this FT harmonic analysis does not require a known ion *m*/*z* or ion signal observable above the time-domain noise, it can be applied to determine the mass and cross sections of ions that were previously inaccessible using CDMS techniques or conventional ion mobility/mass spectrometry. Current work is underway to extend the relationship between energy loss and collisional cross section to higher masses, using large molecules for which accurate collisional cross sections have been measured with more conventional ion mobility instruments.

2.6 Acknowledgements

This material is based upon work supported by the National Science Foundation under CHE-1609866. The authors thank Professor Martin F. Jarrold for helpful discussions and Professor Ryan R. Julian for his innovative contributions to science.

2.7 References

(1) Snijder, J.; Rose, R. J.; Veesler, D.; Johnson, J. E.; Heck, A. J. R. Studying 18 MDa Virus Assemblies with Native Mass Spectrometry. *Angew. Chemie - Int. Ed.* **2013**, *52* (14), 4020–4023.

(2) Lössl, P.; Snijder, J.; Heck, A. J. R. Boundaries of Mass Resolution in Native Mass Spectrometry. *J. Am. Soc. Mass Spectrom.* **2014**, *25* (6), 906–917.

(3) Smith, R. D.; Cheng, X.; Brace, J. E.; Hofstadler, S. A.; Anderson, G. A. Trapping, Detection and Reaction of Very Large Single Molecular Ions by Mass Spectrometry. *Nature* **1994**, *369* (6476), 137–139.

(4) Bruce, J. E.; Cheng, X.; Bakhtiar, R.; Wu, Q.; Hofstadler, S. A.; Anderson, G. A.; Smith, R. D. Trapping, Detection, and Mass Measurement of Individual Ions in a Fourier Transform Ion Cyclotron Resonance Mass Spectrometer. *J. Am. Chem. Soc.* **1994**, *116* (17), 7839–7847.

(5) Wuerker, R. F.; Shelton, H.; Langmuir, R. V. Electrodynamic Containment of Charged

Particles. *J. Appl. Phys.* **1959**, *30* (3), 342–349.

(6) Philip, M. A.; Gelbard, F.; Arnold, S. An Absolute Method for Aerosol Particle Mass and Charge Measurement. *J. Colloid Interface Sci.* **1983**, *91* (2), 507–515.

(7) Hars, G.; Tass, Z. Application of Quadrupole Ion Trap for the Accurate Mass Determination of Submicron Size Charged Particles. *J. Appl. Phys.* **1995**, *77* (9), 4245–4250.

(8) Schlemmer, S.; Illemann, J.; Wellert, S.; Gerlich, D. Nondestructive High-Resolution and Absolute Mass Determination of Single Charged Particles in a Three-Dimensional Quadrupole Trap. *J. Appl. Phys.* **2001**, *90* (10), 5410–5418.

(9) Nie, Z. X.; Tzeng, Y. K.; Chang, H. C.; Chiu, C. C.; Chang, C. Y.; Chang, C. M.; Tao, M. H. Microscopy-Based Mass Measurement of a Single Whole Virus in a Cylindrical Ion Trap. *Angew. Chemie - Int. Ed.* **2006**, *45* (48), 8131–8134.

(10) Cai, Y.; Peng, W. P.; Kuo, S. J.; Lee, Y. T.; Chang, H. C. Single-Particle Mass Spectrometry of Polystyrene Microspheres and Diamond Nanocrystals. *Anal. Chem.* **2002**, *74* (1), 232–238.

(11) Shelton, H.; Hendricks, C. D.; Wuerker, R. F. Electrostatic Acceleration of Microparticles to Hypervelocities. *J. Appl. Phys.* **1960**, *31* (7), 1243–1246.

(12) Hendricks, C. D. Charged Droplet Experiments. *J. Colloid Sci.* **1962**, *17* (3), 249–259.

(13) Stradling, G. L.; Idzorek, G. C.; Shafer, B. P.; Curling, H. L.; Collopy, M. T.; Blossom, A. A. H.; Fuerstenau, S. Ultra-High Velocity Impacts: Cratering Studies of Microscopic Impacts from 3 Km/s to 30 Km/S. *Int. J. Impact Eng.* **1993**, *14* (1–4), 719–727.

(14) Viodé, A.; Dagany, X.; Kerleroux, M.; Dugourd, P.; Doussineau, T.; Charles, L.; Antoine, R. Coupling of Size-Exclusion Chromatography with Electrospray Ionization Charge-Detection Mass Spectrometry for the Characterization of Synthetic Polymers of Ultra-High Molar Mass. *Rapid Commun. Mass Spectrom.* **2016**, *30* (1), 132–136.

(15) Fuerstenau, S. D.; Benner, W. H.; Thomas, J. J.; Brugidou, C.; Bothner, B.; Siuzdak, G. Mass Spectrometry of an Intact Virus. *Angew. Chemie - Int. Ed.* **2001**, *40* (3), 541–544.

(16) Fuerstenau, S. D.; Benner, W. H. Molecular Weight Determination of Megadalton DNA Electrospray Ions Using Charge Detection Time-of-flight Mass Spectrometry. *Rapid Commun. Mass Spectrom.* **1995**, *9* (15), 1528–1538.

(17) Schultz, J. C.; Hack, C. A.; Benner, W. H. Mass Determination of Megadalton-DNA Electrospray Ions Using Charge Detection Mass Spectrometry. *J. Am. Soc. Mass Spectrom.* **1998**, *9* (4), 305–313.

(18) Doussineau, T.; Désert, A.; Lambert, O.; Taveau, J. C.; Lansalot, M.; Dugourd, P.; Bourgeat-Lami, E.; Ravaine, S.; Duguet, E.; Antoine, R. Charge Detection Mass Spectrometry for the Characterization of Mass and Surface Area of Composite Nanoparticles. *J. Phys. Chem. C* **2015**, *119* (20), 10844–10849.

(19) Doussineau, T.; Bao, C. Y.; Antoine, R.; Dugourd, P.; Zhang, W.; D'Agosto, F.; Charleux, B. Direct Molar Mass Determination of Self-Assembled Amphiphilic Block Copolymer

Nanoobjects Using Electrospray-Charge Detection Mass Spectrometry. *ACS Macro Lett.* **2012**, *1* (3), 414–417.

(20) Benner, W. H. A Gated Electrostatic Ion Trap to Repetitiously Measure the Charge and m/z of Large Electrospray Ions. *Anal. Chem.* **1997**, *69* (20), 4162–4168.

(21) Doussineau, T.; Yu Bao, C.; Clavier, C.; Dagany, X.; Kerleroux, M.; Antoine, R.; Dugourd, P. Infrared Multiphoton Dissociation Tandem Charge Detection-Mass Spectrometry of Single Megadalton Electrosprayed Ions. *Rev. Sci. Instrum.* **2011**, *82* (8), 084104.

(22) Doussineau, T.; Antoine, R.; Santacreu, M.; Dugourd, P. Pushing the Limit of Infrared Multiphoton Dissociation to Megadalton-Size DNA Ions. *J. Phys. Chem. Lett.* **2012**, *3* (16), 2141–2145.

(23) Antoine, R.; Doussineau, T.; Dugourd, P.; Calvo, F. Multiphoton Dissociation of Macromolecular Ions at the Single-Molecule Level. *Phys. Rev. A - At. Mol. Opt. Phys.* **2013**, *87* (1), 013435.

(24) Doussineau, T.; Paletto, P.; Dugourd, P.; Antoine, R. Multiphoton Dissociation of Electrosprayed Megadalton-Sized DNA Ions in a Charge-Detection Mass Spectrometer. *J. Am. Soc. Mass Spectrom.* **2014**, *26* (1), 7–13.

(25) Elliott, A. G.; Merenbloom, S. I.; Chakrabarty, S.; Williams, E. R. Single Particle Analyzer of Mass: A Charge Detection Mass Spectrometer with a Multi-Detector Electrostatic Ion Trap. *Int. J. Mass Spectrom.* **2017**, *414*, 45–55.

(26) Contino, N. C.; Jarrold, M. F. Charge Detection Mass Spectrometry for Single Ions with a Limit of Detection of 30 Charges. *Int. J. Mass Spectrom.* **2013**, *345–347*, 153–159.

(27) Pierson, E. E.; Keifer, D. Z.; Contino, N. C.; Jarrold, M. F. Probing Higher Order Multimers of Pyruvate Kinase with Charge Detection Mass Spectrometry. *Int. J. Mass Spectrom.* **2013**, *337*, 50–56.

(28) Pierson, E. E.; Keifer, D. Z.; Selzer, L.; Lee, L. S.; Contino, N. C.; Wang, J. C. Y.; Zlotnick, A.; Jarrold, M. F. Detection of Late Intermediates in Virus Capsid Assembly by Charge Detection Mass Spectrometry. *J. Am. Chem. Soc.* **2014**, *136* (9), 3536–3541.

(29) Keifer, D. Z.; Pierson, E. E.; Hogan, J. A.; Bedwell, G. J.; Prevelige, P. E.; Jarrold, M. F. Charge Detection Mass Spectrometry of Bacteriophage P22 Procapsid Distributions above 20 MDa. *Rapid Commun. Mass Spectrom.* **2014**, *28* (5), 483–488.

(30) Kukreja, A. A.; Wang, J. C.-Y.; Pierson, E.; Keifer, D. Z.; Selzer, L.; Tan, Z.; Dragnea, B.; Jarrold, M. F.; Zlotnick, A. Structurally Similar Woodchuck and Human Hepadnavirus Core Proteins Have Distinctly Different Temperature Dependences of Assembly. *J. Virol.* **2014**, *88* (24), 14105–14115.

(31) Pierson, E. E.; Keifer, D. Z.; Kukreja, A. A.; Wang, J. C. Y.; Zlotnick, A.; Jarrold, M. F. Charge Detection Mass Spectrometry Identifies Preferred Non-Icosahedral Polymorphs in the Self-Assembly of Woodchuck Hepatitis Virus Capsids. *J. Mol. Biol.* **2016**, *428* (2), 292–300.

(32) Pierson, E. E.; Keifer, D. Z.; Asokan, A.; Jarrold, M. F. Resolving Adeno-Associated Viral

Particle Diversity with Charge Detection Mass Spectrometry. *Anal. Chem.* **2016**, *88* (13), 6718–6725.

(33) Keifer, D. Z.; Motwani, T.; Teschke, C. M.; Jarrold, M. F. Acquiring Structural Information on Virus Particles with Charge Detection Mass Spectrometry. *J. Am. Soc. Mass Spectrom.* **2016**, *27* (6), 1028–1036.

(34) Lutomski, C. A.; Lyktey, N. A.; Zhao, Z.; Pierson, E. E.; Zlotnick, A.; Jarrold, M. F. Hepatitis B Virus Capsid Completion Occurs through Error Correction. *J. Am. Chem. Soc.* **2017**, *139* (46), 16932–16938.

(35) Pierson, E. E.; Contino, N. C.; Keifer, D. Z.; Jarrold, M. F. Charge Detection Mass Spectrometry for Single Ions with an Uncertainty in the Charge Measurement of 0.65 E. *J. Am. Soc. Mass Spectrom.* **2015**, *26* (7), 1213–1220.

(36) Keifer, D. Z.; Shinholt, D. L.; Jarrold, M. F. Charge Detection Mass Spectrometry with Almost Perfect Charge Accuracy. *Anal. Chem.* **2015**, *87* (20), 10330–10337.

(37) Elliott, A. G.; Harper, C. C.; Lin, H. W.; Susa, A. C.; Xia, Z.; Williams, E. R. Simultaneous Measurements of Mass and Collisional Cross-Section of Single Ions with Charge Detection Mass Spectrometry. *Anal. Chem.* **2017**, *89* (14), 7701–7708.

(38) Elliott, A. G.; Harper, C. C.; Lin, H. W.; Williams, E. R. Mass, Mobility and MSN Measurements of Single Ions Using Charge Detection Mass Spectrometry. *Analyst* **2017**, *142* (15), 2760–2769.

(39) Keifer, D. Z.; Alexander, A. W.; Jarrold, M. F. Spontaneous Mass and Charge Losses from Single Multi-Megadalton Ions Studied by Charge Detection Mass Spectrometry. *J. Am. Soc. Mass Spectrom.* **2017**, *28* (3), 498–506.

(40) Smith, S. W. *The Scientist and Engineer's Guide to Digital Signal Processing*, 1st ed.; California Technical Publ, 1997.

(41) Alexander, J. D.; Graham, L.; Calvert, C. R.; Kelly, O.; King, R. B.; Williams, I. D.; Greenwood, J. B. Determination of Absolute Ion Yields from a MALDI Source through Calibration of an Image-Charge Detector. *Meas. Sci. Technol.* **2010**, *21* (4), 045802.

(42) Weinheimer, A. J. The Charge Induced on a Conducting Cylinder by a Point Charge and Its Application to the Measurement of Charge on Precipitation. *J. Atmos. Ocean. Technol.* **1988**, *5* (2), 298–304.

(43) Uetrecht, C.; Versluis, C.; Watts, N. R.; Wingfield, P. T.; Steven, A. C.; Heck, A. J. R. Stability and Shape of Hepatitis B Virus Capsids in Vacuo. *Angew. Chemie - Int. Ed.* **2008**, *47* (33), 6247–6251.

2.8 Figures

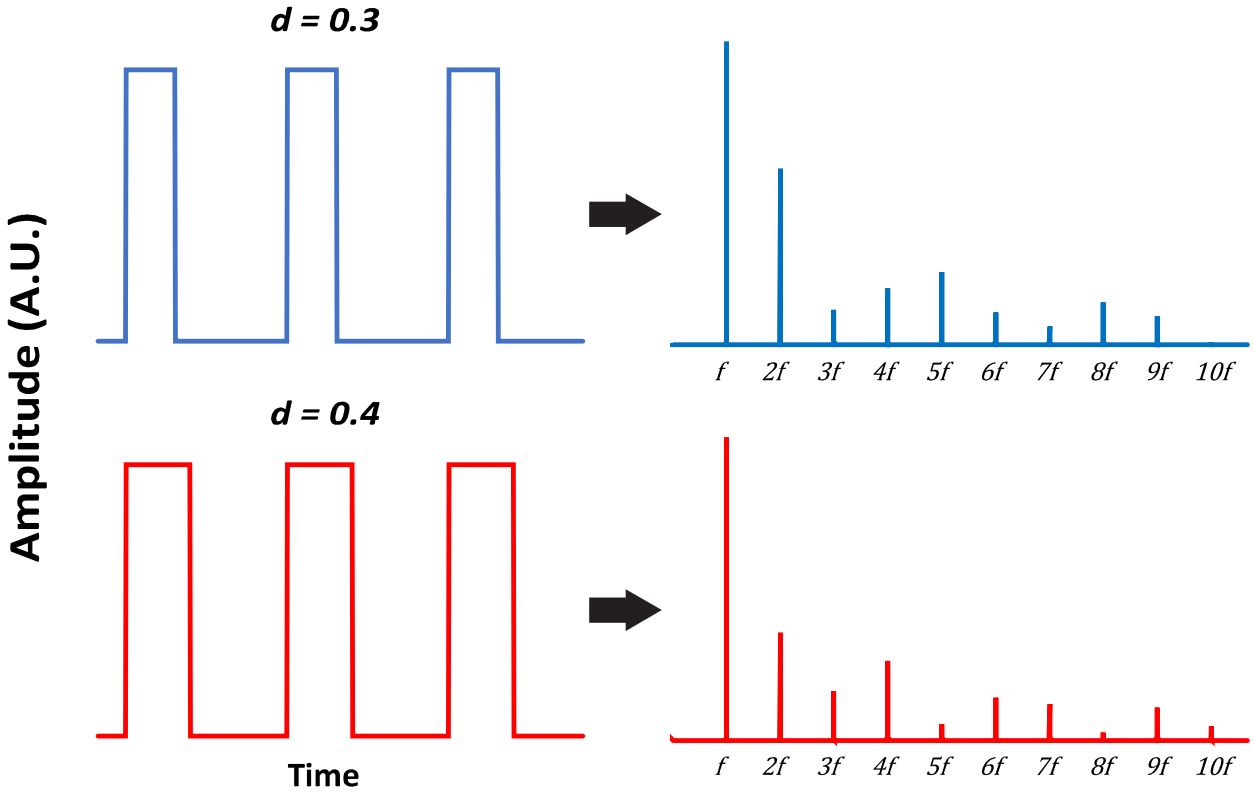


Figure 2.1. Ideal pulse trains (left) with duty cycles of 0.4 (top) and 0.3 (bottoms) and the corresponding FT harmonic amplitudes (right). Small differences in the duty cycle result in significantly different harmonic amplitude distributions.

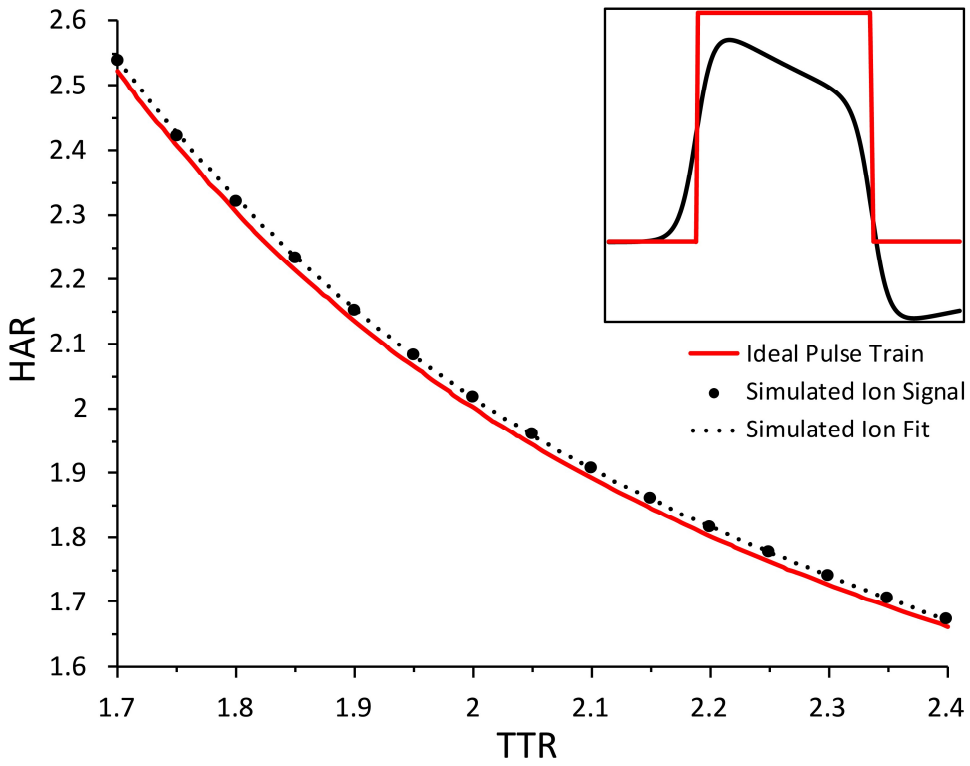


Figure 2.2. Comparison of the dependence of HAR on TTR for an ideal pulse train (red) and simulated ion pulse train (black). The difference in pulse shape (inset) results in consistently higher values of the HAR for the simulated signal. The HAR values of the simulated signal are fit with a third-order polynomial (dotted line).

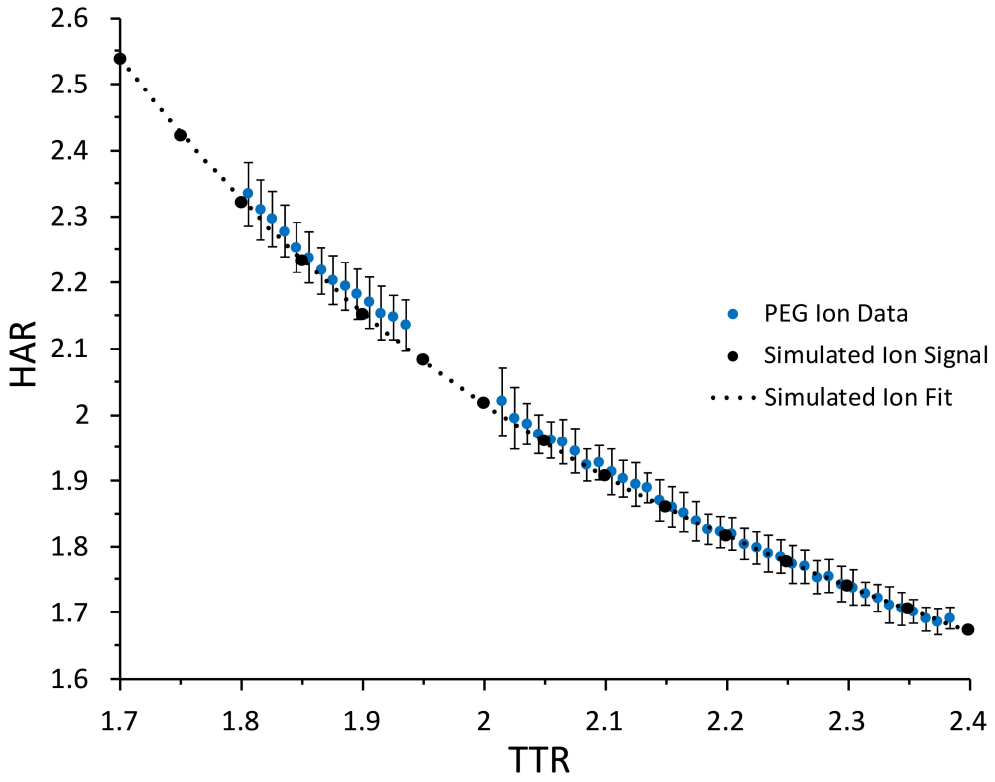


Figure 2.3. Comparison of the simulated signal HAR dependence on TTR to values measured for 5 ms segments of PEG ion signal. For the PEG ions, TTR was measured independently of the HAR. Error bars indicate one standard deviation of the values measured for PEG ions binned in increments of 0.01 TTR. The 0.01 TTR bin size roughly corresponds to the average uncertainty in the time domain TTR measurements for ions at 40 kHz. The gap in PEG ion data from 1.95-2.00 TTR is not due to uneven sampling. Ions in this range are unstable and are lost quickly from the trap, perhaps due to imperfections in the experimental trapping potential.

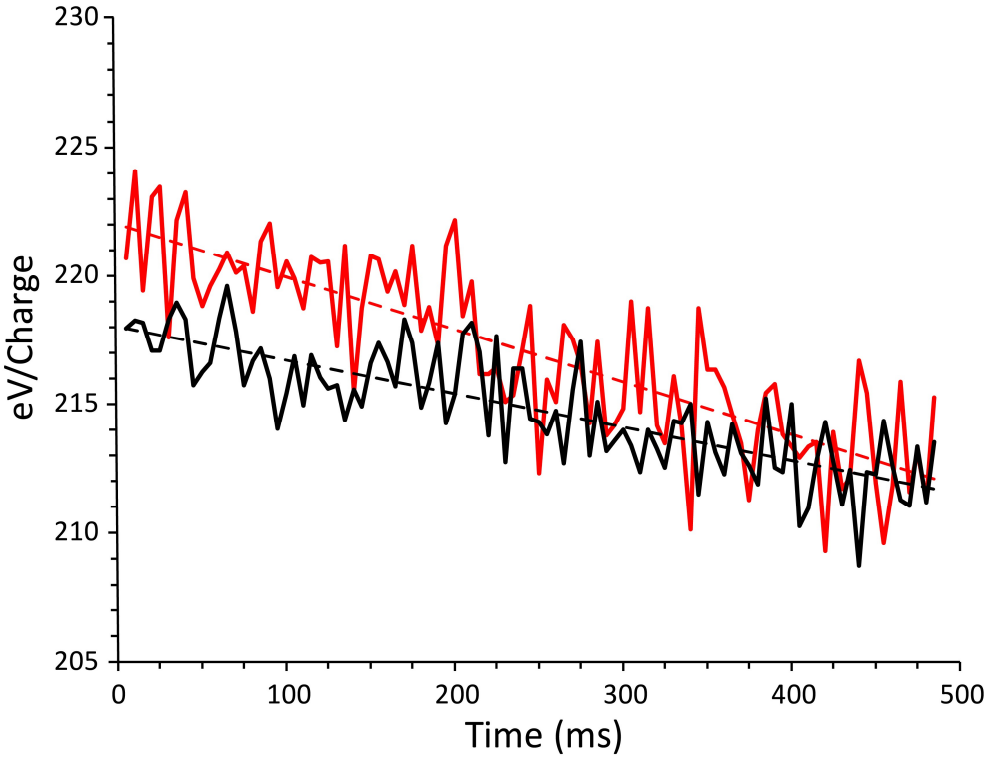


Figure 2.4. Energy per charge measured using HAR for each 5 ms signal segment of PEG ions trapped for 500 ms. Data from ion #1 (red) and ion #2 (black) were fit using a linear regression (dotted lines). Ion 1 has larger energy per charge loss than ion 2 over the same length of time, indicating a greater extent of mass loss and a less dense structure.

2.8 Supporting Information

2.8.1 Determining Ion Energy at Different Trap Potentials

The relationship between the TTR and the ratio of trap potential to ion energy per charge was determined by simulating ion trajectories in SIMION. Ions with energies per charge ranging from 58.7%-77.1% of the trap potential, the range over which ion trajectories are stable for at least 20 cycles, were simulated at trap potentials ranging from 100 to 500 V. At each trap potential, 120 ions were simulated with energies per charge spread uniformly across this range. The TTR was calculated by recording the times at which the simulated ion passed through planes placed at the ends of the detection tube perpendicular to the trap axis. The ratio of the trap potential and ion energy per charge is plotted as a function of TTR in Supporting Figure 2.1. Despite ion energies per charge values that range from 58.7 eV/z at 100 V trapping potential to 293.5 eV/z at the 500 V trapping potential, a constant ratio of trap potential to ion energy per charge yields the same TTR response, as shown in Supporting Figure 2.1. Using these data and experimentally measured TTRs, the energies of ions trapped using a wide range of trapping potentials can be determined.

2.8.2 SIMION Simulations: Determining Energy Lost from Solvent Evaporation

Mass lost by ions during the trapping period due to solvent evaporation or fragmentation changes the energy of the ion. For neutral mass losses, such as solvent evaporation, the potential at which mass loss occurs affects the extent of the energy change. If mass is lost in the field-free region of the trap inside the detection cylinder, where all of the ion energy is kinetic energy, the percentage of mass lost is equal to the percentage of energy lost. In contrast, when the ion is at a non-zero potential during the turning process, only the kinetic energy associated with the neutral mass is lost, resulting in a percentage of mass loss that is greater than the percentage of energy loss. Assuming that mass loss does not depend on the position of the ion in the trap, the average ratio of percent energy loss to percent mass loss relationship is described by Equation S2.1,

$$\frac{\%\ Energy\ Loss}{\%\ Mass\ Loss} = t_{cylinder} + t_{turning} * (1 - V_{turning}) \quad \text{(S2.1)}$$

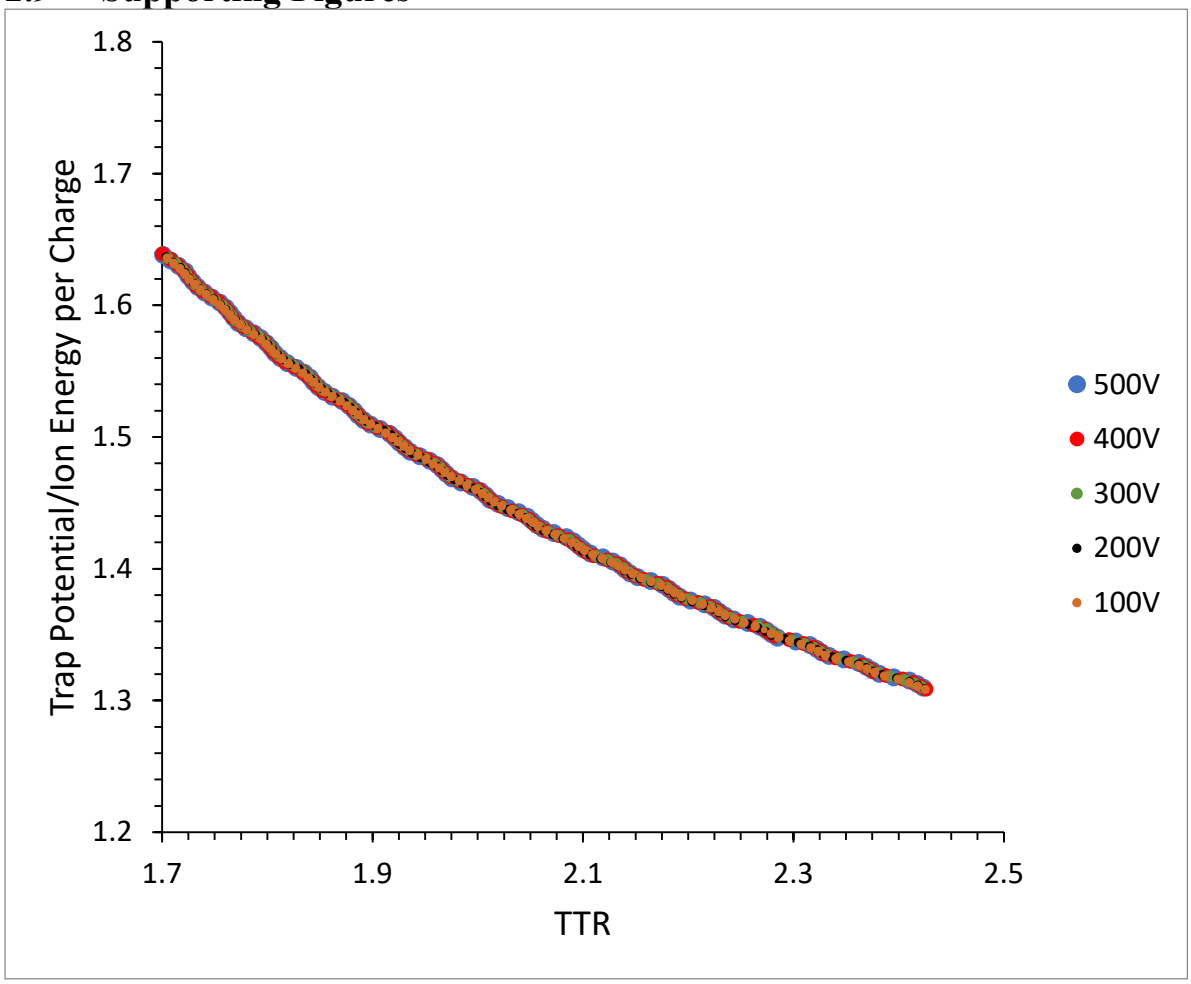
where $t_{cylinder}$ is the proportion of time where the ion is in the detection cylinder, $t_{turning}$ is the proportion of time spent outside of the cylinder, $V_{turning}$ is the average potential experienced by the ion in the region outside the cylinder, normalized by the total ion energy and TTR = $t_{turning}/t_{cylinder}$. SIMION simulations show that $V_{turning}$ also varies as a function of ion TTR for the trap geometry employed here. Thus, the ratio of percent energy loss to percent mass loss can be determined using solely the TTR. A plot of the TTR with respect to the ratio of percent energy loss to percent mass loss is shown in Supporting Figure 2.2 and a quadratic fit of these data is given in Equation S2.2

$$\frac{\%\ Energy\ Loss}{\%\ Mass\ Loss} = 0.0279 \times TTR^2 - 0.2458 \times TTR + 0.9783 \quad \text{(S2.2)}$$

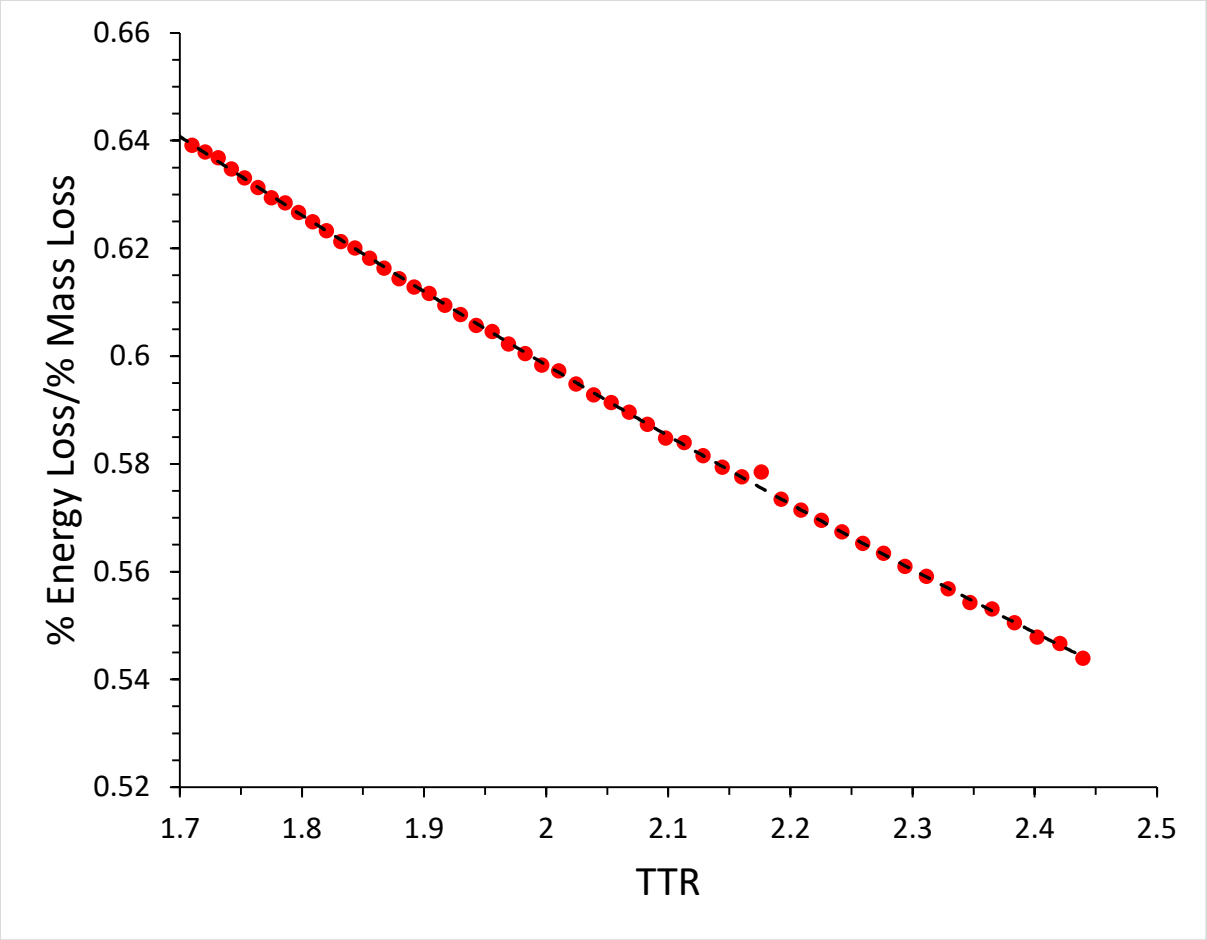
and is shown by the dashed line in Supporting Figure 2.2. The percent energy loss to percent mass loss ratio decreases from 0.64-0.55 as TTR increases over the range of TTRs that have been observed experimentally (1.7-2.4). This relationship makes it possible to accurately determine the proportion of the total energy lost by an ion that is due to neutral mass losses. After accounting for mass-related energy loss, any other energy lost by ions can be attributed to collisions with

background gas which reduce the kinetic energy of the ion and this energy loss can be used to determine ion mobilities.

2.9 Supporting Figures



Supporting Figure 2.1. Data obtained from ions simulated in SIMION at trap potentials ranging from 100-500 V are shown. Different ranges of ion energy per charge are used for each trap potential, but the ratio of the trap potential to ion energy per charge has the same dependence on the TTR regardless of the trap potential used.



Supporting Figure 2.2. Plot of the ratio of percent energy loss to mass loss showing a clear decrease with increasing TTR. As the ion spends more time turning around within the trapping potential, the average potential increases, leaving less kinetic energy available to be lost along with neutral mass.

Chapter 3

Multiplexed Charge Detection Mass Spectrometry for High Throughput Single Ion Analysis of Large Molecules

This chapter is reproduced with permission from:

Conner C Harper, Andrew G. Elliott, Luke M. Oltrogge, David F. Savage, and Evan R. Williams

"Multiplexed Charge Detection Mass Spectrometry for High Throughput Single Ion Analysis of Large Molecules" *Anal. Chem.* **2019**, *91* (11), 7458–7465.

© 2019 American Chemical Society

3.1 Abstract

Applications of charge detection mass spectrometry (CDMS) to measuring the masses of large molecules, macromolecular complexes and synthetic polymers that are too large or heterogeneous for conventional mass spectrometry measurements are made possible by weighing individual ions in order to avoid interferences between ions. Here, a new multiplexing method that makes it possible to measure the masses of many ions simultaneously in CDMS is demonstrated. Ions with a broad range of kinetic energies are trapped. The energy of each ion is obtained from the ratio of the intensity of the fundamental to second harmonic frequency of the periodic trapping motion making it possible to measure both the *m*/*z* and charge of each ion. Because ions with the exact same *m*/*z* but with different energies appear at different frequencies, the probability of ion-ion interference is significantly reduced. We show that the measured mass of a protein complex consisting of 16 protomers, RuBisCO (517 kDa), is not affected by the number of trapped ions with up to 21 ions trapped simultaneously in these experiments. Ion-ion interactions do not affect the ion trapping lifetime up to one second and there is no influence of the number of ions on the measured charge-state distribution of bovine serum albumin (66.5 kDa) indicating that ion-ion interactions do not adversely affect any of these measurements. Over an order of magnitude gain in measurement speed over single ion analysis is demonstrated and significant additional gains are expected with this multi-ion measurement method.

3.2 Introduction

Native mass spectrometry (MS), in which electrospray ionization (ESI) is used to transfer large macromolecules and macromolecular complexes directly from solution into the gas phase, is a powerful tool in structural biology that provides complimentary information to other commonly used structural methods. Information about non-covalent macromolecular interactions, including stoichiometry, stability and assembly kinetics[1-7] can be readily obtained with native MS even from

solutions containing high concentrations (>100 mM) of nonvolatile salts, including traditional biochemical buffers, such as Tris or phosphate.[8, 9] Mass spectral peaks in an electrospray charge-state distribution of large (500+ kDa) macromolecular complexes can be broad owing to adduction of salts and solvent as well as sample heterogeneity.[10, 11] Mixtures are intrinsically heterogeneous but heterogeneity can also affect the analysis of relatively pure samples as a result of chemical modifications of the constituents of a macromolecular complex or multiple stoichiometries of the complex itself. As a result, charge-state distributions of individual components in mixtures of macromolecular complexes or synthetic polymers are often unresolved making it impossible to obtain mass information directly from an ESI mass spectrum.

Information about constituents in a complex mixture can often be obtained using tandem mass spectrometry, in which ions within a limited *m*/*z* range are isolated and dissociated. Fragment ions are formed in a broad *m*/*z* range where the ions can be resolved.[12] This process is enhanced for non-covalent complexes by the phenomenon of asymmetric charge dissociation, which results in the loss of highly charged monomers from a macromolecular complex.[12, 13] An alternative approach to tackling the challenge of sample heterogeneity is to weigh individual molecules or ions. By doing so, the presence of other ions cannot interfere with the mass measurement of another. Single molecule and ion mass measurements have been demonstrated using ion nanoelectromechanical systems[14] and with Fourier-transform ion cyclotron resonance (FT-ICR),[15, 16] ion trap,[17-22] cryodetector time-of-flight,[23, 24] orbitrap,[25, 26] and charge detection mass spectrometry (CDMS).[27-32] These methods can provide accurate masses of individual ions, but often at the expense of analysis time. The number of individual ion measurements necessary to characterize a sample depends on sample complexity. Characterization of mixtures that consist of a vast number of molecules or mixtures where components have very different concentrations requires more single ion measurements compared to the characterization of purer samples.

Weighing ions individually with CDMS has the advantage that fast measurements are possible depending on the accuracy and sensitivity required. In CDMS, an ion passes through a detector, often a conducting tube, and the *m*/*z* is determined by the transit time through the detector tube[33-40] or oscillation frequency inside a trap,[28, 32, 41-56] and the *z* is determined from the magnitude of the induced charge. For highly charged ions, a detectible signal can be obtained from a single pass of the ion through the apparatus leading to a very rapid measurement of ion mass.[33-40] CDMS can include multi-detector arrays,[57, 58] electrostatic ion traps[28, 32, 41-54] or a combination of the two[32] in order to signal average to improve the precision and the sensitivity of these measurements. Electrostatic ion trap based CDMS instruments have been used to measure the masses and assembly kinetics of viruses up to 50 MDa,[46, 49, 50, 55, 56] measure cargo loading into virus capsids,[53] obtain accurate masses of large synthetic polymers[28, 32, 59] and quantify lipoproteins that are important for assessing the risks of cardiovascular disease.[45] Fragmentation[59] and even MS^7 measurements[43] have been demonstrated for a single ion inside a CDMS instrument. Collision cross sections of individually weighed ions can be obtained from changes in the frequency of the ion motion inside the electrostatic ion trap as a result of collisions with background gas.[43, 50-52]

One limitation of trapping CDMS technology is the current need to weigh single ions individually in order to eliminate potential interferences between the signals of multiple ions or ion-ion interactions that can potentially interfere with these measurements. In a recent review on CDMS of large molecules, Jarrold and co-workers state that "…multiple ion trapping events

cannot be analyzed because two highly charged ions trapped together interact and perturb the oscillation frequencies. Hence, only single ion trapping events are useful."[29] In experiments where ions that do not produce detectable signal upon a single pass through a detector tube are measured, ion trapping occurs by systematically lowering the potential of the front of the trap to admit ions and raising the trap potential to trap and weigh the ion.[41] In order to avoid trapping multiple ions and to efficiently acquire data, the ion current must be adjusted so that on average, it is nearly equally probable to have no ions, a single ion or multiple ions in the trap.[29] Thus, under optimum conditions, a single ion is trapped in only 37% of the measurements.[29, 42] However, this necessitates that about two thirds of the measurements contain either no ions or multiple ions and therefore, no ion masses are obtained from the majority of data acquired. The probability of trapping just one ion is significantly reduced if the ion current is either higher or lower than the optimum value making the ion current an essential parameter to optimize for efficient mass measurements. A mass histogram consisting of ~6700 ions can be acquired in about 30 minutes using a 100 ms trapping period and optimum ion current.[42]

Here, we demonstrate a method that enables efficient weighing of individual masses of multiple ions that are trapped in CDMS with precisions and accuracies that are indistinguishable from those made of individually trapped ions. This method takes advantage of the ability to obtain ion energies throughout the measurement process.[51] By trapping ions with a range of energies, the ion signal is spread over a broad range of frequencies even for ions that have the exact same m/z. This significantly reduces the probability of overlapping ion signals. These measurements also show that ion-ion interactions are not a limitation in these experiments within the current ability to weigh individual ions in CDMS. Measurements of up to 13 simultaneously trapped ions are demonstrated, but this method can be extended to significantly more ions. This method enables at least an order of magnitude improvement in the time required to obtain a mass histogram with CDMS, and additional gains in ion measurement efficiency are almost certainly possible from trapping events with even more ions.

3.3 Experimental

3.3.1 Charge Detection Mass Spectrometry

A home-built charge detection mass spectrometer was used in these experiments.[32, 43] Ions are formed by nanoelectrospray ionization of a 5 μM solution of RuBisCO and 10 μM solution of bovine serum albumin (BSA, Sigma Aldrich) both in a 100 mM aqueous ammonium acetate solution using borosilicate capillaries with tips that are pulled to a diameter of ~1.5 μm. Ions enter the instrument through a modified Z-Spray source (Waters Corporation), pass through two RF-only quadrupole ion guides and enter a turning quadrupole (Ardara Technologies) that is used to select a range of ion energies and direct the ions into a chamber that contains an electrostatic cone trap and detector tube. The pressure inside the trap is $\sim 3 \times 10^{-9}$ Torr. The potential of the upstream cone electrode is lowered to 0.0 V for 1 ms to eject ions from the prior measurement and to allow new ions to enter the trap. The potential is subsequently raised to match the downstream cone electrode (330 V) for a specified trapping time of 1.0 s. Ions passing through the detector induce a charge pulse that is amplified by a CoolFET charge-sensitive preamplifier and linear voltage amplifier (Amptek). Because the ions studied here have less than the ~300 e necessary for direct observation in the time domain, a Python program using short-time Fourier transforms (STFT) is

used to analyze the data. A 50 ms segment is analyzed in overlapping steps of 5 ms. The 50 ms segment length was chosen to balance minimizing FT peak widths with amplitude dampening that is caused by ion frequency shifts with time.

For each 5 ms step in the STFT, a peak picking algorithm is used to identify ion frequencies in the range of interest. For peaks within 60 Hz of another peak, only the highest amplitude peak is selected to avoid picking side lobes that occur as a result of no apodization. Peaks that survive for at least 100 ms in the STFT correspond to the initial number of stably trapped ions, i.e., ions must survive at least 100 ms to be considered trapped. Peaks are assigned to individual ion traces based on their frequency proximity across all of the time steps in the STFT. The ion traces of peaks that overlap over the course of the trapping event are discarded. Ion traces that experience large, sudden shifts in frequency exceeding 100 Hz due to an ion being lost from the trap, major change in ion trajectory, or dissociation are truncated to the time step one half of the segment length prior to the large shift. This is done to avoid including dampened amplitude data where the lost ion is still detected, but not present for the duration of the FT segment. The length of time each ion is considered to be trapped is determined from the length of the ion trace.

Because the duty cycle of the ion signal depends on ion energy,[43] the amplitudes of the fundamental and harmonic frequencies also depend uniquely on ion energy.[51] Thus, the ion energy at any time throughout the measurement can be obtained from the ratio of the fundamental amplitude to that of the second harmonic.[51] In combination with the measured frequency, a value of m/z is obtained from equation 3.1;

$$\frac{m}{z} = \frac{C(E)}{f^2} \tag{3.1}$$

where f is the frequency and $C(E)$ is a function of ion energy per charge.[51] This ratio of harmonics is also used to correct the measured fundamental amplitudes for differing harmonic content in order to obtain a more accurate measure of z.[60] These values of m/z and z are multiplied to obtain the individual mass of each ion.

3.3.2 RuBisCO Expression and Purification

Form IA RuBisCO from the chemoautotrophic γ-proteobacterium *Halothiobacillus neapolitanus* was cloned in a pET-14 based expression vector with ampicillin resistance. RuBisCO forms a heterohexadecamer comprised of eight large subunits (CbbL) and eight small subunits (CbbS). The genes *cbbL* and *cbbS* were separated by the native intergenic sequence while a hexahistidine affinity tag was appended to *cbbL*. This plasmid was co-transformed into BL21 (AI) along with an inducible GroEL/ES plasmid (pGro7) in order to facilitate proper protein folding.

The expression cells were grown at 37 °C in 1 L LB with carbenicillin (100 μg/mL) and chloramphenicol (25 μg/mL) up to OD600 = 0.3 - 0.5 whereupon the temperature was reduced to 18 °C and the culture was induced with 0.1% (w/v) L-arabinose. The cells were grown overnight and harvested by centrifugation at 4000 rcf for 15 min. Pellets were stored at -80 °C. The pellets were resuspended with ~25 mL of lysis buffer (50 mM Tris, 150 mM NaCl, pH 7.5) with 1 mM

phenylmethane sulfonyl fluoride (PMSF), 0.1 mg/mL lysozyme, and 0.01 mg/mL DNaseI. The cells were lysed with three passes through an Avestin EmulsiFlex homogenizer and the lysate clarified by centrifugation at 12,000 rcf for 30 min. The supernatant was transferred to a gravity column at 4 °C with ~2 mL of HisPur Ni-NTA resin (Thermo Fisher Scientific). The protein was washed with 10 column volumes of wash buffer (lysis buffer with 20 mM imidazole) and then eluted with lysis buffer containing 200 mM imidazole. The protein was buffer exchanged using 10DG desalting columns (Biorad) to lysis buffer. The purity of the eluted protein was assessed by SDS-PAGE to be >95%. Size exclusion chromatography (Biorad NGC) with a Superose 6 column (GE Healthcare) was used to analytically verify the proper assembly of the L_8S_8 complex. The RuBisCO sample was also analyzed using a Waters quadrupole time of flight (Q-TOF) Premier mass spectrometer. Mass spectra of the whole complex (517 kDa) and the CbbL (51.9 kDa) and CbbS (12.7 kDa) subunit proteins are included in the Supporting Information.

3.4 Results and Discussion

3.4.1 Ion Motion Inside the Trap

RuBisCO is an enzyme that catalyzes the first, and often rate-limiting step, of carbon fixation in the Calvin-Benson-Bassham Cycle. This enzyme consists of a large subunit (CbbL) that weighs ~51.9 kDa and a small subunit (CbbS) with a mass of ~12.7 kDa (Supporting Information). A total of eight CbbL and eight CbbS assemble into a complex that has a mass of ~517 kDa. This molecular complex was chosen to illustrate our multi-ion detection method because the sample can be made relatively pure, and the charge states are relatively low compared to many other analytes effectively analyzed by single ion CDMS. The precision and sensitivity of CDMS measurements improves with larger, more highly charged analytes making a smaller analyte a rigorous test of this method. In addition, the complex is small enough to analyze using conventional time-of-flight MS making it possible to compare this single ion method with measurements from more traditional native MS instrumentation.

Various processes can affect ion motion once an ion is trapped.[52] These processes can provide additional structural information about the sample, but they can also complicate the procedure for mass analysis. Some of these processes are illustrated using data from a single trapping event for ions produced by electrospray ionization of a RuBisCO sample. In this event, 18 ions were initially trapped as indicated by the ion signal at 18 different frequencies at early trap times (Figure 3.1). These data are obtained by short-time Fourier-transform (STFT) of the time domain data of a single trapping event using 50 ms segments stepped at five ms intervals.

The frequencies of the ions that are trapped evolve with time with several characteristics. An example of one of these ions, **A**, is shown in Figure 3.1; this ion has initial and final frequencies of 23,104 Hz and 23,132 Hz, respectively. There are several factors that can affect the ion frequency in these experiments. In general, frequencies tend to gradually increase with time as is the case for ion **A**. This occurs because collisions with background gas reduce the ion energy with time. For ion **A**, this energy loss corresponds to 0.6 eV/charge.[51] This information can be used to obtain the collisional cross section of each ion.[43, 51, 52] There are also frequency variations that occur as a result in a change in ion trajectory inside of the trap. These shifts can be large resulting in an unstable orbit and sudden loss of the ion from the trap, as in the case of ion **B**, which is lost

at ~350 ms. An unstable orbit can also result in larger steps in frequency, as in the case of ion **C** which enters an unstable orbit at ~400 ms but remains trapped for nearly the full 1.0 s of data acquisition. Ions can also be lost due to fragmentation with one or more of the fragments trapped as is the case for ions **D/D'** and **E/E'**. The relationship between each precursor and fragment ion can be readily identified from the temporal correlation of these signals. For example, the initial frequency of ion **D** is 22,750 Hz but this signal disappears at ~300 ms and another signal (**D'**) appears at this same time at a frequency of 22,344 Hz. The *m*/*z* values of the precursor and fragment ions are determined from their oscillation frequency and the real time measure of energy obtained from the ratio of intensity of the fundamental frequency to that of the second harmonic frequency.[51] The charge is determined from the intensity of the fundamental frequency that is calibrated for ion energy using a method described in detail elsewhere.[60] The precursor ion, (**D**), has a measured mass of 522 kDa with 48.5 ± 1.4 positive charges, consistent with the intact complex mass of 517 kDa obtained from averaging data for many ions. The fragment ion (**D'**) has a measured mass of 478 ± 14 kDa with 46 ± 0.5 charges. Formation of this fragment is most consistent with the loss of a CbbL subunit with only 2.5 ± 1.5 charges. The high uncertainty in the charge measurement of the precursor ion is a result of its relatively short lifetime. These results indicate that fragmentation leads to a roughly symmetrical partitioning of charge based on mass or surface area in the dissociation process. In contrast, dissociation of this same intact complex upon collision induced dissociation in TOF MS occurs via a highly asymmetric charge distribution process in which a single subunit carries away between 30+ and 36+ charges (Supporting Information). This difference in charge partitioning to form the same product ion may be due to the low energy metastable dissociation that occurs over hundreds of ms in the CDMS experiments vs. the higher energy deposition necessary to observe dissociation in TOF MS. Previous collisional activation studies of noncovalent dimers showed that symmetric charge distributions can occur at low energy whereas asymmetric charge partitioning occurs with more energetic activation.[13] High energy and short time dissociation can favor unfolding of a monomer subunit prior to complete ejection and resulting flow of charge to the unfolding subunit.[13, 61] Symmetric charge partitioning is also frequently observed with high energy surface-induced dissociation in which energy is deposited rapidly into an ion upon its collision with a surface. This activation method often leads to formation of fragments consisting of multiple subunits which can provide more structural information.[62] Although the dissociation of just one ion is not by itself significant, useful structural information can be obtained from dissociation data obtained for multiple precursor ions that have the same mass. A more detailed study of many dissociation events for individual ions is beyond the scope of this current work, but this single ion example demonstrates another potential application of CDMS in the analysis of large molecules.

Ion signals that are close in frequency can also interfere with each other. This is shown for ions **F** and **G**, which have initial frequencies ~22,024 Hz. Because of small changes in ion orbits as well as a general decrease in frequency with time, the signals of these ions interfere, creating regions of high and low signal in an irregular beat pattern. In this analysis, ions with overlapping frequencies were discarded.

3.4.2 Mass Analysis

To convert the STFT frequency data from each trapping event, e.g, the Figure 3.1 data, into individual ion mass values, a peak picking algorithm is used to identify peaks in each five ms step

of the entire transform. Because the ion trapping frequency can vary with time, the peaks in adjacent five ms time intervals are correlated by proximity in frequency in order to build the individual ion trace i.e. the frequency evolution with time. The ion energy in each five ms step is obtained from the ratio of peak amplitudes of the fundamental frequency to that of the second harmonic frequency.[51] These data provide *m*/*z* values at each five ms interval, which are averaged to obtain a *m*/*z* value that is signal averaged for the duration of the trapping event. Similarly, the peak amplitudes of the fundamental frequency, corrected for the amplitudes of higher harmonic frequencies that vary with energy, are averaged to obtain a value for the ion charge using a calibration procedure that is described in detail elsewhere.[60] The mass of each ion is then obtained from the multiplication of the *m*/*z* and *z* values. In order to examine effects of multiple trapped ions on the mass measurement, only ions that survive for the full 1 s of trapping time are used in the mass histograms. If an ion frequency trace converges with another, both ions are excluded. For example, of the 18 ions initially trapped in the Figure 3.1 data, 11 ions pass these culling criteria and are included in the final mass histogram. In sum, 6988 ions meet all of these criteria, and the maximum number of ions included from a single trapping event is 13.

The probability of traces converging depends on a number of factors, including the number of trapped ions, their *m*/*z*, their energy and the intrinsic frequency width of the peak. The intrinsic frequency width depends both on the STFT segment length and the collision induced frequency change. Because ions with a range of energies are introduced through the energy selective bending quadrupole and are trapped in these experiments, even ions with the exact same *m*/*z* value will have a range of frequencies. In these experiments, an ion with *m*/*z* 10,550 (corresponding to the 49+ ion) has a peak width of 40 Hz (at peak base) but within the range of energies that was filtered and trapped (~215 to 245 eV/charge), an ion at this *m*/*z* can appear at frequencies ranging from 21,500 Hz to 23,250 Hz (a 1750 Hz bandwidth; indicated by the bracket in Figure 3.1). In principle, 1750/40 = ~44 ions with the exact same *m*/*z* value could still be still be readily resolved and individually weighed if their energies were evenly dispersed over this range. In practice, this value will be much lower in order to avoid overlaps, but extending the range of ion energies that are filtered and trapped could reduce the probability of overlap further.

A mass histogram obtained from the data of all of the trapping events independent of the number of ions that were trapped is shown in Figure 3.2a. A Gaussian fit of these data results in a centroid at 517,312 Da with a standard deviation of 13,005 Da (~2.5%). This indicates that the precision of weighing each ion is better than 2.5% because some of this width is due to intrinsic broadening from sample heterogeneity and adduction. Measurement of 6988 ions improves the precision of the overall mass measurement to ~0.03%. The centroid mass of the complex obtained from a deconvolved mass spectrum obtained using a commercial Q-TOF mass spectrometer is 516,900 Da ± 100 Da (Supporting Information). The standard deviation of a Gaussian fitted to the deconvolved data is ~1,700 Da. This provides an estimate of the fraction of the uncertainty in the CDMS measurement that is intrinsic to the sample. The small mass difference between the CDMS and Q-TOF MS centroid values is likely due to small uncertainties in the CDMS charge calibration[60] or small differences in adduction as a result of different electrospray interface conditions. This difference is much smaller than the uncertainty in mass measurements owing to adducts that can increase the measured mass of similarly sized complexes by ~1%.[63]

3.4.3 Mass Analysis and Number of Ions Trapped

In order to evaluate whether the presence of multiple ions inside the trap affects the value of the mass of RuBisCO obtained from these experiments, these data were analyzed separately based on the number of ions that were trapped. These data are shown in Figure 3.2b-3.2g and the masses and widths of these distributions are given in Table 3.1. The distribution of the number of ions that are trapped is not Poisson owing to variations in ion current, both intentional variations and as a result of natural fluctuations in the electrospray during the course of the experiment. A linear fit of the centroid of these mass histograms as a function of the number of trapped ions results in a R^2 value of 0.0016 indicating that the measured mass does not depend on the number of ions trapped within the limits of our ability to obtain mass values from these data.

Ion-ion interactions could potentially adversely affect stable orbits of ions inside the trap leading to more frequent ion loss. In order to determine whether the number of ions that are trapped has any effect on the ion trapping duration, the average trapping time of ions was determined as a function of the number of ions trapped (Table 3.1). These data show that the simultaneously trapped multiply charged ions (average 49+ charges) do not interact sufficiently to cause a measurable effect on the ion trapping lifetimes for the 1.0 s maximum duration of these measurements.

Ion-ion interactions depend on ion charge. In order to determine if there are any measurable perturbations in the charge-state distributions as a result of the number of ions that are trapped, bovine serum albumin (BSA; 66.5 kDa) was analyzed using multi-ion CDMS. This protein was chosen because the charge-state distribution is readily resolved. This necessitates lowering the spread of energies of ions entering the trap to a range of ~206-214 eV, which is done using the turning quadrupole. This reduces the ability to multiplex on the basis of ion energy. The m/z distribution from all ions (Figure 3.3a) and the distributions from trapping events that contain between 2 and 6+ ions are shown in Figure 3.3b – 3g. There is no apparent variation in the abundance of each charge state that depends on the number of ions in the trapping event. For these data only, frequencies are converted to m/z by using the average ion energy. For small proteins with relatively low charge states, such as BSA here, more accurate masses can be obtained by introducing a narrow bandwidth of energies and using the mean energy to calculate m/z. Thus, the applicability of our method to introduce a broad energy spread of ions and decouple ion frequency and m/z measurements is best suited to larger ions that are more highly charged.

As is the case for RuBisCO, the mass measurement does not depend on the number of ions trapped (Supporting Information). These BSA ions have lower charge states (+13 – +16) than those of RuBisCO (+48 – +52), which reduces ion-ion interactions. However, the frequencies are not distributed as fully in frequency space owing to the narrower energy bandwidth, which increases the probability of interference between ion signals and may also increase ion-ion interactions. These data show that ion-ion interactions resulting from simultaneously trapped ions do not adversely affect the frequency spectrum, mass measurement or trapping times under the conditions of these experiments.

3.4.4 Gain in Analysis Speed

To illustrate potential gains in analysis speed, a 360 s segment of data was acquired with relatively high ion currents to enhance the probability of trapping multiple ions. A total of 1983 ions were trapped for at least 100 ms in these 360 trapping events corresponding to an average of about four ions trapped per event. A total of 1050 of these ions lasted for the full one second trap time and did not overlap in frequency with other ions. Approximately 15% of the initial 1983 ions were discarded due to overlapping ion signals in these data. The mass histogram obtained from these data is similar to that shown in Figure 3.2a with a centroid at 519 kDa. In contrast, only 360 x 0.37 = 133 ions could be weighed if this measurement was restricted to conventional single ion analysis with an optimized ion current. If the same proportion of ions are lost or dissociate in the single ion data i.e. do not last the full 1 s, then only ~90 ions would be weighed in this same time period. Thus, our multi ion multiplexing method makes possible over a 10-fold improvement in analysis speed over ideal single ion analysis. Further gains can almost certainly be made by using an ion current that optimizes the ratio of the number of ions trapped to the number of overlapping ion traces and by widening the energy range of ions that are trapped. Improvements to the data analysis algorithm, including more rigorous treatment of ions with overlapping frequencies, will also increase the number of usable ion signals in each trapping event. A further decrease in analysis time could be obtained in tandem with any of these methods by reducing the length of the trapping events, making it possible to acquire more data in a given time period albeit with reduced mass precision. Trade-offs in analysis time and performance are common with measurements where time-domain data are acquired, such as FT/ICR and orbitrap MS.

3.5 Conclusions

A method for multiplexing the measurement and analysis of masses of individual ions that are simultaneously trapped in CDMS is demonstrated. An important feature of this method is the ability to analyze the energy of each ion throughout the trap time, which makes it possible to introduce and trap ions that have a broad range of energies. Thus, ions with the exact same m/z can have a range of frequencies so that it is less likely that their signals will overlap. Although multiple single ion analysis has been demonstrated previously with FT-ICR[16] and orbitrap[25, 26] instruments, ions that have identical m/z have the same frequency so overlap of ions in a limited charge-state distribution of a pure sample is significantly more probable than with our CDMS method. Moreover, the motion of ions with the same m/z in our multiplexing CDMS method is not coherent, which further reduces the probability of ion-ion interactions. It was previously believed that analysis of more than one highly charged ion inside of an electrostatic ion trap would lead to interferences in signal owing to ion-ion interactions and thus analysis of multiple ions has previously been avoided.[29] We show that for RuBisCO ions with an average of 49+ charges each and with up to 21 ions trapped, ion-ion interactions do not adversely affect m/z or mass measurements provided that the ion signals do not overlap, a process made less likely by spreading the ion signal over frequency space using a broad range of ion energies. Moreover, there is no measurable difference in ion trapping events with multiple ions, indicating that ion-ion effects do not lead to ion loss for trap times up to 1.0 s under these conditions.

Many factors influence the mass measuring accuracy of CDMS. With longer trapping times and more accurate frequency measurements that could be achieved at lower pressures and with improved trap designs, ion-ion interactions may ultimately limit the mass measuring accuracy of our method. Because it is essential to weigh many ions in order to analyze more complex

mixtures, particularly when the analysis requires a high dynamic range owing to concentration differences, long trapping times are less likely to be used in most applications. Shorter trapping times also decrease the likelihood of ion overlap events that occur due to frequency shifting, enabling further multiplexing. Larger ions that are more highly charged will experience more ion-ion interactions and the optimum number of trapped ions will almost certainly depend the range of the m/z and charge states of the ions that are trapped.

The analytes measured in this work can also be readily weighed using conventional mass spectrometers in which ensembles of many ions are measured. These analytes were chosen to demonstrate that simultaneous multiple single ion measurements are possible in CDMS and to illustrate a new method that decouples the frequency and m/z measurements by measuring the energy of each ion throughout the measurement. This CDMS method will be most useful for complex mixtures of large molecules or even relatively pure very high mass compounds that are not amenable to analysis using conventional mass spectrometers.

In these experiments, the individual masses of up to 13 ions were measured in one trapping event and up to 21 ions were trapped in a single event. The multiplexing demonstrated here with an average of ~4 ions measured simultaneously leads to about an order of magnitude improvement in the analysis speed compared to optimum single ion experiments. Moreover, this multiplexing method is relatively insensitive to ion current – higher currents lead to more trapped ions but data from all trapping events can be used provided that the ion current is sufficiently high. If the maximum of 13 mass values for ions measured in a single ion trapping event demonstrated here were an average value for all trapping events, up to a 35-fold improvement in measurement speed would be possible over the conventional single ion method. The ability to multiplex depends on many factors, but further gains in measurement speed should be possible by trapping and analyzing data for an even larger number of simultaneously trapped ions and by further increasing the energy spread of ions that are trapped. The optimum number of ions in these experiments and factors that affect these values are currently under investigation.

3.6 Acknowledgements

This material is based upon work supported by the National Science Foundation under CHE-1609866. D.F.S. and L.M.O were supported by the US Department of Energy Grant DE-SC00016240.

3.7 References

(1) Loo, J. A. Electrospray Ionization Mass Spectrometry: A Technology for Studying Noncovalent Macromolecular Complexes. *Int. J. Mass Spectrom.* **2000**, *200* (1–3), 175–186.

(2) Heck, A. J. R.; Van Den Heuvel, R. H. H. Investigation of Intact Protein Complexes by Mass Spectrometry. *Mass Spectrom. Rev.* **2004**, *23* (5), 368–389.

(3) Hernández, H.; Robinson, C. V. Determining the Stoichiometry and Interactions of Macromolecular Assemblies from Mass Spectrometry. *Nat. Protoc.* **2007**, *2* (3), 715–726.

(4) Painter, A. J.; Jaya, N.; Basha, E.; Vierling, E.; Robinson, C. V.; Benesch, J. L. P. Real-Time Monitoring of Protein Complexes Reveals Their Quaternary Organization and Dynamics. *Chem. Biol.* **2008**, *15* (3), 246–253.

(5) Kintzer, A. F.; Sterling, H. J.; Tang, I. I.; Abdul-Gader, A.; Miles, A. J.; Wallace, B. A.; Williams, E. R.; Krantz, B. A. Role of the Protective Antigen Octamer in the Molecular Mechanism of Anthrax Lethal Toxin Stabilization in Plasma. *J. Mol. Biol.* **2010**, *399* (5), 741–758.

(6) Han, L.; Hyung, S. J.; Mayers, J. J. S.; Ruotolo, B. T. Bound Anions Differentially Stabilize Multiprotein Complexes in the Absence of Bulk Solvent. *J. Am. Chem. Soc.* **2011**, *133* (29), 11358–11367.

(7) Sperry, J. B.; Ryan, Z. C.; Kumar, R.; Gross, M. L. Hydrogen/Deuterium Exchange Reflects Binding of Human Centrin 2 to Ca 2+ and Xeroderma Pigmentosum Group C Peptide: An Example of EX1 Kinetics. *Int. J. Mass Spectrom.* **2012**, *330–332*, 302–309.

(8) Cheng, X.; Bakhtiar, R.; Van Orden, S.; Smith, R. D. Charge-State Shifting of Individual Multiply-Charged Ions of Bovine Albumin Dimer and Molecular Weight Determination Using an Individual-Ion Approach. *Anal. Chem.* **1994**, *66* (13), 2084–2087.

(9) Susa, A. C.; Xia, Z.; Williams, E. R. Native Mass Spectrometry from Common Buffers with Salts That Mimic the Extracellular Environment. *Angew. Chemie - Int. Ed.* **2017**, *56* (27), 7912–7915.

(10) Susa, A. C.; Xia, Z.; Williams, E. R. Small Emitter Tips for Native Mass Spectrometry of Proteins and Protein Complexes from Nonvolatile Buffers That Mimic the Intracellular Environment. *Anal. Chem.* **2017**, *89* (5), 3116–3122.

(11) Lössl, P.; Snijder, J.; Heck, A. J. R. Boundaries of Mass Resolution in Native Mass Spectrometry. *J. Am. Soc. Mass Spectrom.* **2014**, *25* (6), 906–917.

(12) McKay, A. R.; Ruotolo, B. T.; Ilag, L. L.; Robinson, C. V. Mass Measurements of Increased Accuracy Resolve Heterogeneous Populations of Intact Ribosomes. *J. Am. Chem. Soc.* **2006**, *128* (35), 11433–11442.

(13) Aquilina, J. A.; Benesch, J. L. P.; Bateman, O. A.; Slingsby, C.; Robinson, C. V. Polydispersity of a Mammalian Chaperone: Mass Spectrometry Reveals the Population of Oligomers in AB-Crystallin. *Proc. Natl. Acad. Sci. U. S. A.* **2003**, *100* (19), 10611–10616.

(14) Jurchen, J. C.; Williams, E. R. Origin of Asymmetric Charge Partitioning in the Dissociation of Gas-Phase Protein Homodimers. *J. Am. Chem. Soc.* **2003**, *125* (9), 2817–2826.

(15) Hanay, M. S.; Kelber, S. I.; O'Connell, C. D.; Mulvaney, P.; Sader, J. E.; Roukes, M. L. Inertial Imaging with Nanomechanical Systems. *Nat. Nanotechnol.* **2015**, *10* (4), 339–344.

(16) Smith, R. D.; Cheng, X.; Brace, J. E.; Hofstadler, S. A.; Anderson, G. A. Trapping, Detection and Reaction of Very Large Single Molecular Ions by Mass Spectrometry. *Nature* **1994**, *369* (6476), 137–139.

(17) Wuerker, R. F.; Shelton, H.; Langmuir, R. V. Electrodynamic Containment of Charged Particles. *J. Appl. Phys.* **1959**, *30* (3), 342–349.

(18) Philip, M. A.; Gelbard, F.; Arnold, S. An Absolute Method for Aerosol Particle Mass and Charge Measurement. *J. Colloid Interface Sci.* **1983**, *91* (2), 507–515.

(19) Hars, G.; Tass, Z. Application of Quadrupole Ion Trap for the Accurate Mass Determination of Submicron Size Charged Particles. *J. Appl. Phys.* **1995**, *77* (9), 4245–4250.

(20) Schlemmer, S.; Illemann, J.; Wellert, S.; Gerlich, D. Nondestructive High-Resolution and Absolute Mass Determination of Single Charged Particles in a Three-Dimensional Quadrupole Trap. *J. Appl. Phys.* **2001**, *90* (10), 5410–5418.

(21) Bell, D. M.; Howder, C. R.; Johnson, R. C.; Anderson, S. L. Single CdSe/ZnS Nanocrystals in an Ion Trap: Charge and Mass Determination and Photophysics Evolution with Changing Mass, Charge, and Temperature. *ACS Nano* **2014**, *8* (3), 2387–2398.

(22) Peng, W. P.; Lin, H. C.; Lin, H. H.; Chu, M.; Yu, A. L.; Chang, H. C.; Chen, C. H. Charge-Monitoring Laser-Induced Acoustic Desorption Mass Spectrometry for Cell and Microparticle Mass Distribution Measurement. *Angew. Chemie - Int. Ed.* **2007**, *46* (21), 3865–3869.

(23) Twerenbold, D. Biopolymer Mass Spectrometer with Cryogenic Particle Detectors. *Nucl. Instruments Methods Phys. Res. Sect. A Accel. Spectrometers, Detect. Assoc. Equip.* **1996**, *370* (1), 253–255.

(24) Sipe, D. M.; Plath, L. D.; Aksenov, A. A.; Feldman, J. S.; Bier, M. E. Characterization of Mega-Dalton-Sized Nanoparticles by Superconducting Tunnel Junction Cryodetection Mass Spectrometry. *ACS Nano* **2018**, *12* (3), 2591–2602.

(25) Makarov, A.; Denisov, E. Dynamics of Ions of Intact Proteins in the Orbitrap Mass Analyzer. *J. Am. Soc. Mass Spectrom.* **2009**, *20* (8), 1486–1495.

(26) Kafader, J. O.; Melani, R. D.; Senko, M. W.; Makarov, A. A.; Kelleher, N. L.; Compton, P. D. Measurement of Individual Ions Sharply Increases the Resolution of Orbitrap Mass Spectra of Proteins. *Anal. Chem.* **2019**, *91* (4), 2776–2783.

(27) Barney, B. L.; Pratt, S. N.; Austin, D. E. Survivability of Bare, Individual Bacillus Subtilis Spores to High-Velocity Surface Impact: Implications for Microbial Transfer through Space. *Planet. Space Sci.* **2016**, *125*, 20–26.

(28) Benner, W. H. A Gated Electrostatic Ion Trap to Repetitiously Measure the Charge and m/z of Large Electrospray Ions. *Anal. Chem.* **1997**, *69* (20), 4162–4168.

(29) Keifer, D. Z.; Pierson, E. E.; Jarrold, M. F. Charge Detection Mass Spectrometry: Weighing Heavier Things. *Analyst* **2017**, *142* (10), 1654–1671.

(30) Keifer, D. Z.; Jarrold, M. F. Single-Molecule Mass Spectrometry. *Mass Spectrom. Rev.* **2017**, *36* (6), 715–733.

(31) Doussineau, T.; Bao, C. Y.; Antoine, R.; Dugourd, P.; Zhang, W.; D'Agosto, F.; Charleux, B. Direct Molar Mass Determination of Self-Assembled Amphiphilic Block Copolymer Nanoobjects Using Electrospray-Charge Detection Mass Spectrometry. *ACS Macro Lett.* **2012**, *1* (3), 414–417.

(32) Elliott, A. G.; Merenbloom, S. I.; Chakrabarty, S.; Williams, E. R. Single Particle Analyzer of Mass: A Charge Detection Mass Spectrometer with a Multi-Detector Electrostatic Ion Trap. *Int. J. Mass Spectrom.* **2017**, *414*, 45–55.

(33) Shelton, H.; Hendricks, C. D.; Wuerker, R. F. Electrostatic Acceleration of Microparticles to Hypervelocities. *J. Appl. Phys.* **1960**, *31* (7), 1243–1246.

(34) Keaton, P. W.; Idzorek, G. C.; Rowton, L. J.; Seagrave, J. D.; Stradling, G. L.; Bergeson, S. D.; Collopy, M. T.; Curling, H. L.; McColl, D. B.; Smith, J. D. A Hypervelocity - Microparticle - Impacts Laboratory with 100-Km/s Projectiles. *Int. J. Impact Eng.* **1990**, *10* (1–4), 295–308.

(35) Stradling, G. L.; Idzorek, G. C.; Shafer, B. P.; Curling, H. L.; Collopy, M. T.; Blossom, A. A. H.; Fuerstenau, S. Ultra-High Velocity Impacts: Cratering Studies of Microscopic Impacts from 3 Km/s to 30 Km/S. *Int. J. Impact Eng.* **1993**, *14* (1–4), 719–727.

(36) Adamson, B. D.; Miller, M. E. C.; Continetti, R. E. The Aerosol Impact Spectrometer: A Versatile Platform for Studying the Velocity Dependence of Nanoparticle-Surface Impact Phenomena. *EPJ Tech. Instrum.* **2017**, *4* (1), 1–17.

(37) Fuerstenau, S. D.; Benner, W. H. Molecular Weight Determination of Megadalton DNA Electrospray Ions Using Charge Detection Time-of-flight Mass Spectrometry. *Rapid Commun. Mass Spectrom.* **1995**, *9* (15), 1528–1538.

(38) Doussineau, T.; Mathevon, C.; Altamura, L.; Vendrely, C.; Dugourd, P.; Forge, V.; Antoine, R. Mass Determination of Entire Amyloid Fibrils by Using Mass Spectrometry. *Angew. Chemie - Int. Ed.* **2016**, *55* (7), 2340–2344.

(39) Barney, B. L.; Austin, D. E. Dynamics of Rebounding Bacillus Subtilis Spores Determined Using Image-Charge Detection. *J. Biol. Phys.* **2017**, *43* (4), 481–492.

(40) Hogan, J. J.; Hendricks, C. D. Investigation of the Charge-to-Mass Ratio of Electrically Sprayed Liquid Particles. *AIAA J.* **1965**, *3* (2), 296–301.

(41) Contino, N. C.; Jarrold, M. F. Charge Detection Mass Spectrometry for Single Ions with a Limit of Detection of 30 Charges. *Int. J. Mass Spectrom.* **2013**, *345–347*, 153–159.

(42) Hogan, J. A.; Jarrold, M. F. Optimized Electrostatic Linear Ion Trap for Charge Detection Mass Spectrometry. *J. Am. Soc. Mass Spectrom.* **2018**, *29* (10), 2086–2095.

(43) Elliott, A. G.; Harper, C. C.; Lin, H. W.; Williams, E. R. Mass, Mobility and MSN Measurements of Single Ions Using Charge Detection Mass Spectrometry. *Analyst* **2017**, *142* (15), 2760–2769.

(44) Antoine, R.; Doussineau, T.; Dugourd, P.; Calvo, F. Multiphoton Dissociation of

Macromolecular Ions at the Single-Molecule Level. *Phys. Rev. A - At. Mol. Opt. Phys.* **2013**, *87* (1), 013435.

(45) Lutomski, C. A.; Gordon, S. M.; Remaley, A. T.; Jarrold, M. F. Resolution of Lipoprotein Subclasses by Charge Detection Mass Spectrometry. *Anal. Chem.* **2018**, *90* (11), 6353–6356.

(46) Lutomski, C. A.; Lyktey, N. A.; Pierson, E. E.; Zhao, Z.; Zlotnick, A.; Jarrold, M. F. Multiple Pathways in Capsid Assembly. *J. Am. Chem. Soc.* **2018**, *140* (17), 5784–5790.

(47) Pierson, E. E.; Keifer, D. Z.; Contino, N. C.; Jarrold, M. F. Probing Higher Order Multimers of Pyruvate Kinase with Charge Detection Mass Spectrometry. *Int. J. Mass Spectrom.* **2013**, *337*, 50–56.

(48) Lutomski, C. A.; Lyktey, N. A.; Zhao, Z.; Pierson, E. E.; Zlotnick, A.; Jarrold, M. F. Hepatitis B Virus Capsid Completion Occurs through Error Correction. *J. Am. Chem. Soc.* **2017**, *139* (46), 16932–16938.

(49) Gamero-Castão, M. Induction Charge Detector with Multiple Sensing Stages. *Rev. Sci. Instrum.* **2007**, *78* (4), 043301.

(50) Doussineau, T.; Antoine, R.; Santacreu, M.; Dugourd, P. Pushing the Limit of Infrared Multiphoton Dissociation to Megadalton-Size DNA Ions. *J. Phys. Chem. Lett.* **2012**, *3* (16), 2141–2145.

(51) Halim, M. A.; Clavier, C.; Dagany, X.; Kerleroux, M.; Dugourd, P.; Dunbar, R. C.; Antoine, R. Infrared Laser Dissociation of Single Megadalton Polymer Ions in a Gated Electrostatic Ion Trap: The Added Value of Statistical Analysis of Individual Events. *Phys. Chem. Chem. Phys.* **2018**, *20* (17), 11959–11966.

(52) Elliott, A. G.; Harper, C. C.; Lin, H. W.; Williams, E. R. Effects of Individual Ion Energies on Charge Measurements in Fourier Transform Charge Detection Mass Spectrometry (FT-CDMS). *J. Am. Soc. Mass Spectrom.* **2019**, *30* (6), 946–955.

(53) Contino, N. C.; Pierson, E. E.; Keifer, D. Z.; Jarrold, M. F. Charge Detection Mass Spectrometry with Resolved Charge States. *J. Am. Soc. Mass Spectrom.* **2013**, *24* (1), 101–108.

(54) Keifer, D. Z.; Motwani, T.; Teschke, C. M.; Jarrold, M. F. Measurement of the Accurate Mass of a 50 MDa Infectious Virus. *Rapid Commun. Mass Spectrom.* **2016**, *30* (17), 1957–1962.

(55) Keifer, D. Z.; Motwani, T.; Teschke, C. M.; Jarrold, M. F. Acquiring Structural Information on Virus Particles with Charge Detection Mass Spectrometry. *J. Am. Soc. Mass Spectrom.* **2016**, *27* (6), 1028–1036.

(56) Harper, C. C.; Elliott, A. G.; Lin, H. W.; Williams, E. R. Determining Energies and Cross Sections of Individual Ions Using Higher-Order Harmonics in Fourier Transform Charge Detection Mass Spectrometry (FT-CDMS). *J. Am. Soc. Mass Spectrom.* **2018**, *29* (9), 1861–1869.

(57) Elliott, A. G.; Harper, C. C.; Lin, H. W.; Susa, A. C.; Xia, Z.; Williams, E. R. Simultaneous Measurements of Mass and Collisional Cross-Section of Single Ions with Charge Detection Mass Spectrometry. *Anal. Chem.* **2017**, *89* (14), 7701–7708.

(58) Pierson, E. E.; Keifer, D. Z.; Asokan, A.; Jarrold, M. F. Resolving Adeno-Associated Viral Particle Diversity with Charge Detection Mass Spectrometry. *Anal. Chem.* **2016**, *88* (13), 6718–6725.

(59) Pierson, E. E.; Keifer, D. Z.; Selzer, L.; Lee, L. S.; Contino, N. C.; Wang, J. C. Y.; Zlotnick, A.; Jarrold, M. F. Detection of Late Intermediates in Virus Capsid Assembly by Charge Detection Mass Spectrometry. *J. Am. Chem. Soc.* **2014**, *136* (9), 3536–3541.

(60) Keifer, D. Z.; Pierson, E. E.; Hogan, J. A.; Bedwell, G. J.; Prevelige, P. E.; Jarrold, M. F. Charge Detection Mass Spectrometry of Bacteriophage P22 Procapsid Distributions above 20 MDa. *Rapid Commun. Mass Spectrom.* **2014**, *28* (5), 483–488.

(61) Jurchen, J. C.; Garcia, D. E.; Williams, E. R. Further Studies on the Origins of Asymmetric Charge Partitioning in Protein Homodimers. *J. Am. Soc. Mass Spectrom.* **2004**, *15* (10), 1408–1415.

(62) Wysocki, V. H.; Jones, C. M.; Galhena, A. S.; Blackwell, A. E. Surface-Induced Dissociation Shows Potential to Be More Informative Than Collision-Induced Dissociation for Structural Studies of Large Systems. *Journal of the American Society for Mass Spectrometry*. Elsevier Inc. November 22, 2008, pp 903–913.

(63) McKay, A. R.; Ruotolo, B. T.; Ilag, L. L.; Robinson, C. V. Mass Measurements of Increased Accuracy Resolve Heterogeneous Populations of Intact Ribosomes. *J. Am. Chem. Soc.* **2006**, *128* (35), 11433–11442.

3.8 Table and Figures

Table 3.1. Mass and Average Trapping Lifetimes of RuBisCO Obtained by CDMS Measurements for All Ions and for Events with 1 Through 6+ Simultaneously Trapped Ions

# Ions Simultaneously Trapped	Mass (Da)	Standard Deviation of Gaussian Fit (Da)	Average Trapping Lifetime (ms)
All	517,312	13,005	762.4
1	516,956	11,437	758.3
2	517,143	13,995	761.5
3	517,914	13,673	764.6
4	517,509	11,721	761.0
5	516,435	12,095	756.9
6+	517,385	13,200	766.8

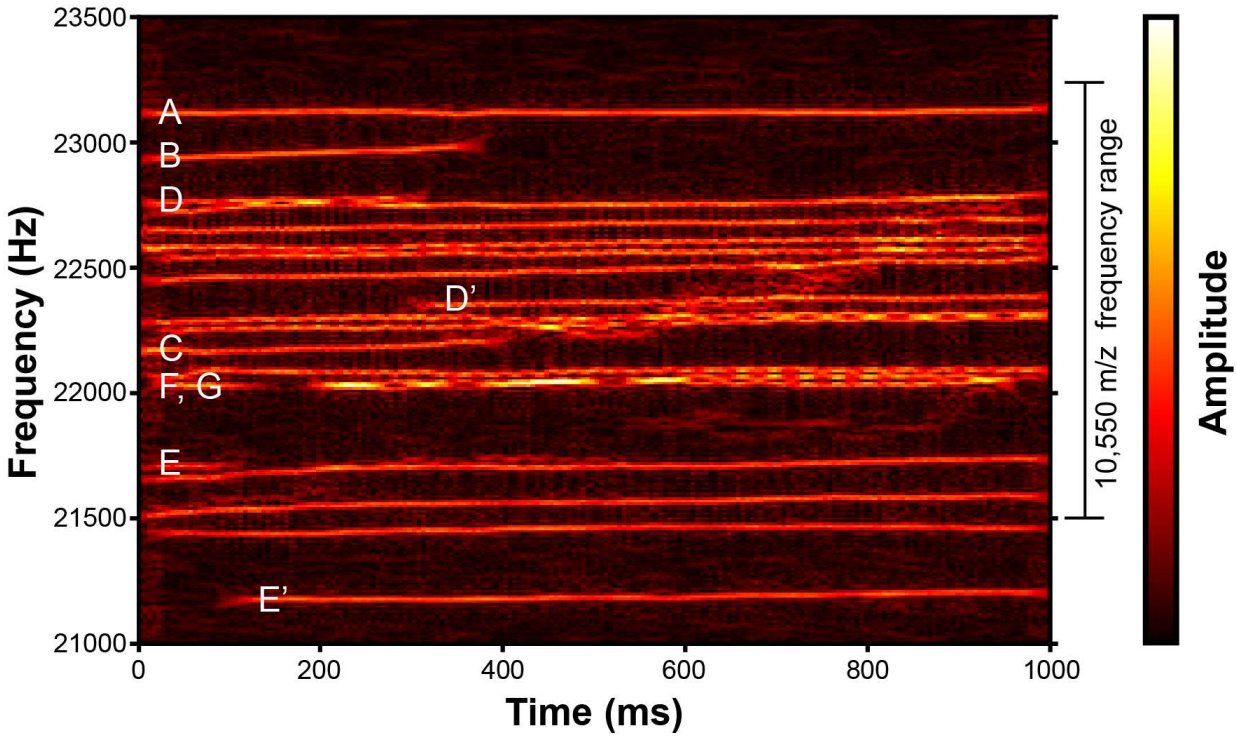


Figure 3.1. Results from a short-time Fourier transform of a single 1.0 s trapping event using 50 ms segments showing traces for RuBisCO ions (517 kDa) formed by electrospray ionization. Eighteen ions were initially trapped for at least 100 ms; some ions last the entire 1.0 s trapping time (**A**) without overlap resulting in mass measurements of 11 ions, some enter unstable orbits and are either lost (**B**) or undergo significant frequency changes (**C**), some dissociate (**D/D'**, **E/E'**) and others overlap in signal (**F**, **G**). The bracket indicates the frequency range (1750 Hz) that an ion at *m/z* = 10,550 can have within the range of ion energies introduced and trapped in these experiments.

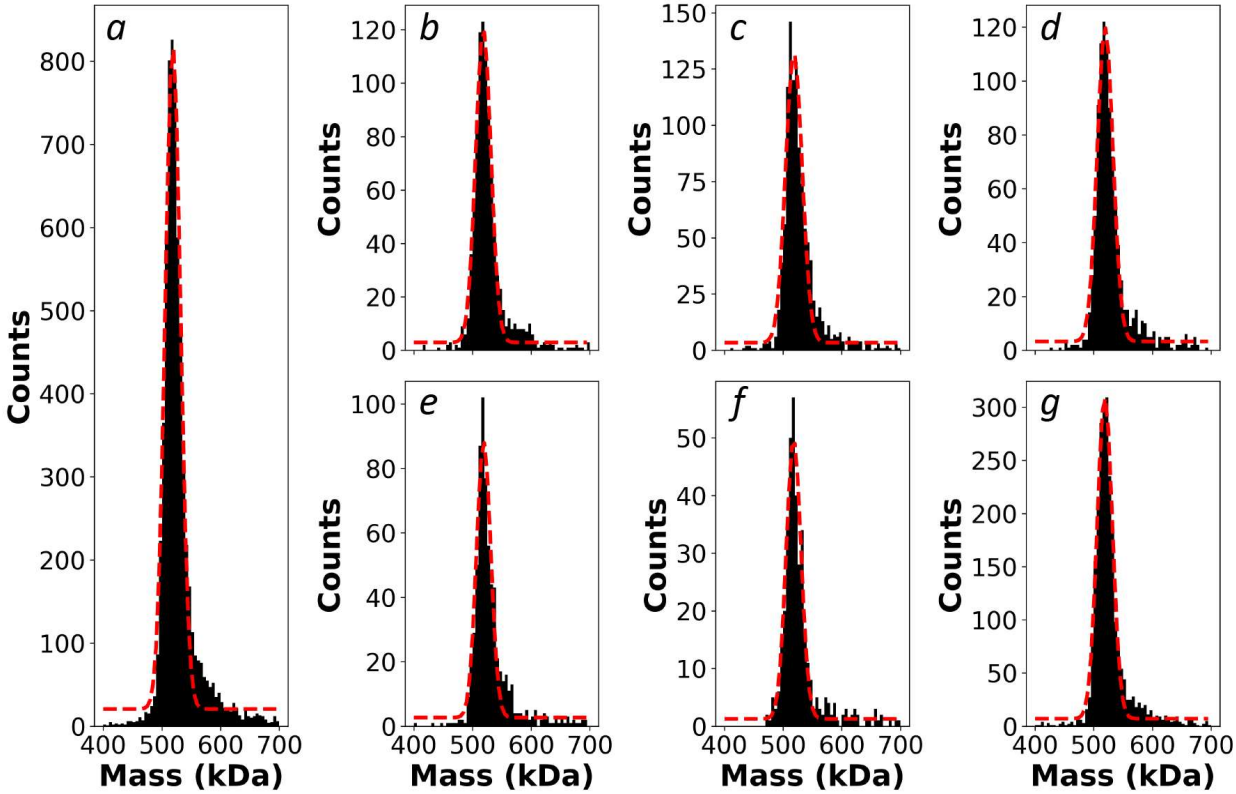


Figure 3.2. CDMS mass histograms of RuBisCO ions formed by electrospray ionization consisting of (**a**) all 6988 ions weighed and these data shown separately for ion trapping events where 1 through 6+ ions were simultaneously trapped (**b** through **g**, respectively). A Gaussian fit (red) was used to find the peak centroid corresponding to the reported mass of the complex. A linear fit of the peak centroids for (**b**) through (**g**) as a function of number of ions trapped results in R^2 value of 0.0016 indicating that the measured mass does not depend on the number of ions that are simultaneously trapped.

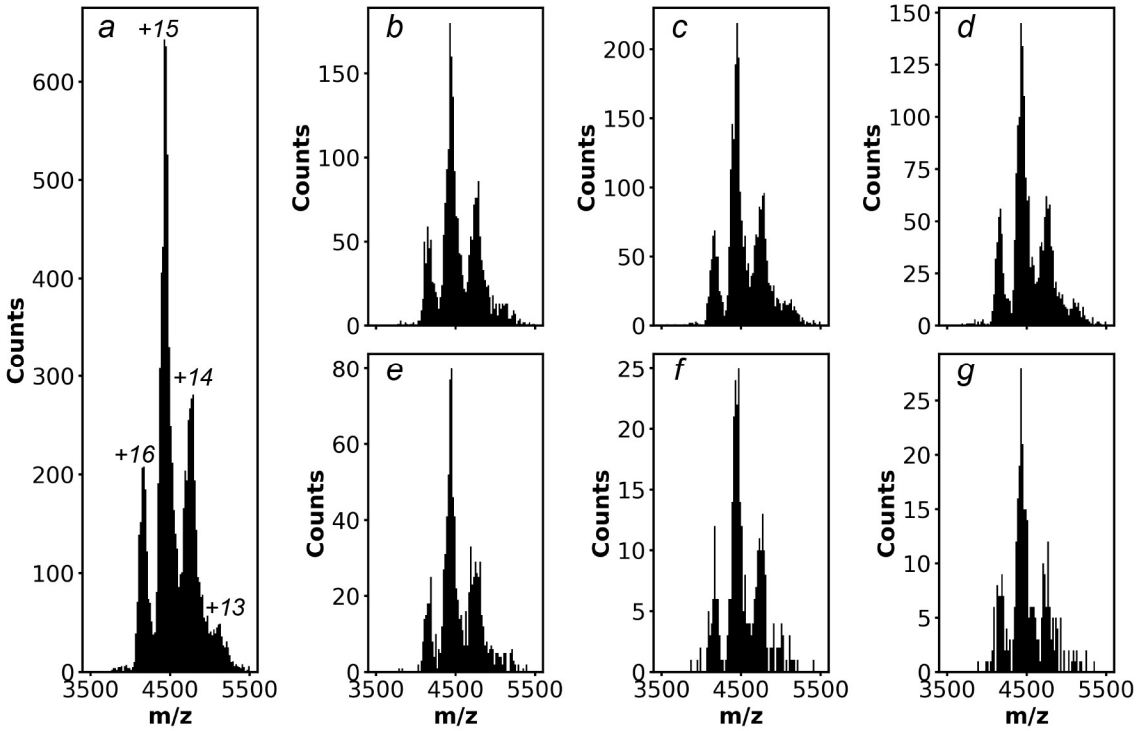


Figure 3.3. CDMS *m*/*z* histogram of bovine serum albumin (66.5 kDa) formed by electrospray ionization showing charge-state distributions resulting from (**a**) all measurements and from measurements where 1 through 6+ ions were simultaneously trapped (**b** through **g**, respectively). Neither the charge-state distributions nor the masses obtained from these data depend on the number of trapped ions. For these data only, frequencies are converted to *m*/*z* by using the average ion energy.

3.9 Supporting Information

3.9.1 Quadrupole-Time of Flight (Q-TOF) Mass Spectrometry of RuBisCO

The RuBisCO sample was analyzed using a Waters Micromass Q-TOF mass spectrometer. Mass spectra of the whole complex (Figure S3.1a) and the large subunit (CbbL, 51.9 kDa) and small subunit (CbbS, 12.7 kDa) substituent proteins (S3.1b) formed from the fragmentation of the whole complex using collision induced dissociation (CID) are shown in Figure S3.1. A deconvolution of the mass spectrum in S3.1a is shown in Figure S3.2. The standard deviation of Gaussian least squares fit to the deconvolved data is 1,700 Da, likely due to adduction and incomplete desolvation. This width is smaller than the width of the mass distribution (13 kDa) measured by charge detection mass spectrometry (CDMS), but suggests that at least a portion of the width of the mass peaks in Figure 3.2 is due to sample heterogeneity and adducts. The additional width of the CDMS mass histogram is likely due to uncertainties in ion energy and charge stemming from varying ion trajectories and the relatively low S/N in the Fourier transform for the charge states of RuBisCO (+48 – +52). Longer trapping times could therefore decrease the CDMS peak width somewhat; however, sample heterogeneity will ultimately limit the improvement that can be made.

3.9.2 Bovine Serum Albumen (BSA) CDMS Measurements

A mass histogram for BSA containing all data for all trapping events independent of the number of ions that were trapped is shown in Figure S3.3a. Figure S3.3b-S3.3g shows the data for trapping events containing different numbers of ions. Similar to the RuBisCO sample shown in Figure 3.2, the centroids of each distribution were determined using a Gaussian fit. A linear fit of these centroid data yields and R^2 value of 0.0031, indicating that the measured mass for BSA also does not depend on the number of ions simultaneously trapped and analyzed. The centroid values, standard deviations, and average trapping lifetime data for BSA are contained in Table S3.1. The larger relative standard deviations (~5.0% for all ions) for BSA compared to Rubisco (~2.5%) are due to the lower charge of the BSA ions. The uncertainties in the individual ion charge and ion energy measurements both depend on the S/N ratio for signal peaks in the Fourier transform. Lower charge ions have lower S/N and therefore have higher relative uncertainties. Shorter average trapping lifetimes are also observed for BSA compared to RuBisCO. This effect can be attributed to the smaller mass of BSA; smaller ions are more easily destabilized by collisions with background gas and are therefore lost more quickly on average.

3.10 Supporting Table and Figures

Table S3.1. Mass and Average Trapping Lifetimes of BSA Obtained by CDMS Measurements for All Ions and for Events with 1 Through 6+ Simultaneously Trapped Ions

# Ions Simultaneously Trapped	Mass (Da)	Standard Deviation of Gaussian Fit (Da)	Average Trapping Lifetime (ms)
All	66,991	3,338	573.2
1	66,957	3,374	562.4
2	66,968	3,358	568.8
3	67,122	3,256	574.1
4	66,784	3,297	563.1
5	67,318	3,225	553.6
6+	66,855	3,582	569.8

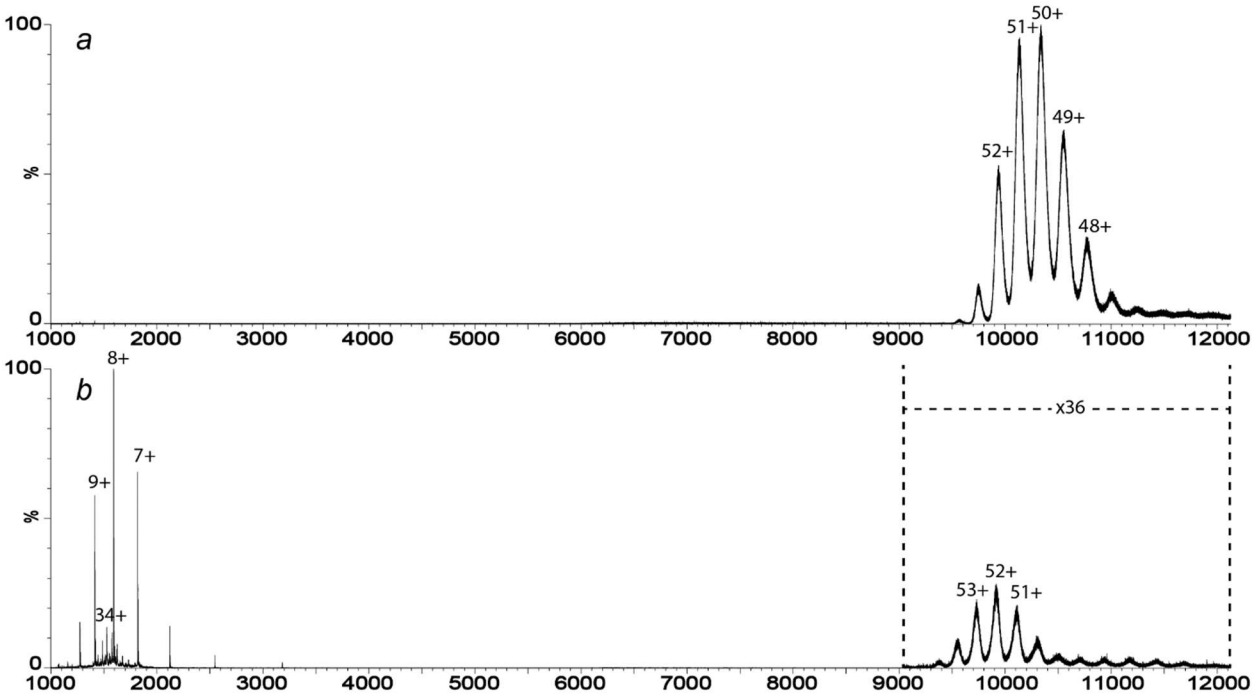


Figure S3.1. Mass spectra of whole RuBisCO complex before (**a**) and after (**b**) CID. The mass determined for RuBisCO in (**a**, 517 kDa) was confirmed by analysis of the small chain (12.7 kDa, 7+ – 9+ labeled) and large chain (51.9 kDa, +34 labeled) CID product ions appearing at lower *m*/*z* in (**b**).

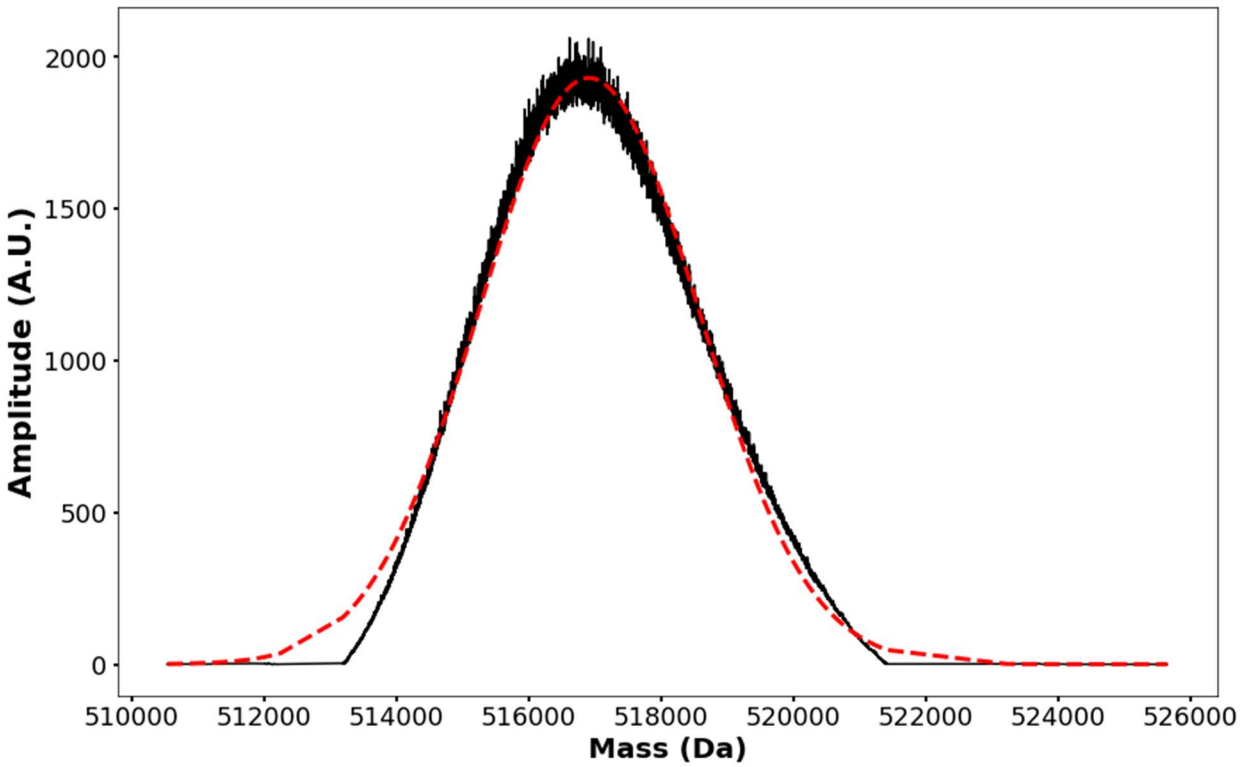


Figure S3.2. The deconvolved mass spectrum of the data shown in Figure S1a. A Gaussian fit of these data yields a centroid mass of 516,900 ± 100 Da. The standard deviation of these data is 1,700 Da, a width that originates from the intrinsic sample heterogeneity and salt adduction.

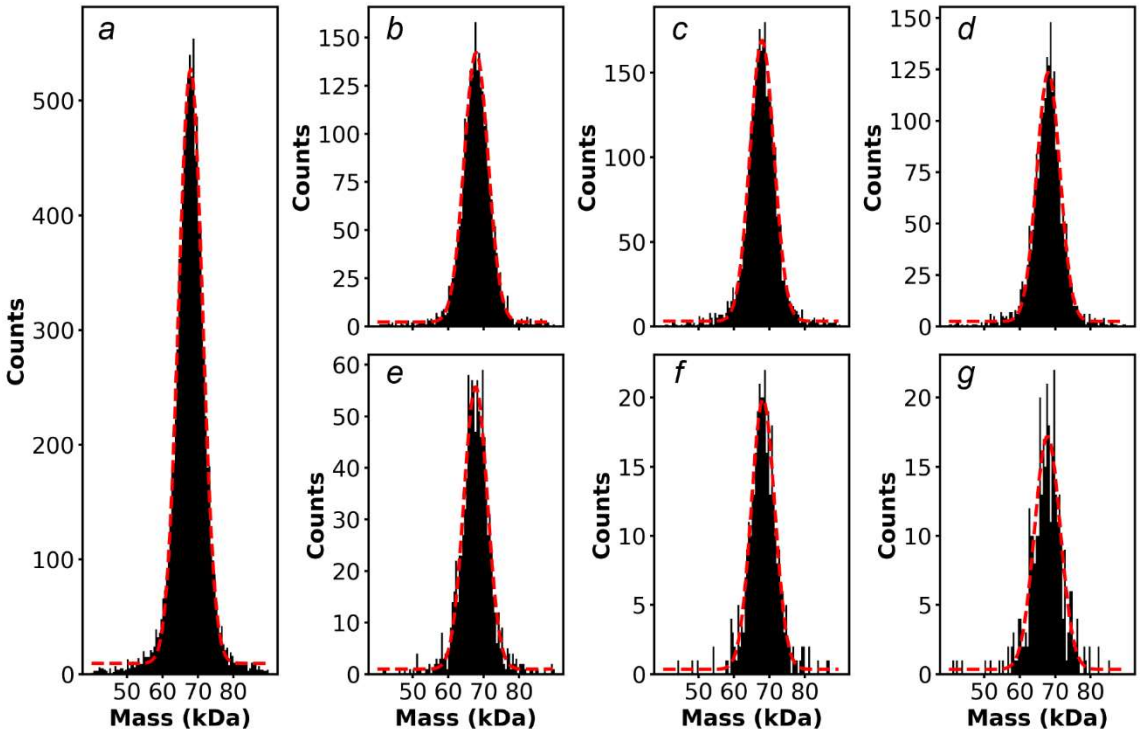


Figure S3.3. CDMS mass histograms of BSA ions formed by electrospray ionization consisting of (**a**) all 9637 ions weighed and these data shown separately for ion trapping events where 1 through 6+ ions were simultaneously trapped (**b** through **g**, respectively). A Gaussian fit (red) was used to find the peak centroid corresponding to the reported mass of the complex. A linear fit of the peak centroids for (**b**) through (**g**) as a function of number of ions trapped results in R^2 value of 0.0031 indicating that the measured mass does not depend on the number of ions that are simultaneously trapped.

Chapter 4

Enhanced Multiplexing in Fourier Transform Charge Detection Mass Spectrometry by Decoupling Ion Frequency from Mass to Charge Ratio

This chapter is reproduced with permission from:

Conner C. Harper and Evan R. Williams

"Enhanced Multiplexing in Fourier Transform Charge Detection Mass Spectrometry by Decoupling Ion Frequency from Mass to Charge Ratio" *J. Am. Soc. Mass Spectrom.* **2019**, *30*, 2637-2645.

© 2019 American Society for Mass Spectrometry

4.1 Abstract

Weighing single ions with charge detection mass spectrometry (CDMS) makes it possible to obtain the masses of molecules of essentially unlimited size even in highly heterogeneous samples, but producing a mass histogram that is representative of all of the components in a mixture requires substantial measurement time. Multiple ions can be trapped to reduce analysis time but ion signals can overlap. To determine the maximum gains in analysis speed possible with current instrumentation with multiple ion trapping, simulations calculating the frequency and overlap rate of ions with different mass, charge, and energy ranges were performed. For an analyte with a broad mass distribution, such as long chain polyethylene glycol (PEG, 8 MDa), gains in analysis speed of up to 160 times that of prior CDMS experiments are possible. For signals from homogeneous samples, ions with the same m/z have frequencies that overlap and interfere, reducing the effectiveness of multiplexing in experiments where ions have the same energy per charge. We show that by maximizing the decoupling of ion m/z from frequency using a broad range of ion energies, the rate of signal overlap is significantly reduced making it possible to trap more ions. Under optimum decoupling conditions, a measurement speed nearly 50 times greater than that of prior CDMS experiments is possible for RuBisCO (517 kDa). The reduction in overlap due to decoupling also results in more accurate quantitation in samples that contain multiple analytes with different concentrations.

4.2 Introduction

Native mass spectrometry, in which ions of biomolecular molecules and associated macromolecular complexes are produced by electrospray ionization from aqueous solutions

containing 100+ mM concentrations of salts[1,2] is widely used to obtain structural information about molecular ions formed from environments in which they have native structures and reactivities.[3] Information about the stoichiometries and structures of complexes can be obtained from tandem mass spectrometry experiments in which mass selected precursor ions are activated, either through collisions with gaseous molecules or with surfaces, and the resulting fragment ions, typically consisting of intact monomer subunits or sub-assemblies are mass analyzed.[4,5] A key challenge in extending the mass range of analytes amendable to such measurements is the need to resolve individual charge states in order to obtain molecular weight information from larger species, such as intact viruses.[6] This is particularly challenging for complex samples, such as synthetic polymers[7,8] or intrinsically heterogeneous macromolecular complexes, where charge-state distributions of the individual components in the mixture are unresolved.[9] Signals for each component in an ensemble measurement can overlap and can lead to loss of resolved signal. In these cases, tandem mass spectrometry performed on a narrow range of *m*/*z* precursors can spread out the fragment ion signal over a wider range of *m*/*z* enabling some mass information to be obtained.[9,10]

One method to overcome the problem of heterogeneity is to mass analyze individual ions so that the measurement of one ion does not interfere with the measurement of another. Single molecule mass measurements have been demonstrated using a variety of different methods, including nanoelectromechanical systems[11,12] and with various types of mass spectrometers, including Fourier-transform ion cyclotron resonance (FTICR),[13,14] Orbitrap,[15,16] ion trap,[17–21] cryodetector time-of-flight,[22,23] and charge detection mass spectrometry (CDMS).[24–30] Several of these mass spectrometry methods can provide high mass measuring accuracy but this typically comes at the expense of analysis time. Kafader et al. demonstrated a resolving power of 677,000 from single ion measurements in an Orbitrap mass spectrometer for the protein carbonic anhydrase using ~250 ms measurement times, but found that there was significant ion decay for species over 40 kDa which resulted in "hours of total acquisition time to produce a composite mass spectrum with statistically meaningful isotopic distributions".[16]

In order to obtain useful information about the composition of heterogeneous samples, the masses of many individual ions must be measured.[26] Thus, analysis speed is essential for practical single ion measurements. Single ion Fourier transform charge detection mass spectrometry (FT-CDMS), in which individual ions are confined in an electrostatic ion trap and the *m*/*z* of each ion is obtained from its oscillation frequency, can provide useful mass measurements from molecules of essentially unlimited size, ranging from small proteins up to particles with masses well above 100 MDa.[26,31–39] Detection and mass accuracy depend on a number of factors, including the ion charge and trap time, but useful measurements can be made in about 100 ms,[31,32,34,40] although longer trapping times are often used for improved mass measurements[41] or to obtain single ion collisional cross sections[38,39] or MS^n information[37] in combination with the measurements of individual ion masses. Because large macromolecules and macromolecular complexes typically have a large number of non-volatile salts and often solvent molecules attached, the masses of large complexes that can be measured in conventional mass spectrometers are often higher than those of the computed masses. Robinson and co-workers have reported a widely used method, which relates the peak width of a charge state to the extent of adduction to provide a "corrected" mass of the unadducted complex [9]. The mass attributed to adduction can account for more than ~1% of the overall measured mass for large protein assemblies weighing 385-800 kDa.[9] The extent to which large molecules and complexes are adducted limits the overall need for high mass measuring

accuracy because the ultimate mass accuracy is limited by any correction method for larger ions.[6,9] Thus, a mass accuracy of less than 0.1%, readily achievable in CDMS with 100 ms trap times and samples of 1000+ ions,[26,42,43] should not limit the overall mass accuracy with which large complexes, polymers, or viruses can be weighed.

Even with a 100 ms trap time, the number of ions that can be measured per second is limited by weighing just one ion at a time. Until recently, it was believed that single ion trapping events were required in FT-CDMS. Jarrold and co-workers state: "…multiple ion trapping events cannot be analyzed because two highly charged ions trapped together interact and perturb the oscillation frequencies. Hence, only single ion trapping events are useful".[26] In order to achieve the optimum single ion trapping conditions, the ion current has to be carefully regulated so that a single ion is trapped in only 37% of the measurements.[26,44] Lower currents lead to fewer single ion trapping events and higher currents lead to more trapping of multiple ions at the expense of single ion events. Thus, under optimum single ion conditions, fewer than four ions can be weighed per second using 100 ms trap times and nearly 2/3 of the measurements, which contain no or multiple ions, are discarded.[26,44]

We recently demonstrated multiple trapped ions can be individually weighed in FT-CDMS and that ion-ion interactions with up to 21 ions trapped do not affect the mass measuring accuracy or ion trapping for times up to one second.[43] A key issue, however, is when two or more ions of the same or similar m/z are introduced into the trap and the resulting signals overlap in frequency. This greatly complicates individual ion mass measurement and is most likely for homogenous samples where the number of charge states in a charge state distribution is limited. This problem of ion overlap can be significantly reduced by decoupling the ion frequency from the ion m/z.[43] This decoupling is accomplished by introducing a relatively broad distribution of ion energies per charge (hereafter referred to simply as "ion energies" or "energies") into the ion trap and measuring the energy of each ion *in situ*. A greater than 10-fold gain in speed was demonstrated with multiple single ion measurements using this frequency to m/z decoupling scheme.[43] Here, we explore the limits of multiple ion trapping experiments and how various instrument and analysis parameters affect the potential signal increases in these measurements. These results indicate that this scheme should make possible rapid acquisition of masses of constituent molecules and that this method will be particularly useful for samples that are not amenable to analysis using conventional mass spectrometry measurements.

4.3 Theory

4.3.1 Decoupling Ion Frequency and m/z in CDMS

In conventional mass spectrometry, a single observable is directly coupled to the m/z of an analyte ion. For example, in the most widely used high performance Fourier-transform mass spectrometry instruments, such as Fourier-transform ion cyclotron resonance (FTICR) or Orbitrap instruments, ion m/z is generally determined by calibrating the measured ion frequencies to a m/z scale using reference standards with known mass.[45] While other factors, such as magnetic field strength (FTICR), injection distance from the axial minimum potential (Orbitrap) and trap geometry (both), also affect the observed ion frequencies, they are held constant with a high degree of precision, leaving ion m/z as the sole variable which makes possible direct calibration of ion frequency to ion m/z. In FT-CDMS, where ions are trapped and oscillate with a period frequency, the relationship between ion frequency, f, and m/z, given in equation 4.1:

$$\frac{m}{z} = \frac{C(E)}{f^2} \tag{4.1}$$

C(E) is a function of ion energy, the trapping voltage, and the trap geometry. This value is determined from ion trajectory simulations [39,40].[38,39] Thus, the ion frequency depends on ion energy, through C(E), as well as ion *m*/*z*. In most FT-CDMS trapping experiments to date, C(E) is kept constant with a narrow bandwidth of energies selected by using energy selective ion optics, such as a dual hemispherical deflection analyzer[46] or a turning quadrupole.[29] The narrowest spread of ion energies reported in single ion CDMS is a standard deviation of 0.3% of the nominal energy, which makes possible the charge state resolution of analytes as large as 465 kDa.[42]

The necessity for energy selective ion optics can be eliminated if the ion energy is determined directly from individual ion signals. Because the duty cycle of the time domain ion signal in FT-CDMS depends on the ion energy, the amplitudes of the fundamental and harmonic frequencies also depend on ion energy.[39] Thus, the ratio of the fundamental and second harmonic frequencies can be used to dynamically determine the ion energy throughout the entire trapping period.[39] This measurement of ion energy does not depend on the ion frequency.

Dynamically measuring ion energies makes it possible to take advantage of the ion *m*/*z* and frequency decoupling that occurs as result of non-uniform ion energies in CDMS. Figure 4.1 demonstrates the advantages that can be gained by intentionally decoupling ion *m*/*z* and frequency. The *m*/*z* spectrum of RuBisCO (517 kDa) acquired using a commercial quadrupole time-of-flight mass spectrometer[43] is shown in Figure 4.1a. The most abundant or base peak corresponds to the +51 charge state at *m*/*z* ~10,140. The theoretical frequency line spectrum of the same RuBisCO ions that would be measured in a conventional FT-based instrument or a CDMS spectrum where the ion energy is a singular value, i.e., C(E) in equation 4.1 is a constant, is shown in Figure 4.1b. If a broad range of ion energies are introduced into the trap, the *m*/*z* and frequency are no longer directly coupled. This is illustrated in Figure 4.1c in which an ion with a given *m*/*z* can be observed anywhere within a range of frequencies that is determined by the width of the ion energy distribution.

The decoupling of ion frequency and *m*/*z* is important to increasing the number of ions that can be simultaneously analyzed in a single CDMS trapping event. Because FT-CDMS is based on individual ion frequency and amplitude measurements, two or more ions with interfering frequencies and convolved amplitudes provide no mass information. For example, if two ions with the same *m*/*z* and energy are trapped simultaneously, analogous to the spectrum in Figure 4.1b, their signals would interfere and the mass of neither ion could be readily determined. This is almost certain to occur as the number of trapped ions approaches the number of peaks in the charge-state distribution of a relatively pure sample of a large molecule, significantly limiting the possibility of multiple ion measurements in cases where mass measuring accuracy is on the order of the peak width. By maximizing the frequency range in which ions of a given *m*/*z* can be observed (Figure 4.1c), the probability of interferences is greatly reduced. This makes it possible to introduce and simultaneously measure a greater number of ions in a single trapping event, decreasing the time required to measure a representative mass spectrum. Detection and analysis of simultaneously trapped individual ions has been recently demonstrated in CDMS.[43] Data from ion trapping events containing multiple RuBisCO ions with a moderately broad distribution of ion energies (standard deviation of ~3% of nominal centroid energy) resulted in more than an order of magnitude decrease in data acquisition times over optimal measurements of just single trapped ions.[43]

In other FTMS methods, including FTICR, Orbitrap, and CDMS for ensemble measurements of low charge state ions, ion motion must be coherent in order measure ion mass. Space-charge effects can be observed when the number of charges of trapped ions with similar *m*/*z* exceed a certain value. For example, effects on FTICR frequencies have been measured when ~10000 charges are present in the trap.[45,47] This can result in signal coalescence, a loss of resolution, and other errors.[45,47] Another advantage of single ion CDMS is that ion motion does not have to be coherent in order to measure ion masses. In fact, for optimum multiplexed ion measurements, ion coherence is highly undesirable because coherent ions with the same or nearly the same *m*/*z* and frequency will experience more ion-ion interactions. Incoherent ions interact for only brief periods of time, making it possible to simultaneously trap a greater number of ions without significant space-charge effects. Decoupling ion frequency from *m*/*z* decreases ion coherence as ions with the same *m*/*z* are not constrained to a single oscillation frequency. Incoherence can be also achieved by using ion injection times that are longer than the oscillation period of the lowest velocity ions, effectively randomizing the initial phase of ion oscillation.

4.4 Methods

4.4.1 Simulating CDMS Ion Frequencies

In order to find the maximum possible decrease in data acquisition times using existing CDMS instrumentation,[37] simulations of multiple ion trapping events were performed using a program written in Python (Supporting Information). The effects of many different variables, including the number of ions within a single trapping event, ion charge, charge-state distribution width, ion mass, ion mass distribution width, nominal ion energy, ion energy distribution width, and FT peak width were investigated. For each number of ions within a single trapping event, hereafter referred to as the "ion count", 1,000 trapping events were simulated to insure statistically meaningful results. Each ion in the simulation was assigned with mass, charge, and energy values randomly generated from Gaussian probability distributions where the mean and standard deviation for each property are given as parameters in the simulation. For ion mass and charge, parameters are chosen to match a real analogue as closely as possible. Ion energy distributions are chosen to match instrumental conditions that enable different extents of frequency and *m*/*z* decoupling. The electrostatic cone trap used in previous CDMS experiments can stably trap a relatively broad range of ion energies (±~12% of trap centroid energy).[37,39] However, when very broad ion energy distributions are introduced to the trap, some ions fall outside of this range of stability. Initially generated ion energies outside of the stable trapping range are reevaluated until the energy generated falls within the stable range, yielding a Gaussian distribution of energies that is truncated at low and high energy.

The ion simulation process is shown schematically in Figure 4.2. For the charge state distribution, the randomly generated values are rounded to the nearest integer value, shown in Figure 2 (top) as the black curve and corresponding black stick plot. The ion energies and the additional parameter of the ion trap voltage are then used to calculate the values of C(E) in equation 4.1 for each ion,[39] which, along with the individual ion masses and charges, are used to calculate the frequency of each simulated ion. For each charge state, the distributions of possible frequencies originating from mass (red) and energy (blue) distributions are shown in Figure 4.2 (top). In Figure 4.2, the ranges of possible frequencies due to a broad spread of ion energies cut off abruptly due to trap stability constraints, but are still much larger than those due to the narrow spread of ion

masses. This result is typical of the relatively homogeneous samples that are often analyzed with native mass spectrometry. After the frequencies are calculated for ions within a single trapping event, the final step of the simulation evaluates overlap between ion frequencies. In a real CDMS trapping event, if the frequencies of two or more ions are closer than the characteristic FT peak width, they interfere with each other, making it difficult to properly measure the exact frequency and charge of the ions. Thus, in these simulations, ions in the same trapping event that have frequencies closer than the FT peak width are discarded. Figure 4.2 (bottom) shows an example of simulated trapping event where the ion count is 10 and two ions with overlapping frequencies near the center of the overall distribution are discarded. Such overlapping ion signals in CDMS measurements are readily identified owing to minor differences in ion frequency evolution with time.[43] Simulated ions that survive this culling criterion could be accurately measured in a real CDMS experiment. The surviving ions from all trapping events at each ion count are summed and divided by the number of trapping events to yield the average number of usable ions at each ion count. To determine the overall gain in ion throughput relative to single ion-only CDMS analysis, the average number of usable ions is divided by 0.37, corresponding to the maximum percentage of ion events that are usable when data from only single ion trapping events are used.[26,44]

As the only simulated parameter that is completely determined by the data analysis method used, the characteristic FT peak width corresponding to the length of time domain segment used is a vital parameter in determining the maximum gain in CDMS acquisition rates. Narrower peak widths enable more unique ion frequencies to "fit" in a single trapping event without overlap within the frequency space established by the ion mass, charge, and energy distributions, resulting in faster overall ion acquisition. In Figure 4.3, the ideal relationship between FT length and peak base width for unapodized signal with a constant frequency is shown in red. Apodization of FT signals results in broader FT peaks regardless of the apodization function and is therefore undesirable in the context of multiple ion analysis in CDMS. For example, the commonly used Hanning apodization doubles the peak base width for a given FT length, as shown in grey in Figure 4.3. For model ion signals that do not vary in frequency over time, an FT of the entire trapping period results in the narrowest possible peaks, as peak widths vary as the inverse of FT length. However, multiple studies have shown that ion frequencies in CDMS do not remain constant for the duration of the trapping period.[37–39,43,48,49] Collisions with background gas, neutral mass losses, and fragmentation all effect CDMS oscillation frequencies. If the ion signal frequency changes over the length of the FT, the peak width is broadened leading to signal amplitude that is distributed over multiple frequencies. This reduces the signal peak amplitude, resulting in a lower measured value of ion charge. As a result, short-time Fourier transforms (STFT) have been implemented to overcome this effect by transforming short segments in which the change in ion frequency is negligible.[33,38] The amplitude data from each short segment is then averaged to calculate the charge, yielding the same precision typically obtained by using a single long FT on stationary signals.

For multi-ion CDMS, the best choice of STFT segment length is the longest period that does not result in broadened peak widths and lowered amplitudes. This can be determined by analyzing the peak widths of the analyte of interest as function of FT length. For example, Figure 4.3 shows the average base peak widths for the experimental data of 125 RuBisCO ions analyzed with different FT lengths incremented by 5 ms (black points). The RuBisCO peak width data begin to diverge from the ideal width (red) between ~40-50 ms, due to frequency shifting as a consequence of energy lost to collisions with background gas. This divergence is more apparent in the percentage

of deviation from the ideal width (blue points, secondary axis in Figure 4.3). The FT length at which widths diverge from the ideal can vary significantly depending on instrumental conditions, such as the pressure in the trapping region and the trap design. Traps in which ion motion is more harmonic will lead to lower energy dependence on the oscillation frequency.[42] In this work, a virtual FT segment length of 50 ms corresponding to a 40 Hz base peak width was used in all simulations to make the results readily comparable to previous work. However, using this method to determine the ideal FT segment length in a multi-ion CDMS experiment is an important step in optimizing usable ion throughput.

4.5 Results and Discussion

4.5.1 Maximum Gains in Analysis Speed for Different Analytes

Using the simulation scheme described above, the optimum ion count and the gain in overall ion acquisition speed was determined for two analytes under different instrumental conditions. Analyte **A** has a nominal mass of 8 MDa and very broad mass and charge distributions, analogous to a sample of 8 MDa polyethylene glycol (PEG) studied in other CDMS work.[29] Analyte **B** has a nominal mass of 517 kDa and relatively narrow mass and charge distributions, analogous to the sample of RuBisCO in Figure 4.1a.[43] All of these analyte specific parameters used in the simulations are provided in Table 4.1. Both analytes were simulated using three different sets of ion energy parameters, corresponding to different instrumental conditions. A narrow energy distribution (0.3% standard deviation), where frequency and *m*/*z* are closely coupled, corresponds to previous CDMS work where energy selective ion optics were employed.[42] An intermediate energy distribution (3% standard deviation), where there is significant decoupling, corresponds to recent multi-ion CDMS work.[43] Finally, a very broad energy distribution width (7.3% standard deviation) was simulated. This width was chosen such that ions within 1.5 standard deviations (~90% of all ions) would fall within the stability constraints imposed by current instrumentation.[37] The trap voltage is set to its current maximum of 500 V so that the absolute width of stable ion energies is as large as possible.[39] All parameters for these simulated energy distributions are provided in Table 2. Instrumentation capable of higher trap voltages and higher energy ion confinement could increase the absolute width of usable ion energies even further. Other decoupling gains might also be made via an improved trap design that stably confines ions with a wider energy distribution. However, these improvements were not studied here due to the trap design-specific parameters required to calculate ion energies and C(E) in equation 4.1.[37–39]

Decoupling the frequency and *m*/*z* in CDMS greatly increases the number of ions which can be simultaneously analyzed, particularly for homogeneous samples. The gain in ion analysis speed as a function of the ion count is shown in Figure 4.4. For analyte **A** (circles), the gain in analysis speed is nearly linear with ion count for each different energy distribution. This is because the extremely broad mass and charge-state distributions of **A** result in a very broad range of possible frequencies regardless of the ion energy distribution and ion overlap events are rare even at higher ion counts. While greater decoupling does not yield large relative gains in ion throughput in this case, these results suggest that very large gains are possible for heterogeneous samples by measuring many ions using CDMS. Further simulations of **A** at ion counts up to 100 result in ion throughput gains of up to ~160x. This is lower than the ideal value of 270x because even for a very heterogeneous sample, the frequency space is still finite so the probability of overlap becomes more significant with a large number of trapped ions. In these cases, gains in usable signal can

still be obtained by using the energy decoupling scheme. Ions produced from samples like **A** will be highly charged so it is possible that ion-ion interactions will ultimately limit the number of ions that can be simultaneously analyzed in an actual CDMS experiment. The extent to which ion-ion interactions are limiting can be determined from experimental measurements of ion mass as a function of the number of ions trapped[39] or potentially from ion trajectory simulations.

In the case of relatively homogeneous samples, such as analyte **B** (squares), ion frequency and *m*/*z* decoupling has a much more significant effect on the ion throughput gains, as shown in Figure 4.4. The three plots corresponding to the narrow (blue), intermediate (black), and broad (red) energy distributions of analyte **B** all have the same characteristic shape. The initial linear increase in gain is due to the low probability of ion overlap at low ion counts. The plots then level off as overlap events become more probable, eventually reaching a maximum. The maximum represents the ion count at which an ion added to the trapping event has equal probabilities of overlapping or not overlapping with another ion. After reaching the maximum, the slow decline in gain occurs as the high probability of ion overlap results in fewer usable ions. The maximum gain in analysis speed and corresponding ion count vary significantly depending on the extent of decoupling. Analyte **B** ions with a narrow distribution of ion energies (blue) reaches a maximum gain of ~19x at an ion count of ~20, whereas **B** ions with the broadest energy distribution (red) reaches a maximum gain of ~48x at an ion count of ~45, meaning that decoupling has the potential to more than double the overall analysis speed for analyte **B** ions using optimum ion currents. In both cases, the maximum gain in analysis speed is significantly higher than the ~10x improvement demonstrated in previous multi-ion CDMS work[43] because the average ion count/current was lower than the optimum value. To further corroborate this conclusion, the results from the intermediate energy distribution (black) match well with experimental results under closely comparable conditions. When an average of ~6 RuBisCO ions were trapped, there was a frequency overlap rate of ~15%;[43] for an ion count of 6 in this simulation, 1093 out of 6000 ions (18.2%) were discarded as a result of overlap. This close correlation between our simulations and previous experimental results suggests that these simulations serve as reasonably accurate predictors of CDMS data strengthening our conclusions that further gains in CDMS ion analysis speed through ion multiplexing and decoupling frequency from *m*/*z* are possible. Another important conclusion from these data is that while the absolute gains in analysis speed depend on the ion count and analyte identity, it is always advantageous to maximize the extent of decoupling to obtain more usable ion signal. Ion-ion effects are not included in these simulations and these interactions may ultimately limit the extent of multiplexing that is experimentally achievable.

4.5.2 Improved Quantitation and Dynamic Range via Decoupling

In addition to gains in analysis speed, decoupling ion frequency and *m*/*z* in CDMS can also yield greater dynamic range and provide more accurate quantitation in experiments where multiple ions are trapped. This is illustrated in Figure 4.5, where the simulated frequency histograms for 1000 trapping events for analyte **B** are shown at narrow, intermediate, and maximized ion energy distribution widths (rows) for ion counts of 1, 10, and 25 (columns). For an ion count of 1 (left column), the narrow ion energy distribution (top row) produces a resolved charge-state distribution in the frequency histogram where the abundance of each charge state is accurately reproduced. However, as the ion count increases to 10 (center column), the number of ions making up each peak in the charge-state distribution no longer accurately reflect the true values. Ions within the most abundant charge states are more likely to overlap in frequency and be discarded, resulting in

a histogram skewed towards low abundance ions. This effect becomes very apparent at an ion count of 25 (right column). Resolution also decreases as a function of ion count. Outlier ions with frequencies that fall in between charge states are less likely to experience overlap and are retained disproportionally. For the intermediate ion energy distribution (middle row), the skew towards outliers is significantly decreased and is only visible as a small dip in the histogram for an ion count of 25. The charge state resolution in the frequency histogram is lost, but because the *m*/*z* of each ion is obtained from both the frequency and ion energy measurements, the charge state distribution in *m*/*z* space is resolved. For the broadest ion energy distribution (bottom row), the skew towards outliers is almost entirely mitigated at all ion counts. The irregular shape of the frequency distributions for the broadest energy distribution is due to a limited range of ion energies that can be trapped and a non-linear relationship between ion energy and frequency. The frequency is higher because the mean ion energy and corresponding trap voltage in the simulation are higher. While the charge-state distributions cannot be resolved in the frequency histogram for broader energy distributions, the *m*/*z* histograms generated from these frequency data still contain resolved charge state distributions. Thus, no mass information is lost as a result of this frequency decoupling method as long as the energy and charge of each ion is measured individually, as demonstrated elsewhere.[37,39,43]

While the skewing effect observed in the narrow and intermediate energy distributions of Figure 4.5 does not affect the mass measurement of individual ions, it can affect the accuracy of quantitation and dynamic range of a sample containing two or more analytes. For example, if the abundance ratio of two analytes contained in a sample is 25:1, a trapping event with an ion count of 26 will contain, on average, 25 ions of the more abundant species and only one ion of the low abundance species. Using the narrow energy distribution described above, an ion count of 25 for the high abundance component results in ~6.8 usable ions after overlapping ions are discarded. If the low abundance ion occupies a different *m*/*z* and frequency space than that of the high abundance ion, it will very rarely experience overlap due to its low ion count. This results in an apparent abundance ratio of 6.8:1, nearly 4x lower than the true value. Decoupling ion *m*/*z* and frequency via a broader energy distribution can help mitigate this effect. For the same 25:1 true abundance ratio, the broadest energy distribution described above yields an apparent ratio of 14.7:1, 58.9% of the true value. In both cases, the high abundance component is under sampled because only multi-ion events with zero overlap will provide exact quantitation.

In multi-ion CDMS experiments, a more accurate measure of the true abundance ratios can be obtained by selecting trapping events that have the lowest number (ideally zero) of overlap events to use in the abundance calculation. Using lower than the optimum multiplexing ion current may also help to mitigate this effect in exchange for relatively small losses in analysis speed, i.e., using lower ion counts in the region where changes in the gain of analysis speed are minimal (Figure 4.4). Regardless of the methods used, abundances measured using a broad energy distribution will have significantly reduced quantitation error due to the significantly lower probability of overlap at all ion counts. This advantage, in addition to the larger gains in analysis speed, make the maximum decoupling of ion frequency and *m*/*z* highly advantageous for multi-ion CDMS.

4.6 Conclusions

Simulations of ion signals for existing CDMS instrumentation demonstrate that the time necessary to acquire single ion CDMS mass histograms can be greatly reduced by analyzing many

simultaneously trapped ions. This gain in analysis speed can be increased further by decoupling ion *m*/*z* from the measured ion frequency. Decoupling is achieved by introducing ions with a broad range of energies into the CDMS ion trap. No mass information is lost as a result of decoupling because ion energies are measured dynamically for each individual ion. Compared to prior CDMS experiments where only trapping events containing a single ion were analyzed[26] these simulations show that up to a ~48x increase in analysis speed is achievable for homogeneous samples of large molecules such as large protein complexes, viruses, and other biological macromolecules that CDMS is well-suited to analyze. Using only trapping events containing a single ion, CDMS experiments using 100 ms trapping events and optimum ion currents require ~30-60 mins to measure a usable mass histogram for a relatively homogeneous analyte.[42,44] Using the methods described here, the acquisition time of a similar histogram can potentially be reduced to less than one minute. For heterogeneous samples of large molecules such as polymers, analysis speed increases of up to ~160x are predicted, although actual experimental gains may be limited by ion-ion interactions inside of the trap.

CDMS has a nearly unlimited mass range, does not require homogeneous samples, and dynamic measurements that can also provide information about collisional cross sections[38,39] and fragmentation pathways[37,50] of individual ions. This makes CDMS an ideal choice for the native MS analysis of large, biologically relevant macromolecules and heterogeneous mixtures of large molecules that are too large or too heterogeneous to be analyzed with conventional mass spectrometers. Continued advances in CDMS technology have increased the sensitivity and accuracy of the method to the point where the intrinsic heterogeneity in the mass of large molecules of interest is nearly equal to or exceeds the experimental error in mass determination.[26,42,43] Similar to other single ion measurements, such as those performed using FTICR[13] and Orbitrap[16] instruments, a principal limitation in CDMS has been the time required to acquire a statistically meaningful set of individual ion data. Using multi-ion CDMS, this throughput limitation has largely been surmounted and further gains in acquisition speed seem reasonably attainable with improvements in instrument design.

4.7 Acknowledgements

This material is based upon work supported by the National Science Foundation under CHE-1609866.

4.8 References

(1) Susa, A. C.; Xia, Z.; Williams, E. R. Native Mass Spectrometry from Common Buffers with Salts That Mimic the Extracellular Environment. *Angew. Chemie - Int. Ed.* **2017**, *56* (27), 7912–7915.

(2) Gavriilidou, A. F. M.; Gülbakan, B.; Zenobi, R. Influence of Ammonium Acetate Concentration on Receptor-Ligand Binding Affinities Measured by Native Nano ESI-MS: A Systematic Study. *Anal. Chem.* **2015**, *87* (20), 10378–10384.

(3) Loo, J. A. Electrospray Ionization Mass Spectrometry: A Technology for Studying Noncovalent Macromolecular Complexes. *Int. J. Mass Spectrom.* **2000**, *200* (1–3), 175–186.

(4) Wysocki, V. H.; Jones, C. M.; Galhena, A. S.; Blackwell, A. E. Surface-Induced Dissociation Shows Potential to Be More Informative Than Collision-Induced Dissociation for Structural Studies of Large Systems. *Journal of the American Society for Mass Spectrometry*. Elsevier Inc. November 22, 2008, pp 903–913.

(5) Benesch, J. L. P.; Aquilina, J. A.; Ruotolo, B. T.; Sobott, F.; Robinson, C. V. Tandem Mass Spectrometry Reveals the Quaternary Organization of Macromolecular Assemblies. *Chem. Biol.* **2006**, *13* (6), 597–605.

(6) Lössl, P.; Snijder, J.; Heck, A. J. R. Boundaries of Mass Resolution in Native Mass Spectrometry. *J. Am. Soc. Mass Spectrom.* **2014**, *25* (6), 906–917.

(7) O'Connor, P. B.; McLafferty, F. W. Oligomer Characterization of 4—23 KDa Polymers by Electrospray Fourier Transform Mass Spectrometry. *J. Am. Chem. Soc.* **1995**, *117* (51), 12826–12831.

(8) Robb, D. B.; Brown, J. M.; Morris, M.; Blades, M. W. Method of Atmospheric Pressure Charge Stripping for Electrospray Ionization Mass Spectrometry and Its Application for the Analysis of Large Poly(Ethylene Glycol)S. *Anal. Chem.* **2014**, *86* (19), 9644–9652.

(9) McKay, A. R.; Ruotolo, B. T.; Ilag, L. L.; Robinson, C. V. Mass Measurements of Increased Accuracy Resolve Heterogeneous Populations of Intact Ribosomes. *J. Am. Chem. Soc.* **2006**, *128* (35), 11433–11442.

(10) Morgner, N.; Robinson, C. V. Mass Ign: An Assignment Strategy for Maximizing Information from the Mass Spectra of Heterogeneous Protein Assemblies. *Anal. Chem.* **2012**, *84* (6), 2939–2948.

(11) Sader, J. E.; Hanay, M. S.; Neumann, A. P.; Roukes, M. L. Mass Spectrometry Using Nanomechanical Systems: Beyond the Point-Mass Approximation. *Nano Lett.* **2018**, *18* (3), 1608–1614.

(12) Hanay, M. S.; Kelber, S.; Naik, A. K.; Chi, D.; Hentz, S.; Bullard, E. C.; Colinet, E.; Duraffourg, L.; Roukes, M. L. Single-Protein Nanomechanical Mass Spectrometry in Real Time. *Nat. Nanotechnol.* **2012**, *7* (9), 602–608.

(13) Smith, R. D.; Cheng, X.; Brace, J. E.; Hofstadler, S. A.; Anderson, G. A. Trapping, Detection and Reaction of Very Large Single Molecular Ions by Mass Spectrometry. *Nature* **1994**, *369* (6476), 137–139.

(14) Bruce, J. E.; Cheng, X.; Bakhtiar, R.; Wu, Q.; Hofstadler, S. A.; Anderson, G. A.; Smith, R. D. Trapping, Detection, and Mass Measurement of Individual Ions in a Fourier Transform Ion Cyclotron Resonance Mass Spectrometer. *J. Am. Chem. Soc.* **1994**, *116* (17), 7839–7847.

(15) Makarov, A.; Denisov, E. Dynamics of Ions of Intact Proteins in the Orbitrap Mass Analyzer. *J. Am. Soc. Mass Spectrom.* **2009**, *20* (8), 1486–1495.

(16) Kafader, J. O.; Melani, R. D.; Senko, M. W.; Makarov, A. A.; Kelleher, N. L.; Compton, P. D. Measurement of Individual Ions Sharply Increases the Resolution of Orbitrap Mass Spectra of Proteins. *Anal. Chem.* **2019**, *91* (4), 2776–2783.

(17) Wuerker, R. F.; Shelton, H.; Langmuir, R. V. Electrodynamic Containment of Charged Particles. *J. Appl. Phys.* **1959**, *30* (3), 342–349.

(18) Philip, M. A.; Gelbard, F.; Arnold, S. An Absolute Method for Aerosol Particle Mass and Charge Measurement. *J. Colloid Interface Sci.* **1983**, *91* (2), 507–515.

(19) Hars, G.; Tass, Z. Application of Quadrupole Ion Trap for the Accurate Mass Determination of Submicron Size Charged Particles. *J. Appl. Phys.* **1995**, *77* (9), 4245–4250.

(20) Schlemmer, S.; Illemann, J.; Wellert, S.; Gerlich, D. Nondestructive High-Resolution and Absolute Mass Determination of Single Charged Particles in a Three-Dimensional Quadrupole Trap. *J. Appl. Phys.* **2001**, *90* (10), 5410–5418.

(21) Howder, C. R.; Bell, D. M.; Anderson, S. L. Optically Detected, Single Nanoparticle Mass Spectrometer with Pre-Filtered Electrospray Nanoparticle Source. *Rev. Sci. Instrum.* **2014**, *85* (1), 014104.

(22) Twerenbold, D. Biopolymer Mass Spectrometer with Cryogenic Particle Detectors. *Nucl. Instruments Methods Phys. Res. Sect. A Accel. Spectrometers, Detect. Assoc. Equip.* **1996**, *370* (1), 253–255.

(23) Sipe, D. M.; Plath, L. D.; Aksenov, A. A.; Feldman, J. S.; Bier, M. E. Characterization of Mega-Dalton-Sized Nanoparticles by Superconducting Tunnel Junction Cryodetection Mass Spectrometry. *ACS Nano* **2018**, *12* (3), 2591–2602.

(24) Barney, B. L.; Pratt, S. N.; Austin, D. E. Survivability of Bare, Individual Bacillus Subtilis Spores to High-Velocity Surface Impact: Implications for Microbial Transfer through Space. *Planet. Space Sci.* **2016**, *125*, 20–26.

(25) Benner, W. H. A Gated Electrostatic Ion Trap to Repetitiously Measure the Charge and m/z of Large Electrospray Ions. *Anal. Chem.* **1997**, *69* (20), 4162–4168.

(26) Keifer, D. Z.; Pierson, E. E.; Jarrold, M. F. Charge Detection Mass Spectrometry: Weighing Heavier Things. *Analyst* **2017**, *142* (10), 1654–1671.

(27) Keifer, D. Z.; Jarrold, M. F. Single-Molecule Mass Spectrometry. *Mass Spectrom. Rev.* **2017**, *36* (6), 715–733.

(28) Doussineau, T.; Bao, C. Y.; Antoine, R.; Dugourd, P.; Zhang, W.; D'Agosto, F.; Charleux, B. Direct Molar Mass Determination of Self-Assembled Amphiphilic Block Copolymer Nanoobjects Using Electrospray-Charge Detection Mass Spectrometry. *ACS Macro Lett.* **2012**, *1* (3), 414–417.

(29) Elliott, A. G.; Merenbloom, S. I.; Chakrabarty, S.; Williams, E. R. Single Particle Analyzer of Mass: A Charge Detection Mass Spectrometer with a Multi-Detector Electrostatic Ion Trap. *Int. J. Mass Spectrom.* **2017**, *414*, 45–55.

(30) Adamson, B. D.; Miller, M. E. C.; Continetti, R. E. The Aerosol Impact Spectrometer: A Versatile Platform for Studying the Velocity Dependence of Nanoparticle-Surface Impact Phenomena. *EPJ Tech. Instrum.* **2017**, *4* (1), 1–17.

(31) Lutomski, C. A.; Lyktey, N. A.; Pierson, E. E.; Zhao, Z.; Zlotnick, A.; Jarrold, M. F.

Multiple Pathways in Capsid Assembly. *J. Am. Chem. Soc.* **2018**, *140* (17), 5784–5790.

(32) Lutomski, C. A.; Gordon, S. M.; Remaley, A. T.; Jarrold, M. F. Resolution of Lipoprotein Subclasses by Charge Detection Mass Spectrometry. *Anal. Chem.* **2018**, *90* (11), 6353–6356.

(33) Pierson, E. E.; Contino, N. C.; Keifer, D. Z.; Jarrold, M. F. Charge Detection Mass Spectrometry for Single Ions with an Uncertainty in the Charge Measurement of 0.65 E. *J. Am. Soc. Mass Spectrom.* **2015**, *26* (7), 1213–1220.

(34) Pierson, E. E.; Keifer, D. Z.; Asokan, A.; Jarrold, M. F. Resolving Adeno-Associated Viral Particle Diversity with Charge Detection Mass Spectrometry. *Anal. Chem.* **2016**, *88* (13), 6718–6725.

(35) Keifer, D. Z.; Pierson, E. E.; Hogan, J. A.; Bedwell, G. J.; Prevelige, P. E.; Jarrold, M. F. Charge Detection Mass Spectrometry of Bacteriophage P22 Procapsid Distributions above 20 MDa. *Rapid Commun. Mass Spectrom.* **2014**, *28* (5), 483–488.

(36) Pierson, E. E.; Keifer, D. Z.; Contino, N. C.; Jarrold, M. F. Probing Higher Order Multimers of Pyruvate Kinase with Charge Detection Mass Spectrometry. *Int. J. Mass Spectrom.* **2013**, *337*, 50–56.

(37) Elliott, A. G.; Harper, C. C.; Lin, H. W.; Williams, E. R. Mass, Mobility and MSN Measurements of Single Ions Using Charge Detection Mass Spectrometry. *Analyst* **2017**, *142* (15), 2760–2769.

(38) Elliott, A. G.; Harper, C. C.; Lin, H. W.; Susa, A. C.; Xia, Z.; Williams, E. R. Simultaneous Measurements of Mass and Collisional Cross-Section of Single Ions with Charge Detection Mass Spectrometry. *Anal. Chem.* **2017**, *89* (14), 7701–7708.

(39) Harper, C. C.; Elliott, A. G.; Lin, H. W.; Williams, E. R. Determining Energies and Cross Sections of Individual Ions Using Higher-Order Harmonics in Fourier Transform Charge Detection Mass Spectrometry (FT-CDMS). *J. Am. Soc. Mass Spectrom.* **2018**, *29* (9), 1861–1869.

(40) Keifer, D. Z.; Motwani, T.; Teschke, C. M.; Jarrold, M. F. Acquiring Structural Information on Virus Particles with Charge Detection Mass Spectrometry. *J. Am. Soc. Mass Spectrom.* **2016**, *27* (6), 1028–1036.

(41) Keifer, D. Z.; Shinholt, D. L.; Jarrold, M. F. Charge Detection Mass Spectrometry with Almost Perfect Charge Accuracy. *Anal. Chem.* **2015**, *87* (20), 10330–10337.

(42) Hogan, J. A.; Jarrold, M. F. Optimized Electrostatic Linear Ion Trap for Charge Detection Mass Spectrometry. *J. Am. Soc. Mass Spectrom.* **2018**, *29* (10), 2086–2095.

(43) Harper, C. C.; Elliott, A. G.; Oltrogge, L. M.; Savage, D. F.; Williams, E. R. Multiplexed Charge Detection Mass Spectrometry for High-Throughput Single Ion Analysis of Large Molecules. *Anal. Chem.* **2019**, *91* (11), 7458–7468.

(44) Draper, B. E.; Jarrold, M. F. Real-Time Analysis and Signal Optimization for Charge Detection Mass Spectrometry. *J. Am. Soc. Mass Spectrom.* **2019**, *30* (6), 898–904.

(45) Marshall, A. G.; Hendrickson, C. L.; Jackson, G. S. Fourier Transform Ion Cyclotron Resonance Mass Spectrometry: A Primer. *Mass Spectrom. Rev.* **1998**, *17* (1), 1–35.

(46) Contino, N. C.; Jarrold, M. F. Charge Detection Mass Spectrometry for Single Ions with a Limit of Detection of 30 Charges. *Int. J. Mass Spectrom.* **2013**, *345–347*, 153–159.

(47) Ledford, E. B.; Rempel, D. L.; Gross, M. L. Space Charge Effects in Fourier Transform Mass Spectrometry. Mass Calibration. *Anal. Chem.* **1984**, *56* (14), 2744–2748.

(48) Keifer, D. Z.; Alexander, A. W.; Jarrold, M. F. Spontaneous Mass and Charge Losses from Single Multi-Megadalton Ions Studied by Charge Detection Mass Spectrometry. *J. Am. Soc. Mass Spectrom.* **2017**, *28* (3), 498–506.

(49) Elliott, A. G.; Harper, C. C.; Lin, H. W.; Williams, E. R. Effects of Individual Ion Energies on Charge Measurements in Fourier Transform Charge Detection Mass Spectrometry (FT-CDMS). *J. Am. Soc. Mass Spectrom.* **2019**, *30* (6), 946–955.

(50) Halim, M. A.; Clavier, C.; Dagany, X.; Kerleroux, M.; Dugourd, P.; Dunbar, R. C.; Antoine, R. Infrared Laser Dissociation of Single Megadalton Polymer Ions in a Gated Electrostatic Ion Trap: The Added Value of Statistical Analysis of Individual Events. *Phys. Chem. Chem. Phys.* **2018**, *20* (17), 11959–11966.

4.9 Tables and Figures

Table 4.1. Simulated Ion Parameters for Analytes A[43] and B[29]

Parameter	Analyte A	Analyte B
Mass (Da)	517000	8000000
Mass Standard Deviation (Da)	1551	2000000
Charge (e)	51	800
Charge Standard Deviation (e)	1.8	100

Table 4.2. Parameters for Simulated Ion Energy Distributions

Energy Distribution	Mean Energy per Charge (eV/z)	Energy per Charge Standard Deviation (eV/z)	Trapping Voltage (V)	Stable Trapping Range (eV/z)
Narrow	230	0.7	330	195-245
Intermediate	230	7	330	195-245
Broad	342.5	25	500	305-380

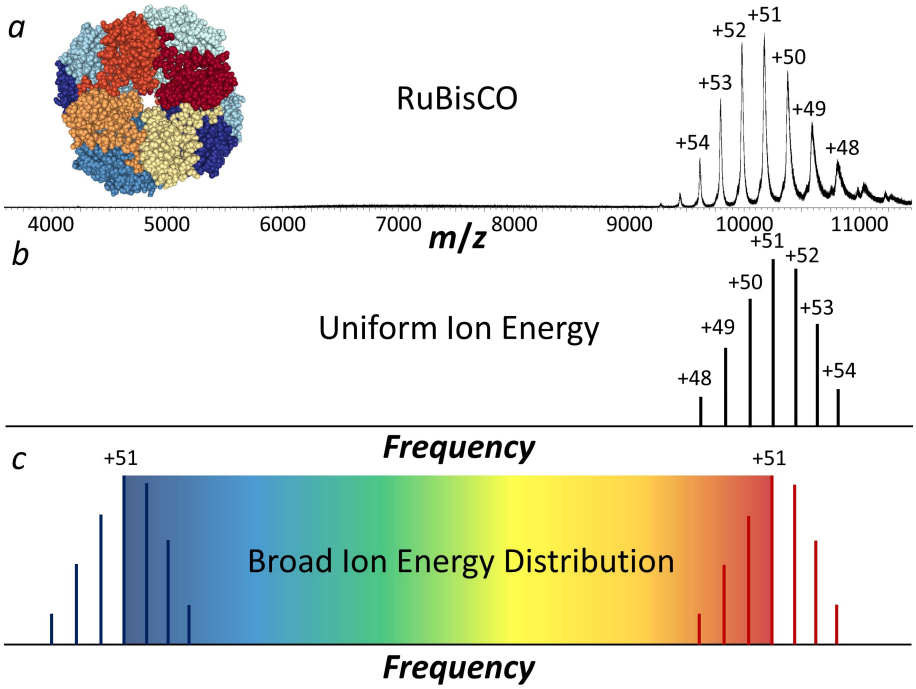


Figure 4.1. Illustration of decoupling ion *m*/*z* from ion frequency. The *m*/*z* spectrum of RuBisCO (517 kDa, with structure PDB ID: 8RUC shown in the left corner) obtained using a commercial Q-TOF instrument (*a*) has a limited number of peaks in the charge state distribution. An equivalent theoretical frequency domain spectrum that might be measured using a conventional FT-based instrument or a CDMS instrument where the range of ion energies is narrow is shown in (*b*). By introducing a broad range of ion energies into a CDMS instrument, *m*/*z* and frequency are decoupled. Thus, ions that have the same *m*/*z* can appear at different frequencies, as shown in (*c*). If multiple ions are trapped, the probability of ion interference in (*b*) is high, but low in (*c*).

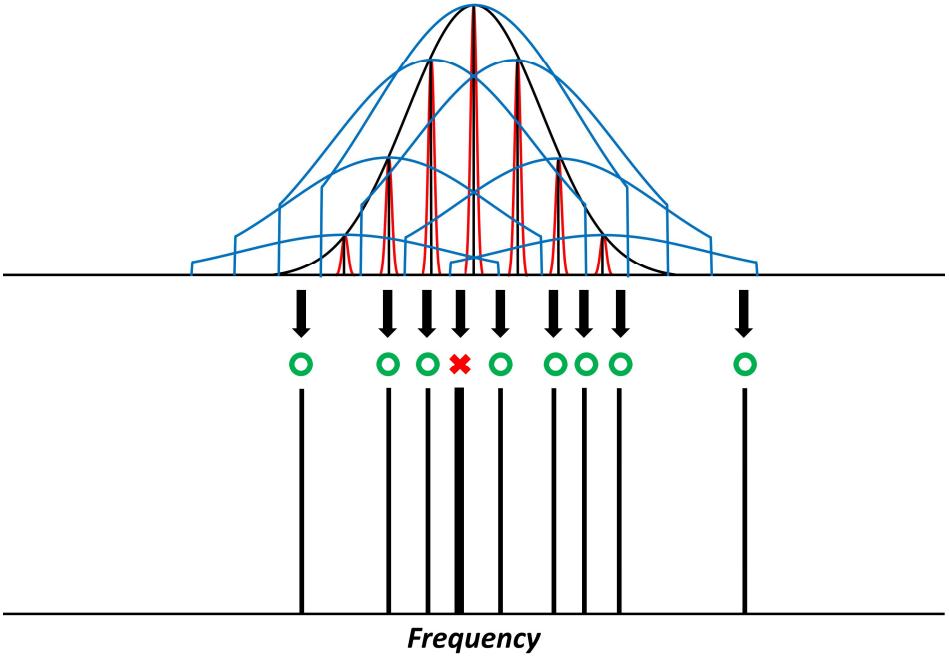


Figure 4.2. Scheme of the ion frequency simulation of a trapping event with an ion count of 10. Gaussian-weighted, randomly generated values for the ion charge (represented by the black distribution, rounded to the nearest integer), ion mass (red), and ion energy (blue, truncated due to instrumentation constraints) values all affect the ion frequency. Broader distributions, such as ion energy (blue) in this scheme, affect the range of ion frequencies more than parameters that are narrowly distributed, such as mass (red). If any of the generated ion frequencies overlap (bottom plot, red X), they are discarded from the simulation.

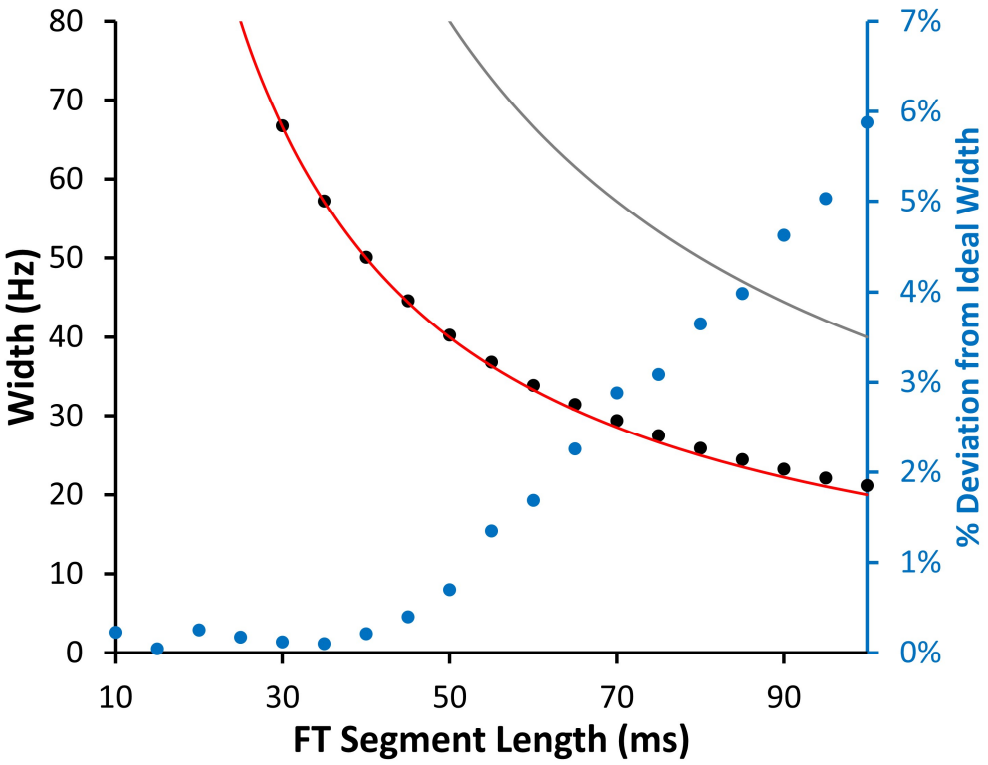


Figure 4.3. Effects of FT segment length and on ion frequency peak widths for experimentally measured RuBisCO ion signal. Ideal non-apodized (red) and Hanning-apodized (grey) peak widths are compared with the average measured width for 125, non-apodized experimental signals of RuBisCO ions (black) at different FT segment lengths. The RuBisCO data begin to slightly diverge from the ideal non-apodized signal around 40-50 ms owing to a gradual shift in frequency with time that occurs as a result of collisional energy loss and other factors. This divergence is more clearly observed in a plot of the % deviation from the ideal value, pictured here on a secondary axis (blue).

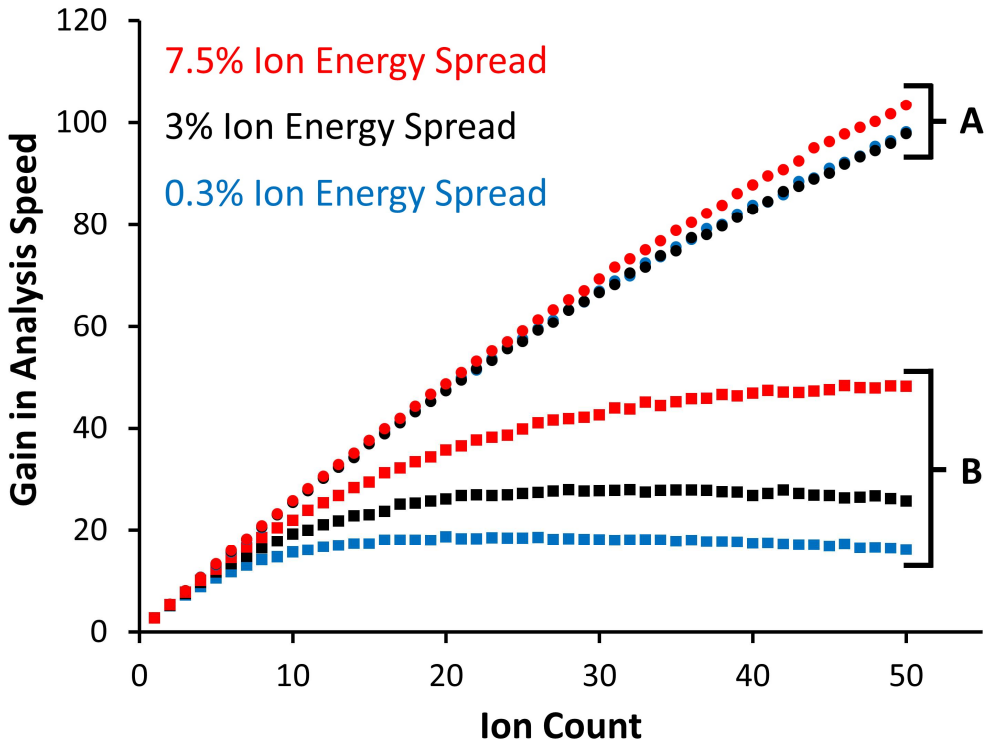


Figure 4.4. Simulated gains in analysis speed for analytes **A** and **B**. For analyte **A**, the ion energy distribution width makes only a minor difference in the observed gain. For analyte **B**, increasing the ion energy spread results in significantly higher gains in analysis speed.

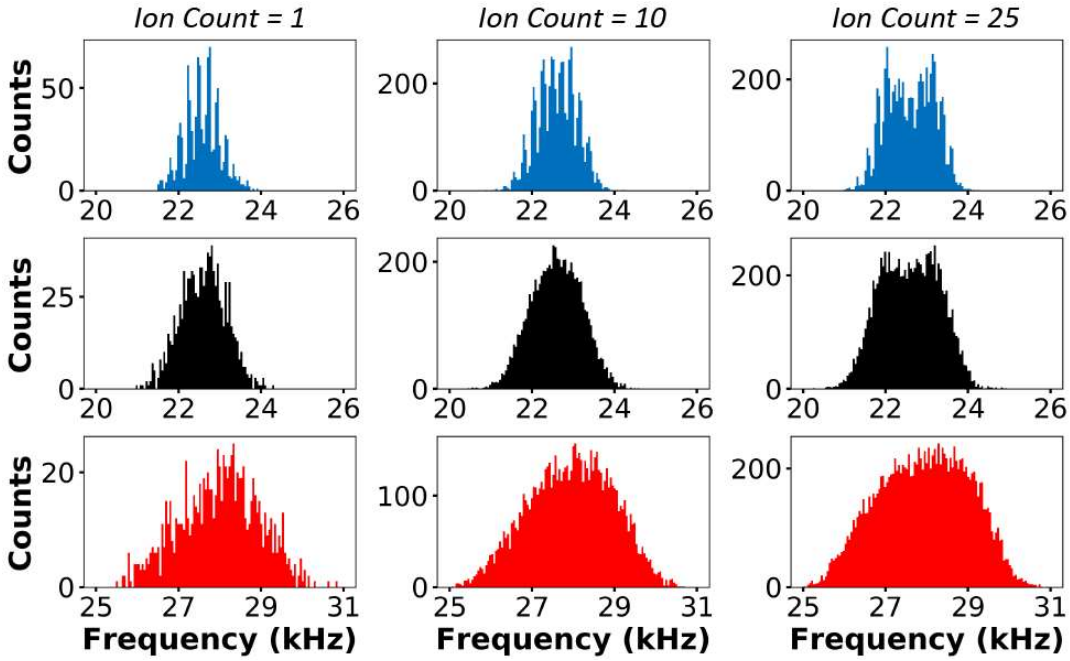


Figure 4.5. Simulated frequency histograms with different ion counts (1, 10, and 25) and different ion energy distribution widths (standard deviations of 0.3%, 3%, and 7.5%, rows, top to bottom). At low ion count, the narrowest energy distribution yields a charge state resolved, quantitative histogram. As ion count increases, quantitation is lost, as the most probable ions are suppressed by frequent overlap events. This quantitation error is mitigated in the lower histograms because overlap is less likely when the ion energy distributions are broad.

4.9 Supporting Information

4.9.1 Python Code and Parameters for CDMS Mass Histogram Simulation

```
####### # Simulating a CDMS Mass histogram # #######
import numpy as np
import numpy.random as rand
import matplotlib.pyplot as plt
import math
import time
import csv
import tkinter as tk
from tkinter import filedialog as fd

#file dialog for directory to save data files
root = tk.Tk()
folder = fd.askdirectory(title = "Choose save location")
root.withdraw()
root.focus_force()

#Energy (eV/z) to C-value conversion (m/z = C(E)/f**2)
#C(E) function of both trap_V and eV_mean (but not their ratio)
#Equation--- C(E) =
(A00+A10*eV_mean+A01*Trap_V+A20*eV_mean**2+A11*eV_mean*Trap_V+A02*Trap_V
**2+A30*eV_mean**3+
#A21*eV_mean**2*Trap_V+A12*eV_mean*Trap_V**2+A03*Trap_V**3)**2

a00=602227.4507
a10=-11874.09336
a01=15785.48334
a20=-110.6314816
a11=179.8976398
a02=-80.62300667
a30=-0.072958226
a21=0.325082528
a12=-0.369837273
a03=0.130371575

trap_V = 500

#Ion Parameters
eV_mean = 342.5
eV_sigma = 25

lowerE = 305
higherE = 380
```

```
mass_center = 517000
mass_sigma = mass_center*0.03

z_mean = 51
z_sigma = 1.8

max_ions =50
trap_events=1000

width = 40

totals =[]

counted_simgoodspectrum = []

for ioncount in np.arange(1,max_ions+1,1): #zip ax in axs to get figures
   r_events=[]
   for event in np.arange(0,trap_events,1):
      r_ions=[]
      for ion in np.arange(0,ioncount,1):
         m = rand.normal(loc=mass_center,scale=mass_sigma)
         z = int(rand.normal(loc=z_mean, scale=z_sigma))
         E = rand.normal(loc=eV_mean,scale=eV_sigma)
         while E < lowerE or E > higherE:
            E = rand.normal(loc=eV_mean,scale=eV_sigma)

         m_z = m/z
         C_eV =
(a00+a10*E+a01*trap_V+a20*E**2+a11*E*trap_V+a02*trap_V**2+a30*E**3+a21*E**2*tra
p_V+a12*E*trap_V**2+a03*trap_V**3)**2
         r_freq = (z*C_eV/m)**0.5
         r_ions.append(r_freq)

      r_events.append(r_ions)

   goodioncount =[]
   goodionspectrum =[]
   goodionfreqtable = []
   goodionscount_wshift= []
   for event in r_events:
      overlap_no=[]
      for num in event:
         complist = [abs(x-num) for x in event]
         complist.remove(0.0)
         if all(i > width for i in complist):
```

```
            overlap_no.append(num)

        goodioncount.append(len(overlap_no))
        goodionspectrum.append(overlap_no)

    simgoodspectrum = [i for sublist in goodionspectrum for i in sublist]  #all "good ions" in 1D
list (no overlap)
    counted_simgoodspectrum.append(simgoodspectrum)
    totals.append(len(simgoodspectrum))
    print(len(simgoodspectrum))
    print(ioncount)
#Creates a file with the total number of non-overlapping ions at each ion count
with open(folder+"/ionnumfilename.txt","w",newline='') as good_ions:
    wr = csv.writer(good_ions, delimiter="\t",)
    wr.writerow(totals)

#Creates a file with a list of all non-overlapping ion frequencies at each ion count
with open(folder+"/ionfreqfilename.txt","w",newline='') as good_freqs:
    wr = csv.writer(good_freqs, delimiter="\t",)
    wr.writerows(counted_simgoodspectrum)

#number of good ions in each iteration of ioncount (e.g. 1000 good ions with an ioncount of 1, 2
good ions for 2 etc.)
print(totals)
```

Chapter 5

Direct Observation of Ion Emission from Charged Aqueous Nanodrops: Effects on Gaseous Macromolecular Charging

This chapter is reproduced with permission from:

Conner C. Harper, Daniel D. Brauer, Matthew B. Francis, and Evan R. Williams

"Direct Observation of Ion Emission from Charged Aqueous Nanodrops: Effects on Gaseous Macromolecular Charging" *Submitted to Chemical Science.* **2020.**

5.1 Abstract

Mechanistic information about how gaseous ions are formed from charged droplets has been difficult to establish because direct observation of nanodrops in a size range relevant to gaseous macromolecular ion formation by optical or traditional mass spectrometry methods is challenging owing to their small size and heterogeneity. Here, the mass and charge of individual aqueous nanodrops between 1 – 10 MDa (15 – 32 nm diameter) with ~50 – 300 charges are dynamically monitored for 1 s using charge detection mass spectrometry. Discrete losses of minimally solvated singly charged ions occur, marking the first direct observation of ion emission from aqueous nanodrops in late stages of droplet evaporation relevant to macromolecular ion formation in native mass spectrometry. Nanodrop charge depends on the identity of constituent ions, with pure water nanodrops charged slightly above the Rayleigh limit and aqueous solutions containing alkali metal ions charged progressively below the Rayleigh limit with increasing cation size. MS2 capsid ions (~3.5 MDa; ~27 nm diameter) are more highly charged from aqueous ammonium acetate than from its biochemically preferred, 100 mM NaCl/10 mM Na phosphate solution, consistent with ion emission reducing the nanodrop and resulting capsid charge. The extent of charging indicate that the capsid partially collapses inside the nanodrops prior to the charging and formation of the dehydrated gaseous ions. These results demonstrate that ion emission can affect macromolecular charging and that conformational changes to macromolecular structure can occur in nanodrops prior to the formation of naked gaseous ions.

5.2 Introduction

Electrospray ionization (ESI) is used in thousands of laboratories worldwide to produce ions directly from solution for analysis by mass spectrometry (MS), yet the mechanism(s) by which gaseous ions are generated has been subject to conjecture and much debate.[1–4] Charged droplets initially generated by electrospray undergo solvent evaporation, which increases the strength of

the electric field at the droplet surface. This can lead to droplet fission when the charge-charge repulsion exceeds the ability of the droplet to stay intact. The extent of charging necessary for fission of a spherical droplet to occur is given by the Rayleigh equation (5.1):[5]

$$Z_R = 8\pi(\varepsilon_0 \gamma R^3)^{1/2} \quad (5.1)$$

where γ is the surface tension, Z_R is the charge on a spherical droplet with a radius, R, ε_0 is the permittivity of free space and *e* is the elementary charge. Fission occurs when a droplet reaches the Rayleigh limit (Z_R), resulting in the emission of smaller charged droplets from the surface. The Rayleigh fission process has been investigated for large droplets (>10s of μm) using a variety of experimental apparatus.[6–8] Leisner and coworkers used high-speed microscopy to show the Rayleigh induced breakup of ~24 μm ethylene glycol droplets, which resulted in the formation of ~100 progeny droplets that carry away ~33% of the charge of the original droplet, but only 0.3% of its mass.[6] Successive fission events of individual charged droplets between 5 – 40 μm were measured using phase Doppler interferometry combined with a drift field reversing "ping-pong" technique.[7] Fission of small water droplets (5 – 20 μm) occurred near the Rayleigh limit whereas acetonitrile and methanol droplets charged up to 120% of the Rayleigh limit prior to fission.[7]

Observing discharge events for smaller "nanodrops" (10 – 100's of nm) is more difficult than for μm-sized droplets because of the challenge associated with using optical methods with droplets that are smaller than the wavelengths of light. Nanodrops containing one or more ions with up to ~600 water molecules, corresponding to diameters <2 nm, have been trapped, mass analyzed, and probed using infrared photodissociation spectroscopy and ultraviolet photodissociation to obtain information about ion-water interactions[9–11] and water molecule binding energies.[12] Charge separation processes can occur in these small nanodrops that contain multivalent ions when sequential evaporation of water molecules reduces the cluster size to where the multivalent ion is no longer stable.[11–14] For example, $La^{3+}(H_2O)_n$ undergoes charge separation to form $H^+(H_2O)_x$ and $LaOH^{2+}(H_2O)_y$ when $n < 19$.[14] Transitions between conformations of small peptides in solution to their stable gaseous ion conformations have been measured with ion mobility of hydrated ions.[15] These cluster studies provide information about processes that occur very late in the dehydration stages of gaseous ions formed by electrospray. However, there remains a significant gap in nanodrop size (2 – 1000 nm) for which direct experimental observations have not previously been possible.

Because of the inability to directly monitor what occurs inside aqueous nanodrops between 2 and 1000 nm, much of what is thought about how gaseous ions are formed has been inferred indirectly from a number of different measurements and from theory. Most mechanisms for dehydrated gaseous ion formation are variations on two long-standing models: the ion evaporation model (IEM)[16] and the charge residue model (CRM).[17] In the CRM, solvent evaporation occurs from small droplets that contain one or more analyte molecules, and the analyte charge is limited by the charge on the droplet.[17] This mechanism is widely invoked in native mass spectrometry where charging of large proteins and macromolecular complexes follows a trend in charging that is limited by the Rayleigh charge on a droplet of similar size to that of the analyte.[3] Charging of analyte molecules that cannot change conformation follows this trend for solvents with different surface tensions.[18] In the IEM, ions are ejected from the surface of small droplets (~10 nm) with only a limited number of solvent molecules when the electric field at the surface is sufficiently

high.[16] The IEM has been widely invoked for the formation of small ionic species.[2,4,16] Ion emission events are characterized by the ejection of ions that carry only a small number of solvent molecules in addition to the charge carrier.[4,16,19] Less highly solvated ions are more readily emitted from a droplet, consistent with formation of more abundant gaseous alkali metal cations and halide anions with increasing ion size.[20]

Formation of gaseous ions from small highly charged nanodrops has been investigated computationally.[4,19,21–23] Molecular dynamics (MD) simulations support ion evaporation of Na^+ and other small ions from nanodrops with diameters <5.5 nm.[21–23] For droplets that contain larger analytes, results from MD simulations suggest the possibility of several different mechanisms. Simulations by Consta and co-workers indicate that significant distortions of the droplets into "star" morphologies can occur.[22] Simulations by Konermann and co-workers suggest a chain ejection model in which an unfolded or unfolding protein at the surface of the droplet is extruded into the gas phase (an IEM-like process) followed by a stepwise ejection of the remainder of the protein chain.[4] This process is analogous to the process for asymmetric charge partitioning typically observed for the collision induced dissociation of large macromolecular complexes.[24,25] Recent simulations by Aliyari and Konermann suggest an ion emission-like process may also occur for small native proteins that carry a sufficiently high charge in solution.[23]

A hybrid model that combines both the charge residue and field emission models (combined charge residue and field emission model or CCRFEM) was proposed by Hogan et al.[26] In this model, the charge states of proteins and other macromolecules are not determined solely by the Rayleigh limit of a droplet of similar size, as would the be case for just the CRM, but rather the charge is also limited by field-induced emission of small charged solute ions and clusters from the protein-containing nanodroplet (an IEM process).[26] Ions that are not as highly solvated are more easily emitted from the droplet and leave less charge available for the protein. A tandem differential mobility analysis of submicrometer particles indicates a transition from Rayleigh fission-controlled to ion emission-controlled discharging occurs for methanol-water nanodrops at ~40 nm.[27] The mean charge state of several proteins ionized from aqueous ammonium acetate (AA) is higher than that from triethylammonium bicarbonate, consistent with the lower solvation energy of the latter cation.[26] However, there was no significant difference in the charging of several proteins with different pI values from solutions containing different alkali metal acetates, suggesting that ions with widely different solvation energies do not necessarily affect protein charging.[28] A complication with these experiments is that protein conformation, which has a significant effect on protein charging, can differ in solutions with different ionic constituents, even when the ionic strength of the solutions is the same.[29] There have been no direct experimental observations of ion emission from nanodrops in the size range (~10–40 nm) where ion emission is thought to play a role in the charging of macromolecules in the CCRFEM.

Charge detection mass spectrometry (CDMS) can weigh individual ions well into the 100s of megadaltons (MDa) corresponding to molecules or molecular assemblies with diameters over 100 nm.[30–36] Sample heterogeneity and salt adduction can lead to overlapping ion signals that can prevent conventional mass spectrometry measurements of ion ensembles.[37,38] This problem with high sample heterogeneity is overcome with CDMS measurements of individual ions, making it an ideal technique for probing charged nanodrops. These measurements can serve as a bridge

between what is known about micron-sized droplet charging and fission and events that occur for nanodrops closer to the size of typical analyte molecules.

Here, aqueous nanodrops ranging in mass from ~1 – 10 MDa (~15 – 32 nm diameter) are investigated using CDMS. The nanodrop charge and mass depends on the identity of salts in solution, and these values change over the one second trapping time, leading to the first direct observation of ion emission from nanodrops in a size range representing late stages of droplet evolution prior to formation of gaseous ions of proteins and macromolecular complexes. Differences in charging of the bacteriophage MS2 capsid formed from aqueous ammonium acetate versus its biochemically preferred sodium-containing buffer solution indicate that solute ion identity affects the final charge states of this complex through ion evaporation of small ions. Moreover, the extent of charging indicates that the structure of the capsid collapses in the nanodrop prior to gaseous ion formation.

5.3 Experimental

5.3.1 Charge Detection Mass Spectrometry

All mass and charge data for individual ions were obtained using a home-built charge detection mass spectrometer.[32,33] Nanoelectrospray ionization using borosilicate capillaries (1.0 mm outer diameter, 0.78 mm inner diameter, Sutter Instruments, Novato, CA) with tips that are pulled to an inner diameter of ~1.5 μm using a Flaming/Brown P-87 micropipette puller (Sutter Instruments, Novato, CA) is used to introduce ions into the instrument through a modified Waters Z-Spray source (Waters Corporation, Milford, MA). Ions enter a region containing two RF quadrupole ion guides (Ardara Technologies, Ardara, PA) and are accumulated in the second ion guide for up to 1 s. They are pulsed into the electrostatic ion trap at a pressure of ~4×10^{-9} Torr where they are stored for 1 s. A charge pulse is induced each time an ion traverses the detector tube. Individual ion masses, charges, and energies are dynamically determined from the measured oscillation frequencies and amplitudes of the fundamental and second harmonic frequencies[39] as they evolve throughout the 1 s trapping period. The broad distribution of ion mass and charge in these experiments makes it possible to simultaneously analyze up to ~40 individual ions in each trapping event because the frequency distribution of the ions is broad and their signals are less likely to interfere with each other.[40,41] Signals are analyzed using short-time Fourier transforms (STFT)[41] using a 25 ms segment length stepped across the transient in 5 ms increments. This segment length was chosen to minimize amplitude dampening that is caused by ion frequency shifts with time.[40] Data for only those ions trapped and detected for the entire 1 s trapping period (>70 % of all ions) were analyzed. Additional experimental details are provided in the Supporting Information. Aqueous solutions of ammonium acetate (AA), LiCl, NaCl, KCl and CsCl at 20 mM salt solutions were prepared using Millipore Milli-Q water.

5.3.2 MS2 Capsid Synthesis

Bacteriophage MS2 virus-like particles were produced as previously described (ref).[42] d In brief, DH10B *E. coli* containing a pBAD MS2 expression vector (chloramphenicol resistant) was grown to OD0.6 in 2xYT media at 37 °C. Expression was induced via addition of arabinose to 0.1% (w/v) and cultures were incubated for 18 h at 37 °C. Cells were then harvested via centrifugation and lysed by sonication. The collected lysate was purified through two rounds of

ammonium sulfate precipitation at 50% saturation followed by polishing on an ÄKTA start FPLC system using a prepacked Sephacryl S-500 HR column. The resultant purified capsids were buffer exchanged into the desired buffers using a 100 kDa MWCO spin concentrator. Details about the small angle x-ray scattering (SAXS) and dynamic light scattering (DLS) experiments performed on MS2 solutions are provided in the Supporting Information.

5.4 Results and Discussion

5.4.1 Acquiring Individual Nanodrop Data

The mass and charge of individual nanodrops generated by electrospray ionization from solutions consisting of either pure water or aqueous solutions with various salts at a concentration of 20 mM were measured using CDMS. Data were acquired with "soft" ESI conditions where the voltage difference between skimmer cones (~5 Torr region) is low (~35 V) to minimize collisional activation. Ions are trapped in a quadrupole ion guide for between 0 – 1 s prior to introduction into the electrostatic ion trap for 1 s. The resulting nanodrop lifetimes are between ~1 and 2 s during which time the frequency and intensity of each ion is measured. The energy of each ion throughout the measurement is obtained from the ratio of the amplitude of the 2nd harmonic frequency to that of the fundamental frequency.[39] The *m*/*z* of each ion is obtained from its energy and frequency, and the charge is obtained from the amplitude of the signal.[39,43] Thus, the mass, charge, and energy of every ion is measured and tracked throughout the 1 s trapping time. The data from many such trapping events are compiled until a statistically robust number of ions (typically several thousand) are measured.

An example of short-time Fourier transform (STFT) data obtained from a single trapping event for ions produced from a 20 mM solution of NaCl is shown in Figure 5.1. This STFT analysis method makes it possible to obtain the evolution of the ion frequency (*y*-axis) and amplitude (color scale) over the trapping period (*x*-axis) with a time resolution of 5 ms corresponding to the STFT step size. Several individual ion signals, corresponding to contiguous lines, persist over the acquisition time. The signal amplitudes are related to the ion charge[43] and the ion frequencies (*f*) are related to the *m*/*z* of ions via equation 5.2:

$$\frac{m}{z} = \frac{C(E)}{f^2} \tag{5.2}$$

where *C(E)* is a function of ion energy per charge.[33,39] Ion frequencies increase, e.g., **A** and **C** in Figure 5.1, as a result of both collisional energy losses to the background gas and energy lost as a result of neutral mass losses, i.e., water evaporation from the nanodrops. Discrete, negative frequency changes occur as a result of sudden charge loss, which increases the *m*/*z* of the remaining nanodrop. Examples of these charge losses can be seen in ion signals **B, C,** and **D** in Figure 5.1. Ion signals may occasionally overlap and interfere in frequency space, as occurs for ion signals **D** and **E** in Figure 5.1. Data from such interfering ions are not used in subsequent analysis.

The two pathways for energy loss, collisions with background gas and neutral mass losses, can be deconvolved, making it possible to measure the neutral mass that is lost from each nanodrop during the trapping event.[39] The ranges of mass loss from the initially trapped ions can

vary widely depending on the solution composition, but some of the initially trapped ions lose 100s of kDa. Significant mass is lost from pure aqueous nanodrops, indicating that evaporation of up to many thousands of water molecules occurs. Such high evaporative losses from ions are not typically observed in CDMS experiments because greater initial ion activation is commonly used to desolvate ions when measuring the masses of large macromolecules.

5.4.2 Nanodrop Mass and Charge Distributions from Different Solutions

Two-dimensional mass vs. charge histograms for ions formed from solutions of pure H_2O and aqueous solutions containing AA, LiCl, NaCl, KCl, and CsCl, each at 20 mM, are shown in Figure 2a–f, respectively. The red lines correspond to the Rayleigh charge limit for a pure aqueous spherical droplet calculated using the bulk surface tension (0.07286 N/m at 20 °C) and the density (0.998 g/mL at 20 °C) of water. The number of ions in each histogram bin, corresponding to a small range of mass and charge, is represented with a color scale. Although many charged nanodrops lose significant mass and/or charge (Figure 5.1), only the average masses and charges were used in these histograms for simplicity (Table 5.1).

The charged nanodrops formed from pure H_2O (Figure 5.2a) have the largest average mass and charge. The average mass and charge from AA (Figure 5.2b) are about 1 MDa and 50 *e* lower. The mass and charge continue trending downward for the alkali metal ions with increasing cation size (Figures 5.2c–5.2f). Ions produced from aqueous CsCl have on average ~25% of the mass and charge of the pure aqueous nanodrops. The relationship between nanodrop mass and solute ion identity is discussed in the Supporting Information. The charge of each ion was divided by the Rayleigh charge limit for an aqueous droplet (red line) for an ion of that mass to give the ion charge as a percentage of the expected Rayleigh charge (Table 5.1). Notably, ions formed from pure water are on average charged well above the computed Rayleigh limit (118%) whereas ions from all other solutions are typically charged below the limit (~56% with CsCl). For H_2O and AA, higher mass nanodrops (>3 MDa) tend to be more highly charged relative to the Rayleigh limit compared to lower mass ions from the same solution, perhaps as a result of deviations in surface tension from bulk values at smaller nanodrop size. There is also a strong dependence between alkali metal ion size and charging relative to the Rayleigh limit, with the LiCl solution having the highest average charge relative to the Rayleigh limit (96%) and CsCl the lowest (56%).

Interpretation of data for nanodrops formed from LiCl and NaCl solutions is complicated by the presence of two distinct distributions of ions with overlapping masses but with different charges. Ions in one distribution are charged below the Rayleigh limit whereas ions in the other distribution are charged slightly above the Rayleigh limit. Due to these differences, these ion distributions in the LiCl and NaCl data were analyzed separately. Data for NaCl obtained under more typical activating conditions resulted in only the lower charge distribution. Based on these and other data, the higher charge distribution for LiCl and NaCl are referred to as “wet” whereas the lower charge distribution is referred to as “dry”. The “wet” LiCl and NaCl ion distributions follow the trend of greater deviation from the Rayleigh limit with greater mass noted for H_2O and AA. In contrast, the lower charge, “dry” distributions are more qualitatively similar to the KCl and CsCl ion distributions.

5.4.3 Comparing Individual “Dry” and “Wet” Ions

Because CDMS measurements are made on an ion-by-ion basis, analysis of individual ion signals can provide additional insights into the overall analyses of ion ensembles. For ion ensembles containing more than one distribution of ions, such as LiCl and NaCl, this type of analysis is especially informative because different physical traits of ions that make up the two distinct "wet" and "dry" ion distributions can be distinguished. Five individual ions from both the "wet" and "dry" distributions from NaCl were randomly selected from different trapping events, and the STFT ion peak amplitude traces are shown together in Figure 5.3. Blue traces correspond to the "dry" individual ions below the white dotted line of Figure 5.2D; red traces correspond to "wet" ions above the line. The frequencies of ions from the "dry" distribution (blue) remain relatively constant, indicating that the *m*/*z* values and ion energies do not change significantly over the trapping period. However, some abrupt drops in frequency that correspond to charge losses occur (circled in black in Figure 5.3). Although a sample of only five ions is shown in Figure 5.3, nearly all ions in the lower charge distribution exhibit similar behavior. Ions from the higher charge "wet" distribution (red) also show abrupt frequency drops (black circles), but in contrast with the ions in the lower charge "dry" distribution, the frequency of these ions increases significantly at all other times. The frequencies of these ions continuously increase as a result of neutral mass losses on the order of ~100 kDa (~5600 water molecules). Mass loss data for each solution as well as the "wet" and "dry" distributions observed for LiCl and NaCl are included in Table 5.1. Nearly all ions in the upper charge distribution undergo more extensive mass loss than ions in the lower distribution. This individual ion analysis provides additional support for the classification of the two distributions as "wet" and "dry" ions with notably different physical characteristics. Although the two distributions are distinguished as "wet" and "dry", the ions in the "dry" distribution still undergo measurable mass loss that indicates that these ions are still hydrated, but less so than the corresponding "wet" distribution.

5.4.4 Direct Observations of Ion Emission

The sporadic, negative frequency changes observed for many of these ions (Figure 5.3, black circles) correspond to charge losses (average number of ion emission events per nanodrop is given in Table 5.1). The charge before and after each event is determined to obtain the number of charges lost in each event. A histogram of the charge lost in ion emission events for ions formed from 20 mM aqueous NaCl is shown in Figure 5.4. Similar histograms for the other solutions for which a significant number of ion emission events were observed (H_2O, AA, LiCl) are included in the Supporting Information. Few ion emission events were observed from either KCl or CsCl solutions. Only ions that survive for at least 100 ms before and after the ion emission event without another ion emission event occurring were included in these histograms in order to decrease the charge uncertainty, which is ~1.8 e for 100 ms measurements with this CDMS instrument.[43] The histogram data were fit with a Gaussian function (red dashed line in Figure 5.4) and the mean charge loss at each ion emission event for the NaCl data in Figure 5.4 is 1.1 *e* with a standard error of 0.07 *e*. The mean mass loss associated with these charge losses is close to zero, consistent with a minimally solvated ion being emitted from the droplet (Supporting Information). Because charge must be an integer value, we conclude that nearly all the ion emission events correspond to loss of a single charge. Loss (and gain) of a single charge from large analyte ions has been observed previously,[44–46] but the data reported here represents the first time that ion emission has been

directly observed from aqueous nanodrops and in a size range (~1 – 10 MDa, ~15 – 32 nm diameter) relevant to formation of gaseous macromolecule ions.

The probability an ion emission event for a given charged nanodrop depends on the identity of the solute ion with H_2O and AA having a discharge rates of ~0.2 events per ion, whereas KCl and CsCl) exhibit few such events (<0.01). The extent of "wetness" or "dryness" does not appear to be directly related to the extent of ion evaporation. For LiCl and NaCl where both "dry" and "wet" ions are observed simultaneously, the rate of charge loss events for these two different types of ions do not appear to be correlated (also indicated in the Figure 5.3 data), suggesting that "dryness" alone does not determine the probability of discharging events. The mass of the precursor ion also does not directly correlate to discharge rates. For the alkali metal ion solutions, there is a clear trend of decreasing ion emission rate with increasing cation size (Table 5.1).

5.4.5 Origins of Solution-Dependent Nanodrop Mass and Charge

The masses of nanodrops and their corresponding charges depend on the identity of ions present in these aqueous solutions. These results do not appear to be the result of differences in initial droplet sizes produced by electrospray ionization. The conductivity of pure water is lower than that of the ion containing solutions and may lead to differences in initial droplet size. However, the initial droplet sizes for the alkali metal ion containing solutions should be the same, yet the trapped nanodrops are clearly different in mass and charge. Any differences in conductance, vapor pressure, or surface tension in the initial droplets should be minor at 20 mM concentration. Because the surface tension of the droplets of the different solutions should be approximately the same, Rayleigh fission events for the initial droplets should also be similar at these concentrations. Thus, the differences in the nanodrops that are observed in these experiments must originate from processes that occur after the initial droplet is formed and the first of any Rayleigh fission events that may occur.

The trend in lower charging with increasing cation size for the alkali metal ions follows the trend in ion cation solvation energies where the Gibbs solvation energy of Li^+ is 575 kJ/mol relative to the solvation energy of H^+ (assigned a value of 0 kJ/mol) and is lower than that of Cs^+ (798 kJ/mol).[47] H^+ has the lowest Gibbs solvation energy, and the concentration of this ion in pure water is substantially lower than the positive ions in the other solutions. Both factors should make ion emission less favored for pure water compared to other solutions. Because pure H_2O nanodrops lack an abundant suitable ion emission "release valve" for excess charge, the formation of more highly charged ions may be kinetically favored leading to "supercharged" nanodrops with charge above the Rayleigh limit (Figure 5.2a). This may explain the higher charging observed for micron-sized droplets consisting of volatile solvents,[7] which evaporate more rapidly than pure water. Results for the AA containing nanodrops do not follow the trends in cation solvation energies of the other solutions. The solvation energy of NH_4^+ is between that of K^+ and Rb^+ yet the charges and masses of the AA containing nanodrops are more similar to that of water than that of KCl. The counterions (acetate vs. Cl^-) differ and may also influence the evaporation process for the cations. Unlike the alkali metal ion salts, AA can undergo proton transfer processes creating a path for their loss as neutrals, which may also lead to the observed differences.

These results provide compelling evidence for the CCRFEM. The observation of ion emission from 15 – 32 nm nanodrops is consistent with conclusions from prior work which indicated a transition between Rayleigh limited charging and solute ion emission-controlled charging at ~40 nm.[27] It is interesting to speculate why charging of proteins and peptides from different solutions have provided limited support for this model. Ions of β-lactoglobulin, bovine ubiquitin and egg-white lysozyme are more highly charged from pure water than from solutions containing alkali metal ions (acetate salts),[28] consistent with higher charging of aqueous nanodrops. However, the extent of charging of these proteins from solutions containing Li^+, Na^+, K^+, Rb^+, Cs^+ as well as NH_4^+ are similar.[28] There is no significant trend in protein ion charging and ion solvation energy except with minimally solvated TMA and TEA.[28] The significantly lower charge states observed with the latter ions was attributed to collisional dissociation of these positively charged ions from the proteins, a process that occurs to a much lesser extent with the other ions.[28] Protein conformation also plays a significant role in the extent of charging on proteins.[29] It is also apparent that the differences in nanodrop charging relative to the Rayleigh limit for these solutions become less distinct when the nanodrop mass is below ~1 MDa (15 nm diameter). Thus, charging differences predicted by the CCRFEM may not be as applicable to smaller proteins or macromolecular complexes.

5.4.6 The Role of Ion Evaporation in Charging of MDa Macromolecules

The substantial differences in the charging of MDa-sized nanodrops originating from pure water and different salt solutions suggest that these effects may also affect the charging of molecules that have comparable size to the nanodrops investigated here (~15 – 32 nm diameters). To investigate if that is the case, an MS2 capsid with a theoretical "empty" mass of 2466 kDa and a diameter of 27 nm[48] was analyzed using CDMS from a biochemically preferred solution consisting of 100 mM NaCl and 10 mM Na phosphate (NaX) and from a 100 mM AA solution commonly used in native mass spectrometry. Source conditions were made more energetic than the nanodrop experiments described above by increasing the voltage between skimmer cones to ~150 V to desolvate these ions more effectively. The resulting 1D mass histograms and the 2D mass vs. charge histograms are shown in Figure 5.5. There are two broad high mass peaks in the 1D mass histograms from both solutions (Figures 5.5a and 5.5b) that are separated by ~670 kDa. There is an additional, poorly resolved low abundance peak between these two main peaks that is more apparent in the mass histogram from AA (Figure 5.5a). A Gaussian fit of the two most abundant peaks from both solutions results in mass values of 2.76 MDa and 3.42 MDa from AA and 3.00 and 3.67 MDa from NaX. All ions in both solutions that compose these two peaks are "dry", with no measurable mass change over their lifetimes in the trap. Because the widths of these peaks are much greater than the intrinsic linewidth (shown in yellow), each peak must consist of unresolved MS2 capsid species that have encapsulated a range of different cargoes. The native virus RNA (1147 kDa) was not present during the virus assembly. Thus, the heterogeneity observed is almost certainly a result of varied encapsulation of messenger RNA and/or DNA transcripts from the recombinant expression of the capsid, a phenomenon that has been observed previously for MS2 capsids.[48]

The relative abundances of the two major ions from both solutions are similar (Figures 5.5a and 5.5b). The principal difference between the two mass histograms is that ions formed from the NaX solution are shifted ~250 kDa (~8%) higher in mass and the distributions are wider (~13%

larger standard deviations). The higher mass and wider peak width are almost certainly the result of extensive adduction of non-volatile salts present in the NaX solution. This is the first time that MDa-sized macromolecular ions have been analyzed in native MS from a solution containing a 100+ mM concentration of non-volatile salts.

The charge states of the MS2 capsids produced from these two solutions are significantly different. The average charge of MS2 capsid ions formed from the NaX solution is ~13 charges (~10%) lower than the average charge of these ions formed from the AA solution despite the higher masses of the former ions. This can be readily seen from the white oval in Figure 5.5d, which shows the range of the higher mass ions formed from AA. This white oval is shifted to lower mass but higher charge. Differing charge-state distributions are most often attributed to conformational changes.[49] To determine if there are differences in MS2 capsid size indicative of a conformational difference between the two solutions, small angle x-ray scattering (SAXS) experiments were performed.[50] The SAXS data indicate that the MS2 capsid is slightly more compact in NaX (0.42 ± 0.93 nm smaller diameter relative to that in AA), representing a ~3% relative change in the surface area (Fig. S5.8). For molecular assemblies with near spherical shape, the extent of charge on the ions formed by electrospray should be proportional to surface area.[17] Thus, this small difference in diameter does not fully account for the 10% difference in the charge. Dynamic light scattering (DLS) experiments were also performed to verify capsid diameter consistency in both solutions. The DLS data show no detectable capsid size shift between these two buffer systems (Fig. S5.9). The effect of any acidification of the solution that may occur during the electrospray process was also explored. DLS data for solutions ranging in pH between 3.5 and 7.5 display no evidence of contraction in capsid diameter in more acidic solutions (Fig. S5.10). Thus, it is unlikely that the different charge distributions observed from the two solutions originate from a conformational difference in these two solutions.

The extent of charging of nanodrops with similar physical sizes to that of the MS2 capsid provides insights into the origin of differences of MS2 capsid charging from the two solutions. Aqueous nanodrops with AA are charged to a greater extent than those with NaCl, consistent with the relative extents of charging of the MS2 capsid from the two different solutions. The average charge of the larger, most abundant MS2 species formed from AA solution (Figure 5.5c) is 141.5 *e*, similar to the value of ~145 *e* for AA containing nanodrops in the same mass range (Figure 5.2b). In contrast, the average charge for the MS2 base peak from NaX (Figure 5.5d) is 128.5 *e*, which more closely matches the charge of the "dry" distribution of ions produced from the NaCl solution at similar mass (Figure 5.2d, ~120 *e*).

5.4.7 Evidence for Solution Phase Capsid Compaction

The MS2 capsid is roughly spherical in solution with a diameter of 27 nm.[48] A 27 nm diameter AA nanodrop has ~200 *e* whereas MS2 ions formed from AA have ~142 *e.* The lower charging of the capsid indicates that the structure collapses to a significant extent in the nanodrop prior to charging of the gaseous ion. An estimate of the MS2 capsid diameter of 21.8 nm is obtained from AA nanodrops with the same charge. The apparent capsid density of 1.04 g/mL is substantially less than that of an average protein (1.35 g/mL)[51] or RNA/DNA (~1.7 g/mL),[52] suggesting that this compaction is not complete. The extent to which native macromolecular structure is preserved in the gas phase is a matter of ongoing debate.[53,54] Ion mobility

measurements have shown that large protein complexes, such as GroEl, can undergo a "gas-phase collapse" to produce a compacted structure.[54] This compaction is generally assumed to take place after gaseous ion formation.[55–57] Our data indicate that the structure of MS2 capsid is compacted by ~5 nm in diameter relative to its solution-phase structure and that this compaction must occur prior to the final stages of nanodrop evaporation where the charge of the analyte is determined.

5.5 Conclusions

The masses and charges of nanodrop ions generated from pure H_2O and 20 mM aqueous solutions of AA, LiCl, NaCl, KCl, and CsCl were measured on an ion-by-ion basis using CDMS. Nanodrop sizes ranging from 1 – 10 MDa (15 – 32 nm diameter) are trapped and the mass and charge evolution of individual ions show that two distinct types of ions were generated. "Wet" ions from the H_2O, AA, LiCl, and NaCl solutions, exhibited significant mass loss corresponding to evaporation of thousands of water molecules over the 1 s trapping time whereas "dry" ions from LiCl, NaCl, KCl, and CsCl solutions lost little mass. Ion emission events corresponding to the loss of a singly charged minimally solvated ion occurs for both "wet" and "dry" ions. This is the first direct observation of ion emission from aqueous nanodrops in the nanometer size range. These results provide compelling evidence for the CCRFEM for charging of MDa+ macromolecular complexes in native mass spectrometry. Charging of the nanodrops depends on the identity of charge carriers in solution. There is clear trend of lower nanodrop mass and charge with increasing alkali metal cation size, and these results also indicate that solute identity affects droplet evaporation after the initial formation of the charged droplets.

The mass and charge distribution of MS2 capsid ions from AA typically used in native MS differs from those formed from a biochemically preferred NaX solution containing 100+ mM of non-volatile solutes. Ions formed from NaX have ~8% higher masses as a result of extensive adduction, but significantly lower charge, consistent with ion evaporation of Na^+ lowering the charge on the droplets from which these ions are formed. The extent of MS2 capsid charging from the AA solution indicates that the structure partially collapses in the nanodrops prior to when charging of the gaseous ions occurs. Ion mobility results have shown that compaction of other macromolecular assemblies occur,[54] but our results localize this compaction to a time prior to gaseous ion formation. This is the first time MDa-sized ions have been analyzed in native MS from a biochemically relevant solution. Future work on calibrating the mass shift based on peak widths, analogous to what has been done for much smaller complexes,[58] could make this a practical method to obtain accurate masses of large complexes from a wide range of buffers that contain nonvolatile salts typically used in biochemistry.

5.6 Acknowledgements

This material is based upon work supported by the National Science Foundation Division of Chemistry under grant number CHE-1609866. The authors are also grateful for financial support from CALSOLV. This work was also supported by the Immunotherapeutics and Vaccine Research Initiative at UC Berkeley. SAXS data was collected at SIBYLS which is supported by the DOE-BER IDAT DE-AC02-05CH11231 and NIGMS ALS-ENABLE (P30 GM124169 and S10OD018483).

5.7 References

(1) Fenn, J. B.; Mann, M.; Meng, C. K.; Wong, S. F.; Whitehouse, C. M. Electrospray Ionization–Principles and Practice. *Mass Spectrom. Rev.* **1990**, *9* (1), 37–70.

(2) Kebarle, P.; Peschke, M. On the Mechanisms by Which the Charged Droplets Produced by Electrospray Lead to Gas Phase Ions. *Anal. Chim. Acta* **2000**, *406* (1), 11–35.

(3) Fernandez De La Mora, J. Electrospray Ionization of Large Multiply Charged Species Proceeds via Dole's Charged Residue Mechanism. *Anal. Chim. Acta* **2000**, *406* (1), 93–104.

(4) Konermann, L.; Ahadi, E.; Rodriguez, A. D.; Vahidi, S. Unraveling the Mechanism of Electrospray Ionization. *Anal. Chem.* **2013**, *85* (1), 2–9.

(5) Rayleigh, Lord. XX. On the Equilibrium of Liquid Conducting Masses Charged with Electricity. *London, Edinburgh, Dublin Philos. Mag. J. Sci.* **1882**, *14* (87), 184–186.

(6) Duft, D.; Achtzehn, T.; Müller, R.; Huber, B. A.; Leisner, T. Coulomb Fission: Rayleigh Jets from Levitated Microdroplets. *Nature* **2003**, *421* (6919), 128.

(7) Smith, J. N.; Flagan, R. C.; Beauchamp, J. L. Droplet Evaporation and Discharge Dynamics in Electrospray Ionization. *J. Phys. Chem. A* **2002**, *106* (42), 9957–9967.

(8) Zilch, L. W.; Maze, J. T.; Smith, J. W.; Ewing, G. E.; Jarrold, M. F. Charge Separation in the Aerodynamic Breakup of Micrometer-Sized Water Droplets. *J. Phys. Chem. A* **2008**, *112* (51), 13352–13363.

(9) OBrien, J. T.; Williams, E. R. Effects of Ions on Hydrogen-Bonding Water Networks in Large Aqueous Nanodrops. *J. Am. Chem. Soc.* **2012**, *134* (24), 10228–10236.

(10) Cooper, R. J.; Ditucci, M. J.; Chang, T. M.; Williams, E. R. Delayed Onset of Crystallinity in Ion-Containing Aqueous Nanodrops. *J. Am. Chem. Soc.* **2016**, *138* (1), 96–99.

(11) DiTucci, M. J.; Williams, E. R. Nanometer Patterning of Water by Tetraanionic Ferrocyanide Stabilized in Aqueous Nanodrops. *Chem. Sci.* **2017**, *8* (2), 1391–1399.

(12) Ditucci, M. J.; Heiles, S.; Williams, E. R. Role of Water in Stabilizing Ferricyanide Trianion and Ion-Induced Effects to the Hydrogen-Bonding Water Network at Long Distance. *J. Am. Chem. Soc.* **2015**, *137* (4), 1650–1657.

(13) Wong, R. L.; Williams, E. R. Dissociation of SO42-(H2O)n Clusters, n = 3-17. *J. Phys. Chem. A* **2003**, *107* (50), 10976–10983.

(14) Bush, M. F.; Saykally, R. J.; Williams, E. R. Reactivity and Infrared Spectroscopy of Gaseous Hydrated Trivalent Metal Ions. *J. Am. Chem. Soc.* **2008**, *130* (28), 9122–9128.

(15) Silveira, J. A.; Fort, K. L.; Kim, D.; Servage, K. A.; Pierson, N. A.; Clemmer, D. E.; Russell, D. H. From Solution to the Gas Phase: Stepwise Dehydration and Kinetic Trapping of Substance p Reveals the Origin of Peptide Conformations. *J. Am. Chem. Soc.* **2013**, *135* (51), 19147–19153.

(16) Iribarne, J. V.; Thomson, B. A. On the Evaporation of Small Ions from Charged Droplets. *J. Chem. Phys.* **1976**, *64* (6), 2287–2294.

(17) Dole, M.; Mack, L. L.; Hines, R. L.; Chemistry, D. O.; Mobley, R. C.; Ferguson, L. D.; Alice, M. B. Molecular Beams of Macroions. *J. Chem. Phys.* **1968**, *49* (5), 2240–2249.

(18) Iavarone, A. T.; Williams, E. R. Mechanism of Charging and Supercharging Molecules in Electrospray Ionization. *J. Am. Chem. Soc.* **2003**, *125* (8), 2319–2327.

(19) Ichiki, K.; Consta, S. Disintegration Mechanisms of Charged Aqueous Nanodroplets Studied by Simulations and Analytical Models. *J. Phys. Chem. B* **2006**, *110* (39), 19168–19175.

(20) Wang, G.; Cole, R. B. Solvation Energy and Gas-Phase Stability on Alkali Metal Cluster Ion Formation in Lonization Mass Spectrometry. *Anal. Chem.* **1998**, *70* (5), 873–881.

(21) Konermann, L.; Metwally, H.; Duez, Q.; Peters, I. Charging and Supercharging of Proteins for Mass Spectrometry: Recent Insights into the Mechanisms of Electrospray Ionization. *Analyst*. Royal Society of Chemistry November 7, 2019, pp 6157–6171.

(22) Sharawy, M.; Consta, S. Characterization of "Star" Droplet Morphologies Induced by Charged Macromolecules. *J. Phys. Chem. A* **2016**, *120* (44), 8871–8880.

(23) Aliyari, E.; Konermann, L. Formation of Gaseous Proteins via the Ion Evaporation Model (IEM) in Electrospray Mass Spectrometry. *Anal. Chem.* **2020**, *92* (15), 10807–10814.

(24) Jurchen, J. C.; Williams, E. R. Origin of Asymmetric Charge Partitioning in the Dissociation of Gas-Phase Protein Homodimers. *J. Am. Chem. Soc.* **2003**, *125* (9), 2817–2826.

(25) Aquilina, J. A.; Benesch, J. L. P.; Bateman, O. A.; Slingsby, C.; Robinson, C. V. Polydispersity of a Mammalian Chaperone: Mass Spectrometry Reveals the Population of Oligomers in AB-Crystallin. *Proc. Natl. Acad. Sci. U. S. A.* **2003**, *100* (19), 10611–10616.

(26) Hogan, C. J.; Carroll, J. A.; Rohrs, H. W.; Biswas, P.; Gross, M. L. Combined Charged Residue-Field Emission Model of Macromolecular Electrospray Ionization. *Anal. Chem.* **2009**, *81* (1), 369–377.

(27) Hogan, C. J.; Biswas, P.; Chen, D. R. Charged Droplet Dynamics in the Submicrometer Size Range. *J. Phys. Chem. B* **2009**, *113* (4), 970–976.

(28) Susa, A. C.; Mortensen, D. N.; Williams, E. R. Effects of Cations on Protein and Peptide Charging in Electrospray Ionization from Aqueous Solutions. *J. Am. Soc. Mass Spectrom.* **2014**, *25* (6), 918–927.

(29) Xia, Z.; Degrandchamp, J. B.; Williams, E. R. Native Mass Spectrometry beyond Ammonium Acetate: Effects of Nonvolatile Salts on Protein Stability and Structure. *Analyst* **2019**, *144* (8), 2565–2573.

(30) Keifer, D. Z.; Motwani, T.; Teschke, C. M.; Jarrold, M. F. Measurement of the Accurate Mass of a 50 MDa Infectious Virus. *Rapid Commun. Mass Spectrom.* **2016**, *30* (17), 1957–1962.

(31) Draper, B. E.; Anthony, S. N.; Jarrold, M. F. The FUNPET—a New Hybrid Ion Funnel-Ion Carpet Atmospheric Pressure Interface for the Simultaneous Transmission of a Broad Mass Range. *J. Am. Soc. Mass Spectrom.* **2018**, *29* (11), 2160–2172.

(32) Elliott, A. G.; Merenbloom, S. I.; Chakrabarty, S.; Williams, E. R. Single Particle Analyzer of Mass: A Charge Detection Mass Spectrometer with a Multi-Detector Electrostatic Ion Trap. *Int. J. Mass Spectrom.* **2017**, *414*, 45–55.

(33) Elliott, A. G.; Harper, C. C.; Lin, H. W.; Williams, E. R. Mass, Mobility and MSN Measurements of Single Ions Using Charge Detection Mass Spectrometry. *Analyst* **2017**, *142* (15), 2760–2769.

(34) Doussineau, T.; Paletto, P.; Dugourd, P.; Antoine, R. Multiphoton Dissociation of Electrosprayed Megadalton-Sized DNA Ions in a Charge-Detection Mass Spectrometer. *J. Am. Soc. Mass Spectrom.* **2014**, *26* (1), 7–13.

(35) Barney, B. L.; Pratt, S. N.; Austin, D. E. Survivability of Bare, Individual Bacillus Subtilis Spores to High-Velocity Surface Impact: Implications for Microbial Transfer through Space. *Planet. Space Sci.* **2016**, *125*, 20–26.

(36) Adamson, B. D.; Miller, M. E. C.; Continetti, R. E. The Aerosol Impact Spectrometer: A Versatile Platform for Studying the Velocity Dependence of Nanoparticle-Surface Impact Phenomena. *EPJ Tech. Instrum.* **2017**, *4* (1), 1–17.

(37) Lössl, P.; Snijder, J.; Heck, A. J. R. Boundaries of Mass Resolution in Native Mass Spectrometry. *J. Am. Soc. Mass Spectrom.* **2014**, *25* (6), 906–917.

(38) Weiss, V. U.; Bereszczazk, J. Z.; Havlik, M.; Kallinger, P.; Gösler, I.; Kumar, M.; Blaas, D.; Marchetti-Deschmann, M.; Heck, A. J. R.; Szymanski, W. W.; Allmaier, G. Analysis of a Common Cold Virus and Its Subviral Particles by Gas-Phase Electrophoretic Mobility Molecular Analysis and Native Mass Spectrometry. *Anal. Chem.* **2015**, *87* (17), 8709–8717.

(39) Harper, C. C.; Elliott, A. G.; Lin, H. W.; Williams, E. R. Determining Energies and Cross Sections of Individual Ions Using Higher-Order Harmonics in Fourier Transform Charge Detection Mass Spectrometry (FT-CDMS). *J. Am. Soc. Mass Spectrom.* **2018**, *29* (9), 1861–1869.

(40) Harper, C. C.; Williams, E. R. Enhanced Multiplexing in Fourier Transform Charge Detection Mass Spectrometry by Decoupling Ion Frequency from Mass to Charge Ratio. *J. Am. Soc. Mass Spectrom.* **2019**, *30* (12), 2637–2645.

(41) Harper, C. C.; Elliott, A. G.; Oltrogge, L. M.; Savage, D. F.; Williams, E. R. Multiplexed Charge Detection Mass Spectrometry for High-Throughput Single Ion Analysis of Large Molecules. *Anal. Chem.* **2019**, *91* (11), 7458–7468.

(42) Brauer, D. D.; Hartman, E. C.; Bader, D. L. V.; Merz, Z. N.; Tullman-Ercek, D.; Francis, M. B. Systematic Engineering of a Protein Nanocage for High-Yield, Site-Specific Modification. *J. Am. Chem. Soc.* **2019**, *141* (9), 3875–3884.

(43) Elliott, A. G.; Harper, C. C.; Lin, H. W.; Williams, E. R. Effects of Individual Ion Energies on Charge Measurements in Fourier Transform Charge Detection Mass Spectrometry (FT-CDMS). *J. Am. Soc. Mass Spectrom.* **2019**, *30* (6), 946–955.

(44) Howder, C. R.; Long, B. A.; Gerlich, D.; Alley, R. N.; Anderson, S. L. Single Nanoparticle Mass Spectrometry as a High Temperature Kinetics Tool: Sublimation, Oxidation, and Emission Spectra of Hot Carbon Nanoparticles. *J. Phys. Chem. A* **2015**, *119* (50), 12538–

12550.

(45) Bruce, J. E.; Cheng, X.; Bakhtiar, R.; Wu, Q.; Hofstadler, S. A.; Anderson, G. A.; Smith, R. D. Trapping, Detection, and Mass Measurement of Individual Ions in a Fourier Transform Ion Cyclotron Resonance Mass Spectrometer. *J. Am. Chem. Soc.* **1994**, *116* (17), 7839–7847.

(46) Keifer, D. Z.; Alexander, A. W.; Jarrold, M. F. Spontaneous Mass and Charge Losses from Single Multi-Megadalton Ions Studied by Charge Detection Mass Spectrometry. *J. Am. Soc. Mass Spectrom.* **2017**, *28* (3), 498–506.

(47) Fawcett, W. R. Thermodynamic Parameters for the Solvation of Monatomic Ions in Water. *J. Phys. Chem. B* **1999**, *103* (50), 11181–11185.

(48) Asensio, M. A.; Morella, N. M.; Jakobson, C. M.; Hartman, E. C.; Glasgow, J. E.; Sankaran, B.; Zwart, P. H.; Tullman-Ercek, D. A Selection for Assembly Reveals That a Single Amino Acid Mutant of the Bacteriophage MS2 Coat Protein Forms a Smaller Virus-like Particle. *Nano Lett.* **2016**, *16* (9), 5944–5950.

(49) Chowdhury, S. K.; Katta, V.; Chait, B. T. Probing Conformational Changes in Proteins by Mass Spectrometry. *J. Am. Chem. Soc.* **1990**, *112* (24), 9012–9013.

(50) Putnam, C. D.; Hammel, M.; Hura, G. L.; Tainer, J. A. X-Ray Solution Scattering (SAXS) Combined with Crystallography and Computation: Defining Accurate Macromolecular Structures, Conformations and Assemblies in Solution. *Quarterly Reviews of Biophysics*. Cambridge University Press August 2007, pp 191–285.

(51) Fischer, H.; Polikarpov, I.; Craievich, A. F. Average Protein Density Is a Molecular-Weight-Dependent Function. *Protein Sci.* **2009**, *13* (10), 2825–2828.

(52) Schildkraut, C. L.; Marmur, J.; Doty, P. Determination of the Base Composition of Deoxyribonucleic Acid from Its Buoyant Density in CsCl. *J. Mol. Biol.* **1962**, *4* (6), 430–443.

(53) Leney, A. C.; Heck, A. J. R. Native Mass Spectrometry: What Is in the Name? *J. Am. Soc. Mass Spectrom.* **2017**, *28* (1), 5–13.

(54) Hogan, C. J.; Ruotolo, B. T.; Robinson, C. V.; Fernandez De La Mora, J. Tandem Differential Mobility Analysis-Mass Spectrometry Reveals Partial Gas-Phase Collapse of the GroEL Complex. *J. Phys. Chem. B* **2011**, *115* (13), 3614–3621.

(55) Breuker, K.; McLafferty, F. W. Stepwise Evolution of Protein Native Structure with Electrospray into the Gas Phase, 10-12 to 102 S. *Proceedings of the National Academy of Sciences of the United States of America*. National Academy of Sciences November 25, 2008, pp 18145–18152.

(56) Rolland, A. D.; Prell, J. S. Computational Insights into Compaction of Gas-Phase Protein and Protein Complex Ions in Native Ion Mobility-Mass Spectrometry. *TrAC - Trends Anal. Chem.* **2019**, *116*, 282–291.

(57) Steinberg, M. Z.; Breuker, K.; Elber, R.; Gerber, R. B. The Dynamics of Water Evaporation from Partially Solvated Cytochrome c in the Gas Phase. *Phys. Chem. Chem. Phys.* **2007**, *9*

(33), 4690–4697.

(58) McKay, A. R.; Ruotolo, B. T.; Ilag, L. L.; Robinson, C. V. Mass Measurements of Increased Accuracy Resolve Heterogeneous Populations of Intact Ribosomes. *J. Am. Chem. Soc.* **2006**, *128* (35), 11433–11442.

5.8 Table and Figures

Table 5.1. Physical Properties of Nanodrops Originating from Solutions Containing Different Solutes

	Pure H_20	AA	LiCl (all)	LiCl ("dry")	LiCl ("wet")	NaCl (all)	NaCl ("dry")	NaCl ("wet")	KCl	CsCl
Ion Count	3523	5861	4322	3181	1141	5616	2597	3019	8255	3078
Avg. Mass (kDa)	5118	3992	3106	3009	3378	3343	2890	3733	2006	1352
Avg. Mass Loss (kDa)	319	189	30	18	68	71	18	145	9	5
Avg. Charge	207.0	152.8	129.5	121.2	152.5	132	101.5	158.2	73.9	51.3
Avg. % of Rayleigh Charge	118 %	99%	96%	92%	106%	94%	78%	106%	69%	56%
Ion Emission Rate (events/ion)	0.228	0.189	0.527	0.475	0.708	0.305	0.365	0.277	0.006	0.009

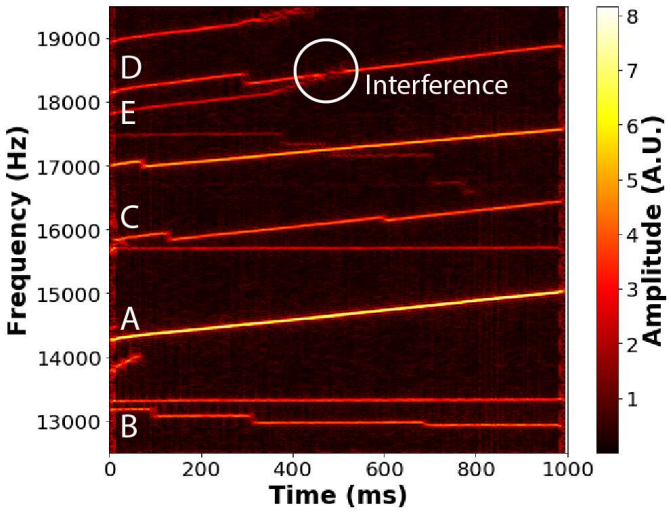


Figure 5.1. Short-time Fourier transform of a 1 s trapping event with 11 ions generated from a 20 mM NaCl solution. Seven ions are trapped for the entire 1 s trapping time. Increases in ion frequency, e.g., for ions labeled **A**, **C**, **D**, and **E,** correspond to decreasing ion energies, primarily as a result of water evaporation from the ions. Discrete, negative changes in frequency observed for ions **B**, **C**, and **D** correspond to charge losses. Any ion frequencies that overlap during the trapping period, such as ions **D** and **E**, are discarded from the analysis as inaccurate/indistinguishable amplitudes (white circle) occur as a result of interference.

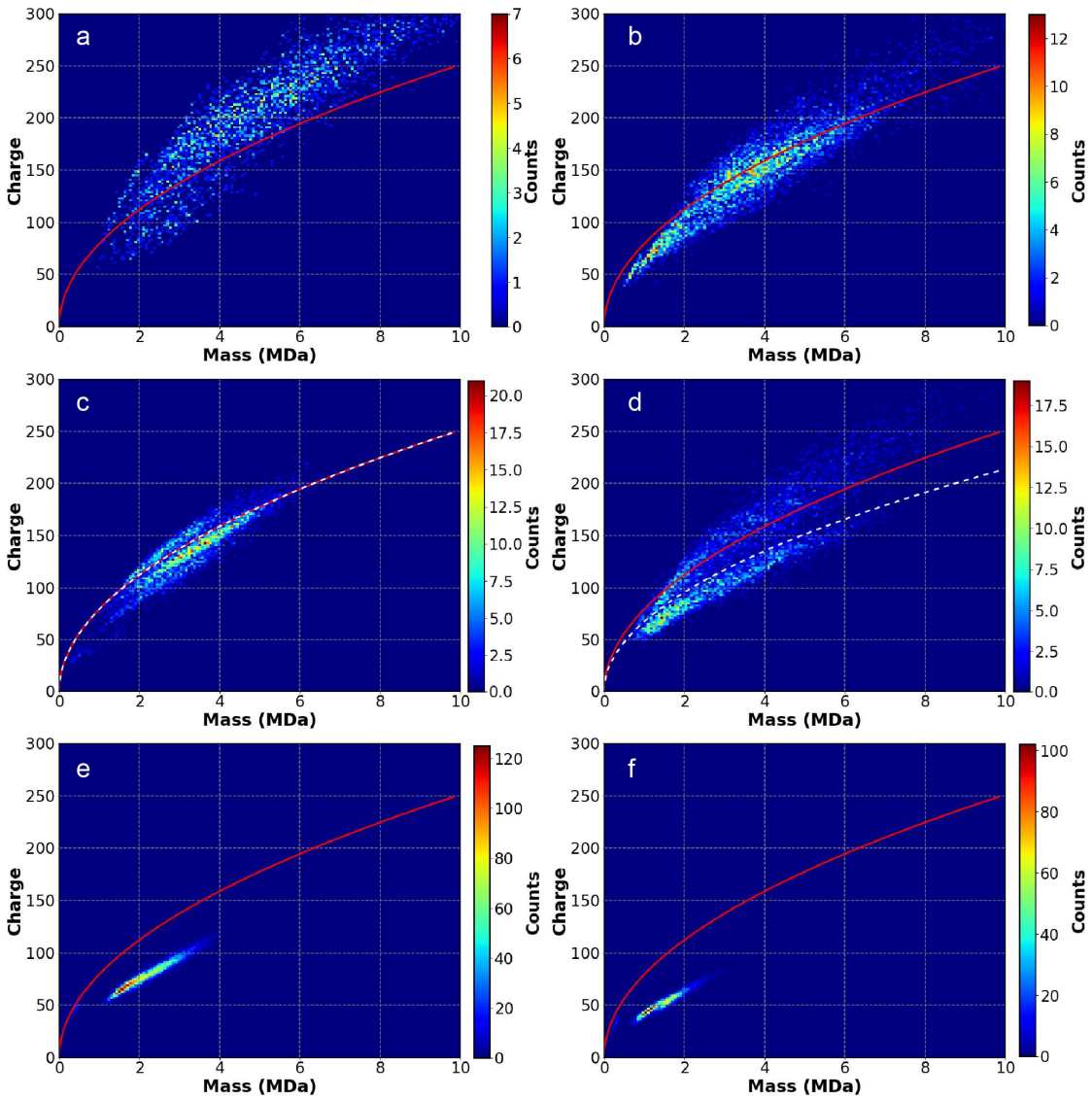


Figure 5.2. Two-dimensional mass vs. charge histograms for ions originating from (a) pure water, (b) AA, (c) LiCl, (d) NaCl, (e) KCl and (f) CsCl. Red lines indicate the Rayleigh limit charge as function of mass calculated for water with a density of 0.998 g/mL. White dotted lines in the LiCl and NaCl data distinguish "wet", higher charge distributions of ions from "dry", lower charge distributions. Higher mass "wet" ions present in (a), (b), (c) and (d) have higher charge relative to the Rayleigh limit than lower mass "wet" ions, suggesting a progression toward a "dry" state at lower mass. "Dry" ions, observed in (c), (d), (e), and (f), have charges below the Rayleigh limit that decrease as a function of increasing alkali metal cation size.

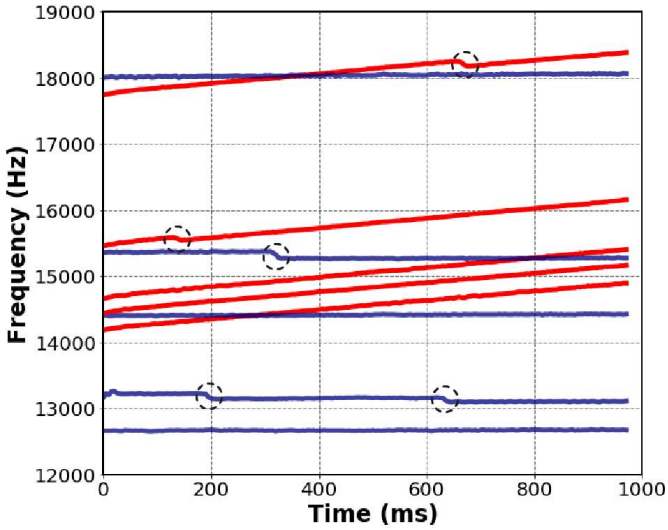


Figure 5.3. Ion frequency vs. trap time for five "dry" (blue) and five "wet" (red) individual ions randomly selected from the two distributions observed in NaCl solution data of Figure 2D. Ion emission events (black circles) occur with both "dry" and "wet" ions. The frequencies of "wet" ions increase significantly, primarily as a result of neutral mass losses of 100's of kDa. The frequency increase of "dry" ions occurs less rapidly.

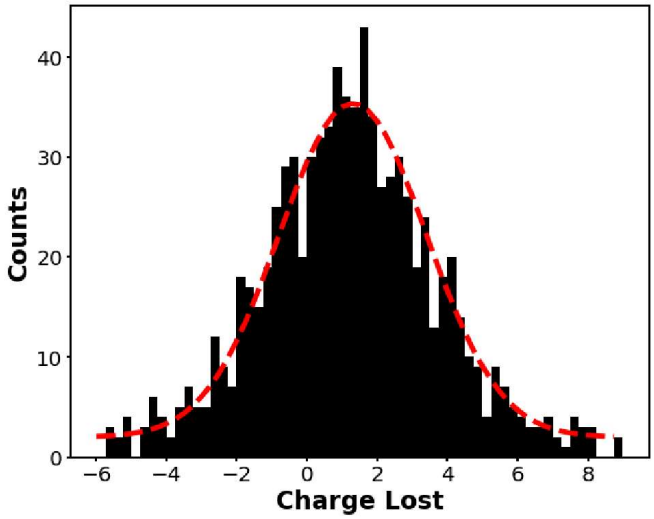


Figure 5.4. Histogram of the number of charges lost at each ion emission event for individual ions generated from a 20 mM NaCl solution. The charge loss distribution is fit by a Gaussian curve (red dotted line) centered at 1.1 e with standard error of 0.07 e. The Gaussian fit indicates that the width of the distribution is primarily a consequence of measurement uncertainty rather than losses of multiple charges.

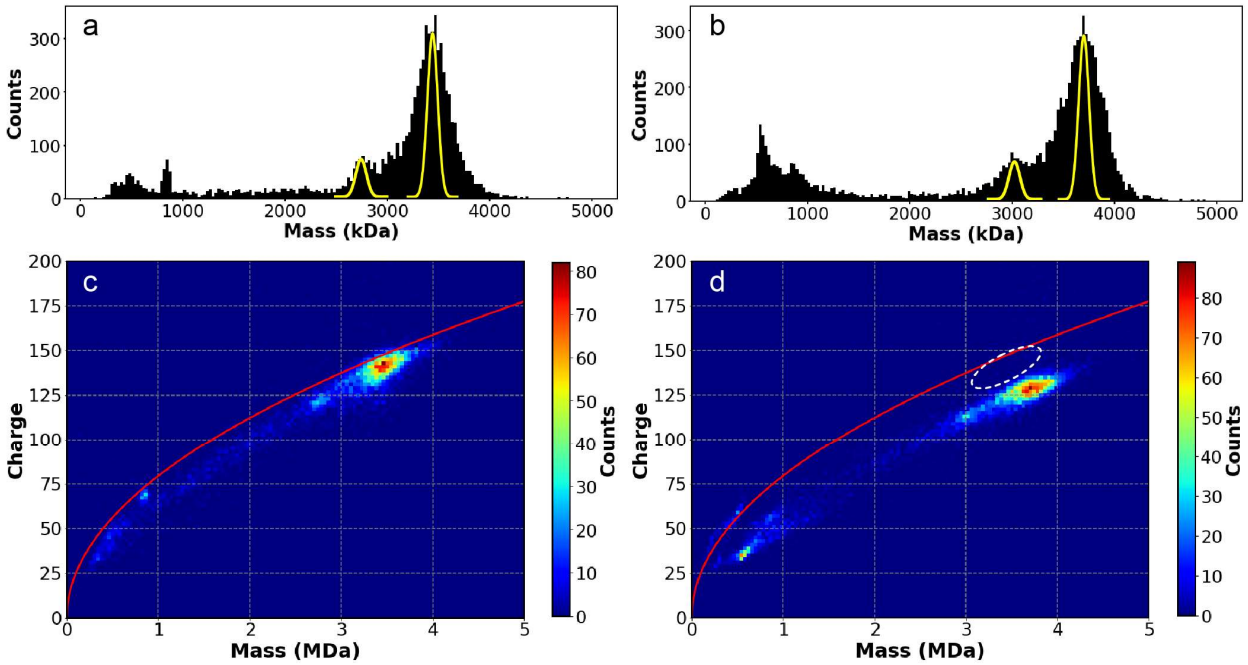


Figure 5.5. Mass histograms for MS2 capsid ions formed by electrospray from (a) ammonium acetate and (b) NaX solutions. The yellow peaks correspond to the instrinsic linewidth; the broad peak widths observed indicate significant sample heterogeneity due to encapsulation and salt adduction, especially from the NaX solution. Two-dimensional mass vs. charge histograms for MS2 capsid from (c) AA and (d) NaX show that ions formed from the latter solution are ~250 kDa higher in mass due to salt adduction, but are charged less (~13 *e*) despite their higher mass (for comparison purposes, the white dotted oval in (d) indicates AA ion distribution).

5.9 Supporting Information

5.9.1 Experimental Details: Charge Detection Mass Spectrometry

Ions are introduced into the CDMS instrument through a modified Waters Z-Spray source (Waters Corporation, Milford, MA) and enter a region containing two RF-only quadrupole ion guides (Ardara Technologies, Ardara, PA) at a pressure of ~1×10^{-3} Torr. The DC potential of the first guide is ~10 V higher than that of the second guide. Ions with *m*/*z* below ~10,000 are lost in this stage due to the low mass cut-off of the RF quadrupole ion guides operating at 555 kHz. A lens at the exit of the ion guides with a potential ~80 V higher than that of the second ion guide is used to accumulate ions for up to 1 s. The voltage on this lens is pulsed down by 110 V for 1 ms, which introduces a pulse of ions into a turning quadrupole (Ardara Technologies, Ardara, PA) that directs the ions into the high vacuum chamber containing an electrostatic cone trap and detector tube. The pressure in the final chamber was ~4×10^{-9} Torr. The potential of the entrance cone electrode is lowered to 0.0 V for 1 ms with a 500 μs delay relative to the release of the ions from the RF quadrupole to allow for ions to transit from the RF trap into the electrostatic ion trap. The potential is then raised to match the end cone (330 V) for the duration of the 1 s trapping event. Ions in the electrostatic ion trap induce a charge pulse each time they traverse the detector tube. Individual ion masses, charges, and energies are determined at each 5 ms increment from the measured oscillation frequencies and amplitudes of the fundamental and second harmonic frequencies as they evolve throughout the 1 s trapping period. The broad distribution of ion mass and charge in these experiments makes it possible to simultaneously analyze up to ~40 individual ions in each trapping event because the frequency distribution of the ions is broad (up to 10 kHz) and their signals are less likely to interfere with each other. Ion energies are centered around 211 eV/z with a standard deviation of 5 eV/z. The induced charge signal is amplified by a CoolFET charge-sensitive preamplifier (Amptek) and home-built linear voltage and current amplifier. The signal is digitized and analyzed with a Python program using short-time Fourier transforms (STFT) and a peak-picking algorithm. Interfering ion signals and ion signals that do not persist for the entire 1 s trapping period are discarded.

5.9.2 Charge and Mass Lost after Ion Emission Events

Figures S5.1–S5.7 show charge and mass loss histograms as a result of ion emission events for nanodrops originating from pure water (S5.1-S5.2), ammonium acetate (S5.3–S5.4), LiCl (S5.5–S5.6), and NaCL (S5.7, mass loss only). In general, Gaussian fits of charge losses are centered near 1 *e* and fits of mass losses are centered near 0 Da within measurement error. These data are consistent with the loss of a singly charged ion that is minimally solvated.

5.9.3 Experimental Details: Small Angle X-ray Scattering (SAXS)

MS2 capsid samples were prepared in triplicate at a range of concentrations between 50 uM and 6.7 uM in 100 mM ammonium acetate at pH 7.2 or 10 mM sodium phosphate buffer at pH 7.2 with 100 mM NaCl. Samples were analyzed by high-throughput small angle X-ray scattering (HT-SAXS) at the SIBYLS beamline at the Advanced Light Source in Berkeley CA. Samples were exposed with a 10^{11} photon/s, 12 keV monochromatic beam in a series of exposures: 0.5, 1.0, 2.0, and 4.0 s. Background subtraction was performed using measurements of buffer-only samples. Data were first analyzed using the SAXS FrameSlice web app and then imported into the ScÅtter and SASview applications for further size and shape analysis. Data were fit to a

polydisperse core-shell sphere model using a fixed protein shell scattering length density as described in previous MS2 SAXS measurements.[1]

5.9.4 Experimental Details: Dynamic Light Scattering (DLS)

DLS measurement was performed on a Malvern Instruments Zetasizer Nano ZS. MS2 capsid samples were prepared at a protein concentration of 10 uM in each respective buffer and passed through a 0.2 μM spin filter prior to each run. Size determination was performed in triplicate at 25 ºC following a 2-min temperature equilibration.

5.9.5 Correlation of Nanodrop Mass and Solute Identity

A notable result from these nanodrop experiments is that the average mass of the nanodrops generally correlates with the solvation energies of the charge carriers in solutions. Electrospray conditions were held approximately constant between solutions, so it is unlikely that the large mass differences observed are the merely the result of electrospray variations. While this correlation is still under investigation, these data suggest that less solvated charge carriers may promote the formation of either smaller Rayleigh fission progeny droplets or accelerate the droplet evaporation process by some other means. Early stage differences in droplet evaporation may also amplify the observed differences in nanodrop size, as the increased ratio of surface area to volume of smaller droplets, among other factors, is conducive to faster evaporation rates.

5.9.6 Supporting Reference

(1) Kuzmanovic, D. A.; Elashvili, I.; O'Connell, C.; Krueger, S. A Novel Application of Small-Angle Scattering Techniques: Quality Assurance Testing of Virus Quantification Technology. *Radiat. Phys. Chem.* **2008**, *77* (3), 215–224.

5.10 Supporting Figures

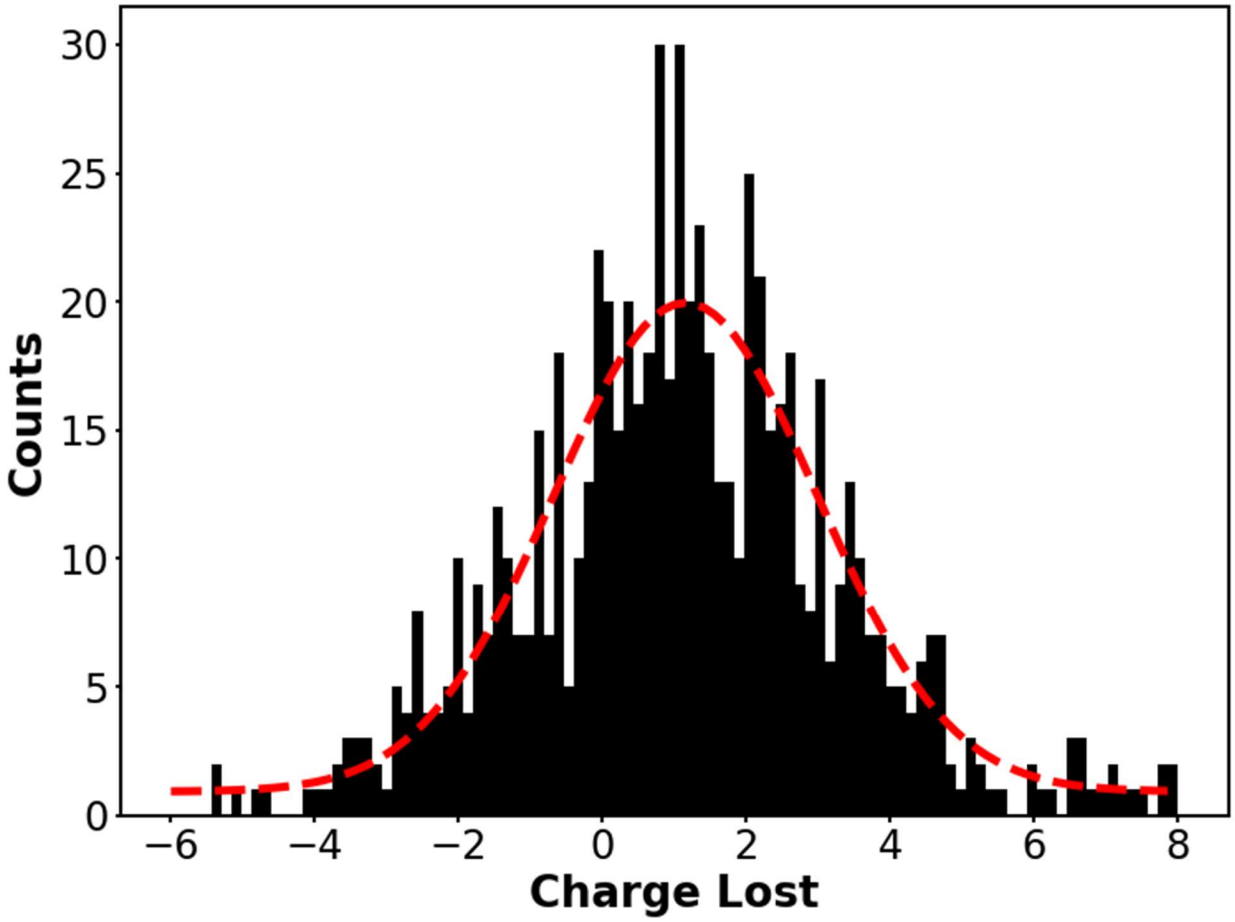


Figure S5.1. Histogram of the number of charges lost at each ion emission event for individual ions generated from pure water. The charge loss distribution is fit by a Gaussian curve (red dotted line) centered at 1.01 *e* with standard error of 0.07 *e*.

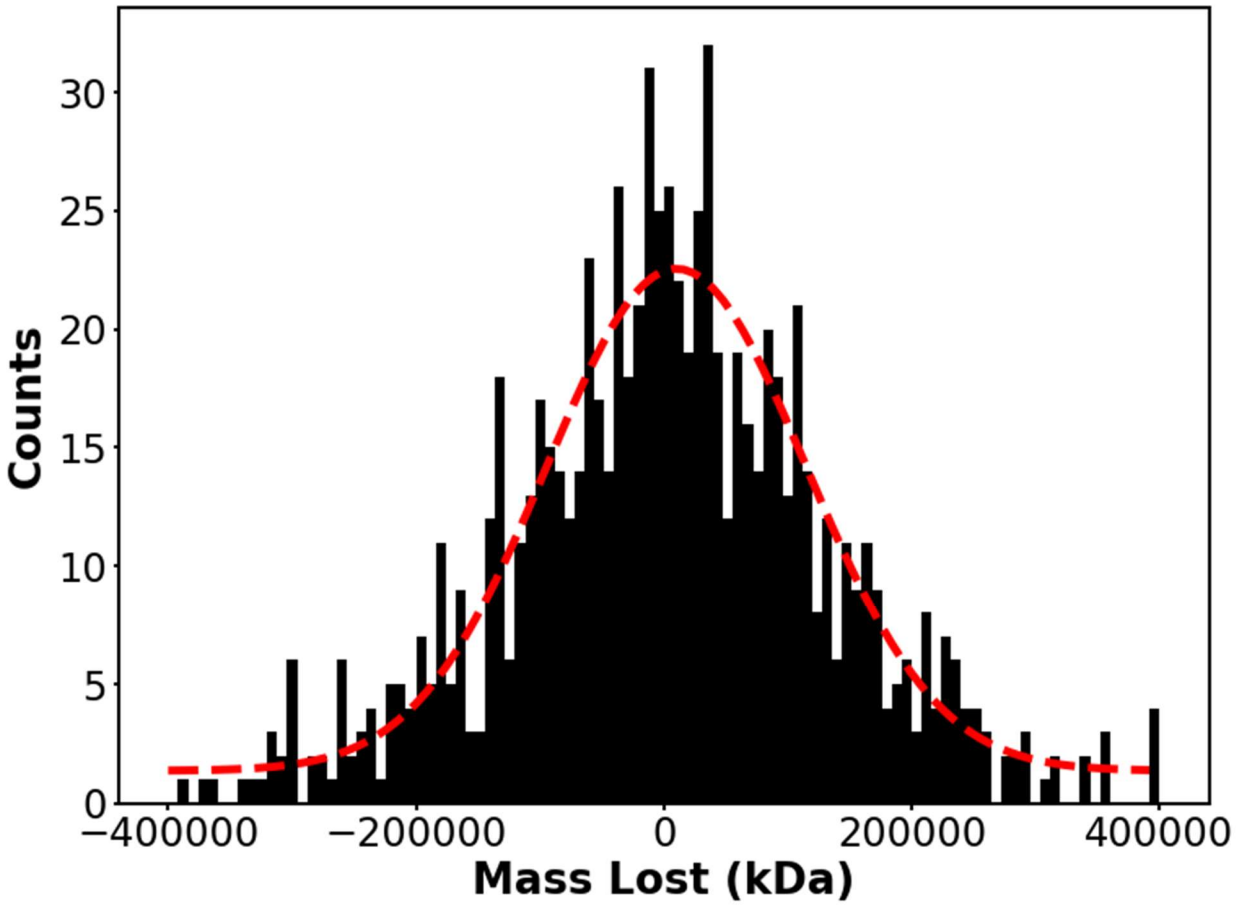


Figure S5.2. Histogram of the mass lost at each ion emission event for individual ions generated from pure water. The mass loss distribution is fit by a Gaussian curve (red dotted line) centered at 2,000 Da with standard error of 4,000 Da.

.

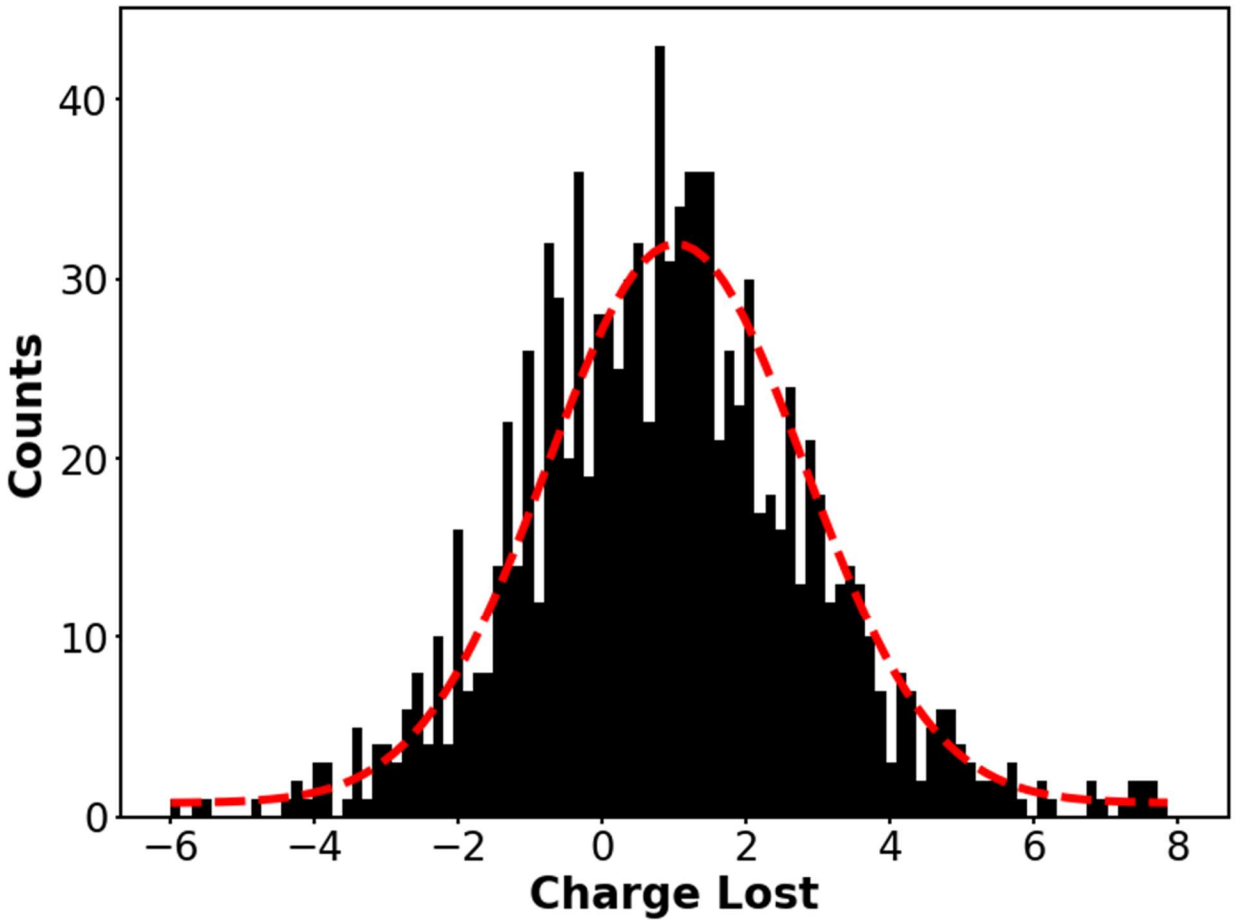


Figure S5.3. Histogram of the number of charges lost at each ion emission event for individual ions generated from 20 mM ammonium acetate. The charge loss distribution is fit by a Gaussian curve (red dotted line) centered at 1.03 *e* with standard error of 0.05 *e*.

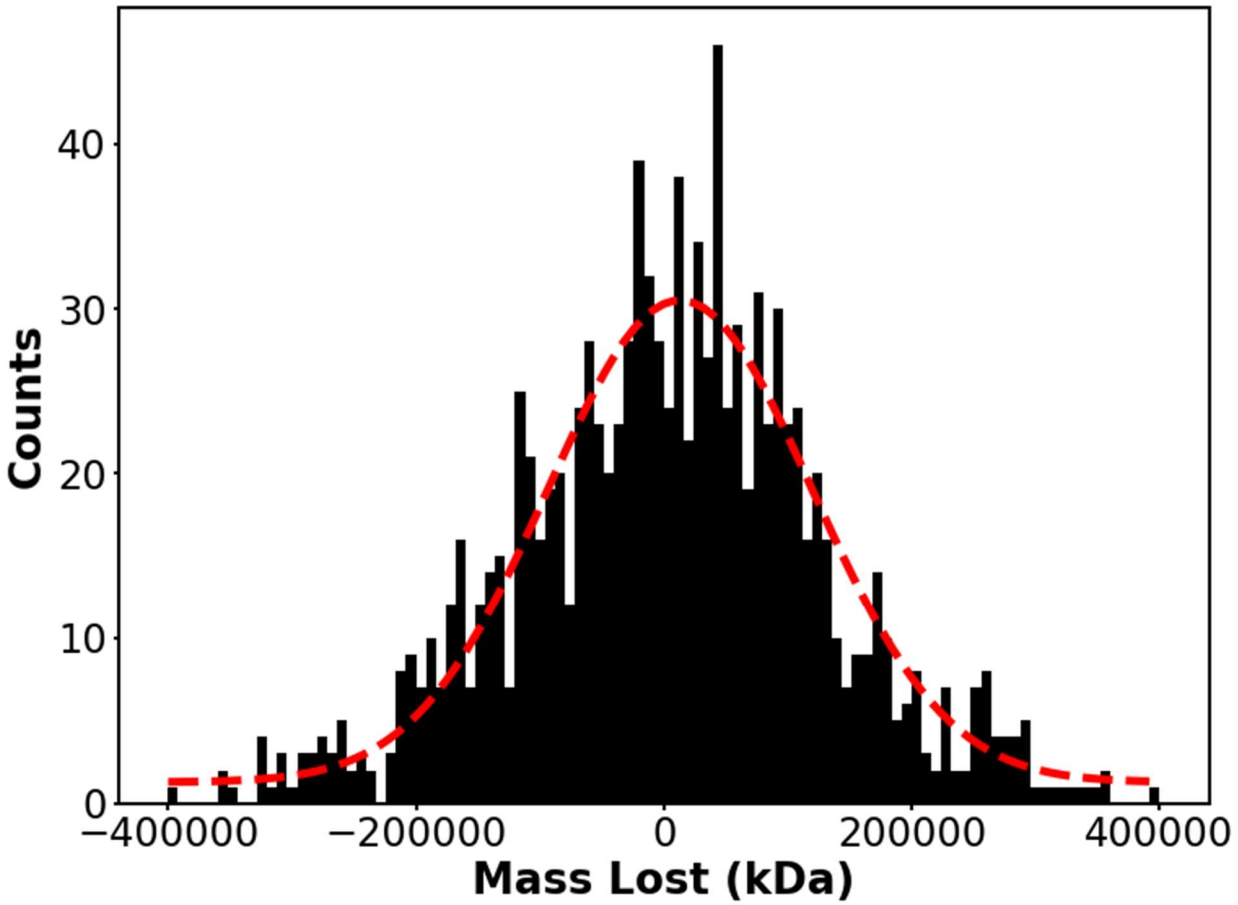


Figure S5.4. Histogram of the mass lost at each ion emission event for individual ions generated from 20 mM ammonium acetate. The mass loss distribution is fit by a Gaussian curve (red dotted line) centered at 4,000 Da with standard error of 3,000 Da.

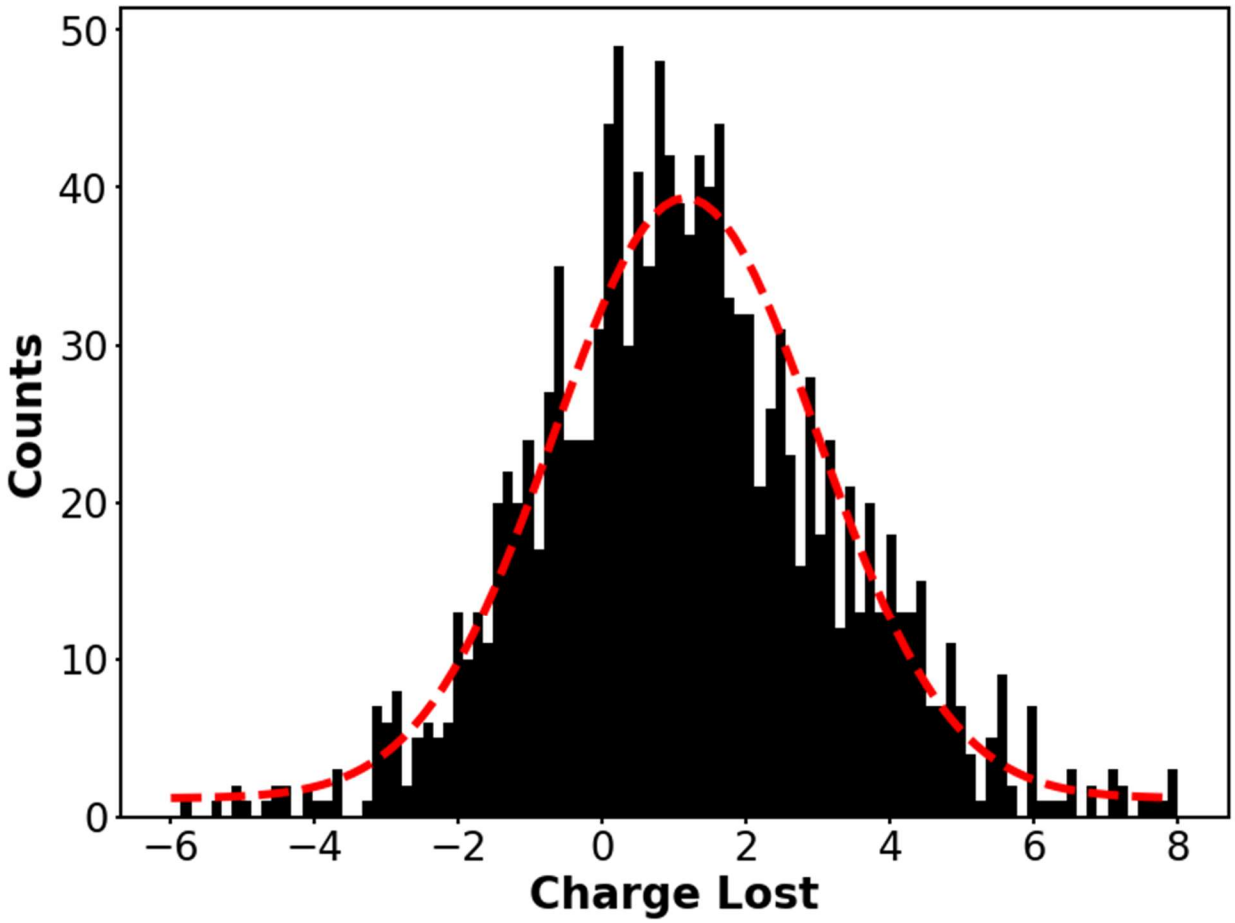


Figure S5.5. Histogram of the number of charges lost at each ion emission event for individual ions generated from 20 mM LiCl. The charge loss distribution is fit by a Gaussian curve (red dotted line) centered at 0.97 *e* with standard error of 0.05 *e*.

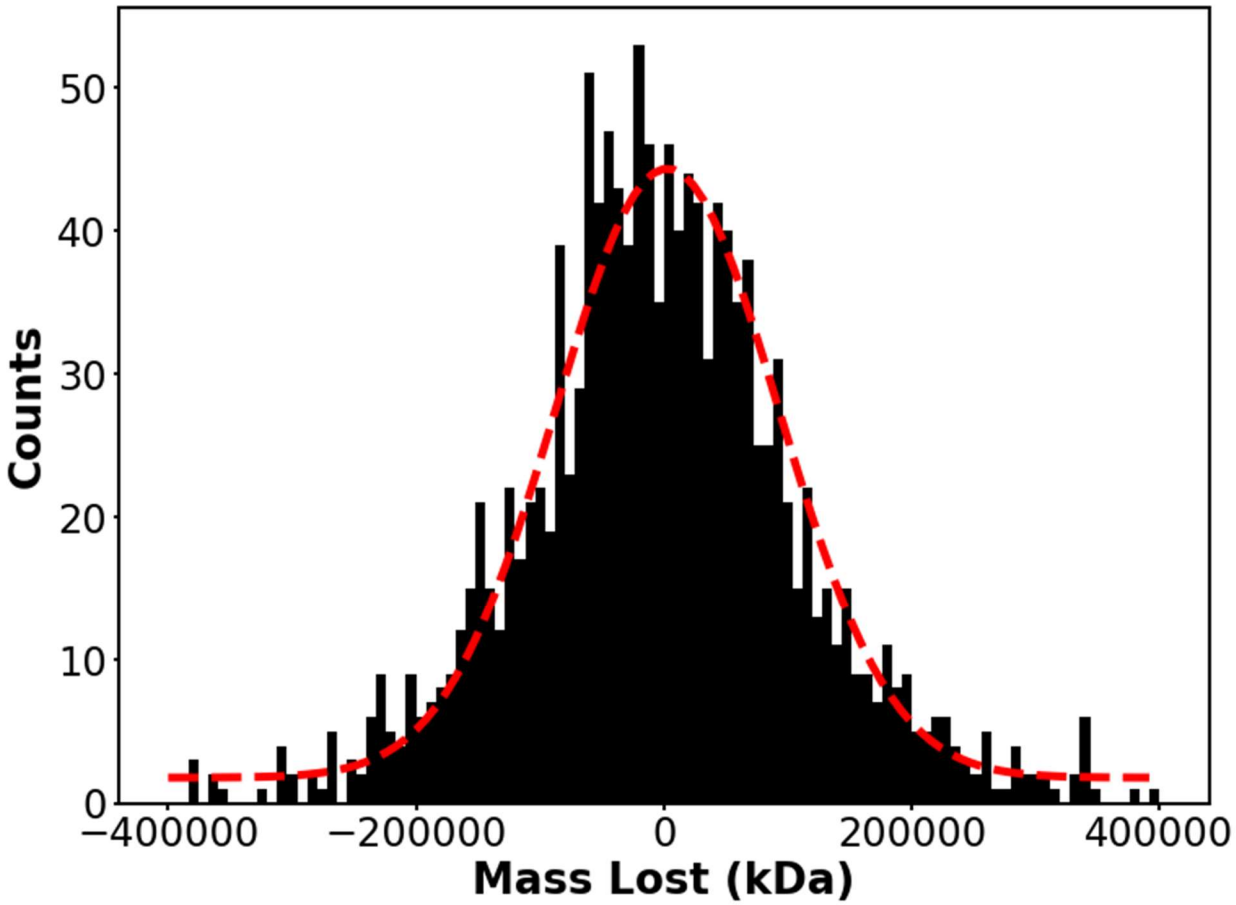


Figure S5.6. Histogram of the mass lost at each ion emission event for individual ions generated from 20 mM LiCl. The mass loss distribution is fit by a Gaussian curve (red dotted line) centered at 0 Da with standard error of 2,000 Da.

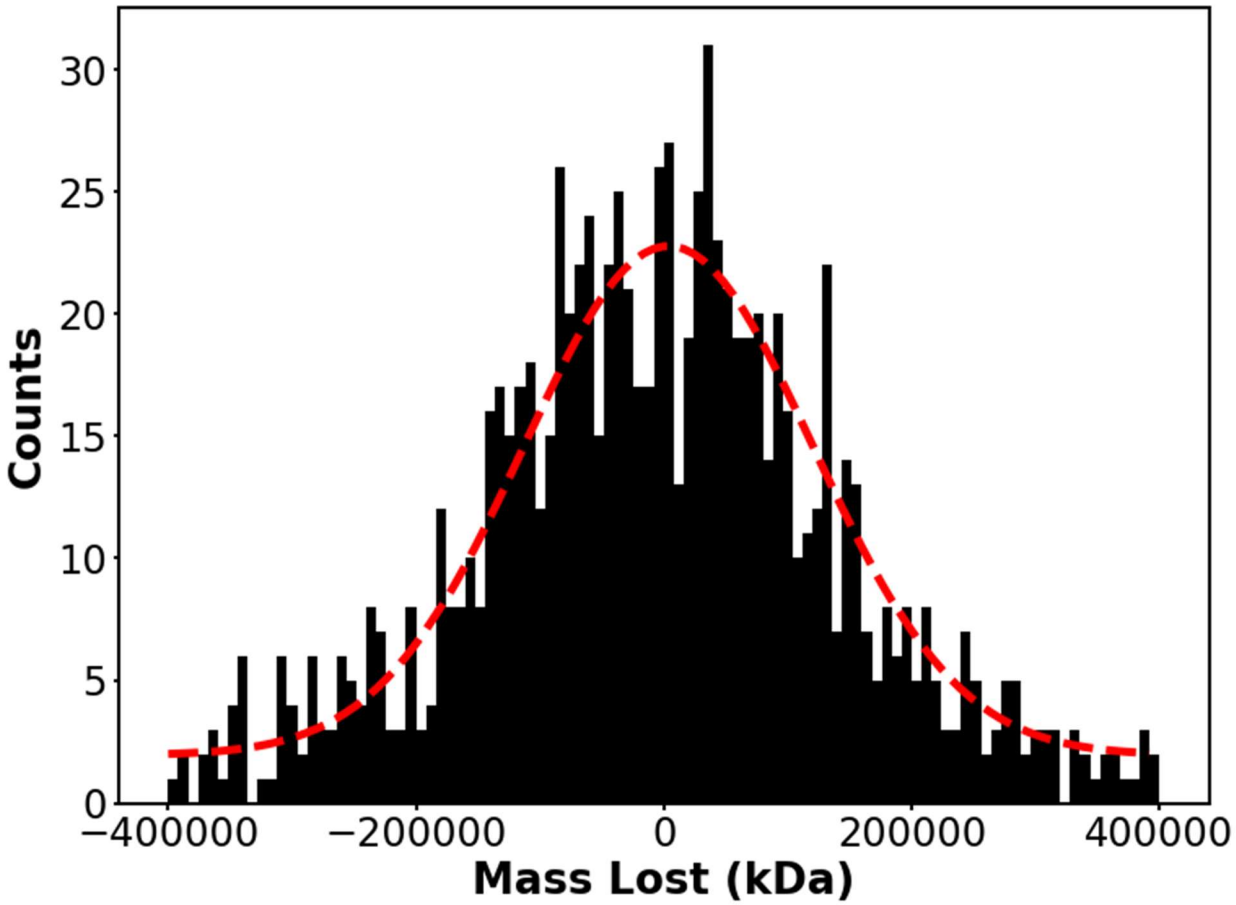


Figure S5.7. Histogram of the mass lost at each ion emission event for individual ions generated from 20 mM NaCl. The mass loss distribution is fit by a Gaussian curve (red dotted line) centered at 1,000 Da with standard error of 4,000 Da.

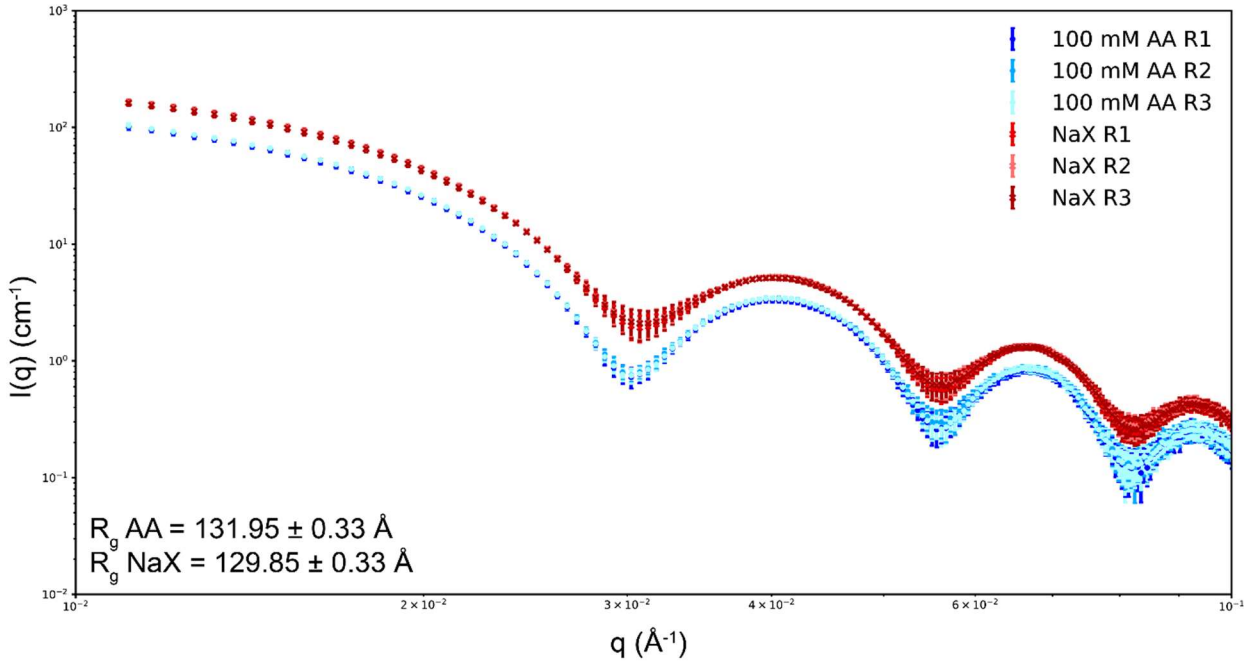


Figure S5.8. Intensity vs q profile of MS2 capsids from SAXS in AA (100 mM ammonium acetate) or NaX (10 mM sodium phosphate + 100 mM NaCl) buffer. The mean radius of gyration (R_g) was determined by fit to a core-shell sphere model and reported as the sum of the core and protein shell radii.

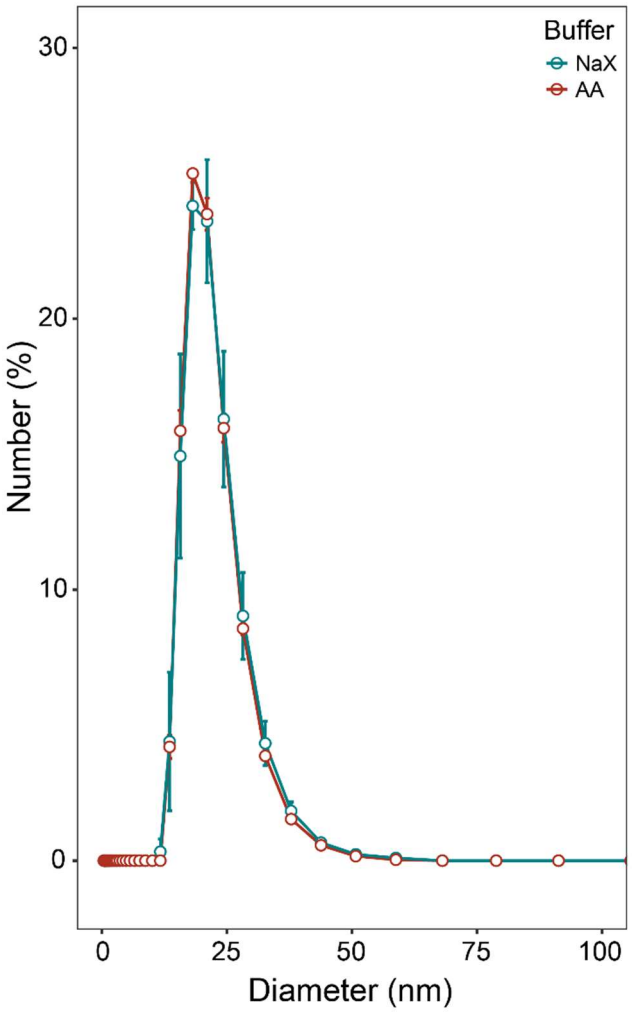


Figure S5.9. MS2 capsid diameter in NaX or AA buffer as determined by DLS. Size distribution is reported as percent number of particles. Error bars represent the standard deviation of three replicate measurements.

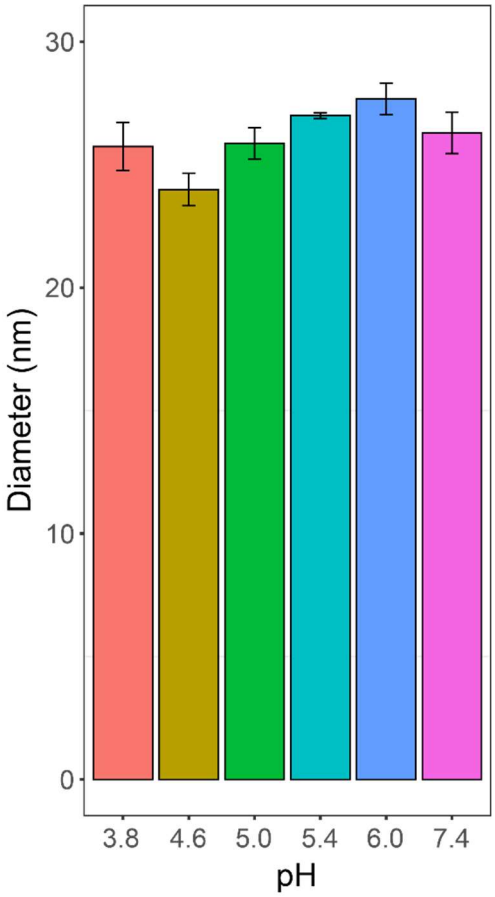


Figure S5.10. Effect of pH on MS2 capsid diameter as determined by DLS. Samples were prepared in 10 mM sodium phosphate buffer with 100 mM NaCl at the indicated pH. Error bars represent the standard deviation of three replicate measurements.

Chapter 6

Conclusions and Future Directions

6.1 Conclusions

The work in this dissertation contributes a set of new data analysis and measurement techniques that further enable CDMS as a tool for analyzing high mass, highly heterogeneous samples. Chapter 2 describes a novel method for the dynamic, *in situ* measurement of ion energies along with the standard measurements of *m*/*z* and charge. This extra dimension of analysis further differentiates ions in a sample and makes it possible to extract additional information about molecular structures, such as collision cross sections, and also enables MS^n studies of evaporative mass losses (Chapters 2 and 5) and fragmentation events (Chapters 3 and 5). This *in situ* measurement method also has meaningful implications in CDMS instrument design. Typical CDMS analyzers use energy selective optics to admit ions with a narrow range of energies to the detector and use the centerline energy as a constant in the *m*/*z* calculation. This is done to minimize the intrinsic dependence of the mass measurement on ion energy. However, using energy selective optics comes at a cost of decreased ion transmission, increased instrument complexity and size, and increased expense. The method of Chapter 2 largely eliminates the necessity for such optics because the energy of each ion is determined directly without assumptions.

Chapters 3 and 4 demonstrate and discuss a multiplexing method for simultaneously trapping and analyzing multiple ions. The multiplexing technique presented in Chapter 3, where multiple ions are simultaneously trapped and measured, decreases acquisition time in trapping CDMS without sacrificing mass measurement accuracy. An order of magnitude improvement in analysis speed is demonstrated without measurable detriment to the mass measurement. Simulations of trapped ion CDMS in Chapter 4 show that this improvement in analysis speed can be increased an additional order of magnitude via a novel *m*/*z* and frequency decoupling scheme. In multiplexed trapping CDMS, ions with the same or similar oscillation frequencies interfere and neither can be accurately measured. However, because ion energy can be measured *in situ* (Chapter 2), ion of varying energies can be admitted to the ion trap. Differences in ion energy result in different oscillation frequencies, even if ions have the same *m*/*z*. This decoupling of *m*/*z* from oscillation frequency makes it possible to use variable ion energies to spread ion signal across a broader range of frequencies and decrease instances of interference that reduce the number of measurable ions in a single trapping event.

Chapter 5 is an application of the techniques developed in Chapters 2 and 3 to understanding the mechanism by which charged macromolecules are formed using electrospray ionization (ESI). Small charged nanodrops (10 – 100s of nm in diameter) are too small to image using optical techniques, but are still far too large and heterogeneous for measurement by conventional MS. Moreover, solvent evaporation from these charged nanodrops result in constantly changing ion mass and energy. Ion emission from the surface of the nanodroplets also result in discrete charge loss events. However, because all these quantities are dynamically tracked (Chapter 2), the evaporative mass loss and charge lost to ion emission can be measured. Chapter 5 quantifies the

extent of evaporative mass loss and frequency of ion emission from solutions containing different solute. Solute ions with lower solvation energies yield nanodrops with decreasingly less charge compared to the charge predicted by the Rayleigh equation, perhaps due to more kinetically favorable ion emission of these solute ions. MS2 capsid ions analyzed from differing solutions show a similar, solute dependent trend in charging, indicating that solute identity can significantly affect charging in native MS of large macromolecules. The MS2 capsid charging also indicates that the hollow capsid structure of MS2 collapses significantly prior to its transition into the gas phase, contrary to the gas-phase collapse observed by others.

6.2 Future Directions and Applications of CDMS

Charge detection mass spectrometry (CDMS) is a rapidly evolving technique in mass spectrometry. A key aspect that differentiates CDMS from conventional MS techniques is that CDMS independently measures each individual ion's *m*/*z* and charge, rather than only the *m*/*z* of an ensemble of ions. Making measurements of both ion *m*/*z* and charge on an ion-by-ion basis makes it possible to directly calculate the mass of each individual ion. The individual ion mass measurements of CDMS immunize the technique from the challenges inherent to ensemble measurements of heterogeneous samples. Because analyte heterogeneity naturally increases with mass,[1] CDMS is well-suited to the measurement of large macromolecules. Furthermore, macromolecules are typically ionized using electrospray ionization (ESI), a technique that yields increasingly charged analytes as mass and size increase.[1] The sensitivity and accuracy of CDMS measurements improve with increasing charge, as opposed to ensemble techniques where identifying and resolving high charge states is increasingly difficult.[1–3] These advantages give CDMS an unprecedented mass range compared to conventional MS, as illustrated in Figure 6.1. CDMS has also largely closed the gap between MS techniques and macroscopic mass measurement techniques such as surface acoustic wave (SAW) balances.[4,5] Compared to the current state of other individual ion techniques, the combination of relatively simple instrumentation, high mass and charge accuracy, and shorter time required to analyze a sample make CDMS the premier technique in the single ion mass spectrometry of MDa-sized macromolecules.

6.2.1 The Need for Speed

Historically, single ion mass spectrometry has been limited in its applications due to very low measurement throughput, i.e., it takes a very long time measure each ion. Single pass CDMS overcomes this limitation, but at the cost of greater mass uncertainty. Single ion only CDMS requires longer acquisition times (30+ min) to acquire enough individual ion data to provide a meaningful mass spectrum.[6] Limiting CDMS to one ion at a time is proposed to eliminate ion frequency shifts resulting from ion-ion interactions which can result in greater uncertainty in the ion mass determination.[6,7] Simulations of ion trajectories provide some evidence for these frequency shifts, but no published experimental results have verified this phenomenon.[7] In either case, pursuing a high-resolution single ion approach is mostly unnecessary in native MS because the heterogeneity of large analytes, not the maximum instrumental resolution, ultimately limits the achievable mass resolution. For example, Lössl et al. note that for a very well purified 18 MDa virus capsid (~52,000 *m*/*z*) measured using a time-of-flight instrument, a *m*/*z* resolution of only 200 could be achieved, even though experiments measuring CsI clusters have shown that an instrumental resolution of several thousand is possible in a similar *m*/*z* range.[1] Mass resolution and

m/*z* resolution are equal insofar as the charge can be unambiguously determined either by deconvolution of resolved charge states (achieved Lössl et al. in the example above) or by direct measurement (achieved in CDMS[8]).

While a mass resolution of 200+ has not yet been achieved in the instrument used for the multiplexed CDMS presented in Chapters 3 and 4, the recently improved detection electronics and internal charge calibration standard used in a different, single ion only CDMS instrument have made it possible to achieve a mass resolution of ~330.[9] Given that no effects on instrument resolution were observed as a function of the number of trapped ions in Chapter 3, multiplexed CDMS including these improvements should also benefit in increased resolution even if performance is slightly affected by ion-ion interactions. Rather than maximizing unusable mass resolution, increasing measurement speed is a more practical pursuit in advancing CDMS technology. Faster analysis times are required for CDMS to be practical for commercial applications. The multiplexing methods demonstrated in Chapters 3 are the most straightforward way to achieve the needed gains in analysis speed without sacrificing the accuracy of the mass and charge measurements. The analysis in Chapter 4 indicates that decreasing CDMS acquisition times to less than one minute is eminently reasonable using these methods, especially with optimized instrumentation.

6.2.2 Advantage of Dynamic Energy Measurement

The dynamic energy measurement presented in Chapter 2 is a powerful tool in CDMS. Not only does it remove the need for an energy selective device in CDMS, but it also constitutes a true *ab initio* method for measuring the energy of each ion. Because the energy is encoded in the ratio of the first and second harmonic amplitudes (HAR), the accuracy of the ion energy measurement scale in quadrature with the signal-to-noise ratios (S/N) associated with these two amplitudes. The first harmonic amplitude is also used to calculate ion charge. As a result, any instrument improvements in S/N increase both charge and energy measurement accuracy and, in the limit of a noise-free signal (infinite S/N), this method can theoretically achieve a perfect measurement of ion energy in addition to a perfect charge determination. Other CDMS methods that use energy selective devices, while currently practical, have a best-case scenario where the accuracy of their measurements is limited by the narrowest energy bandpass that still transmits a sufficient number of ions into the detector trap.[10] The importance of an accurate energy measurement can be diminished by designing a trap geometry that more closely approaches a harmonic potential where ion energy no longer affects ion oscillation frequency.[10] However, a true harmonic potential cannot be achieved for a CDMS instrument because the detector electrode must be shielded from outside potentials to facilitate an accurate charge measurement.

With current technology, there is a cross-over point when comparing the measurement accuracy possible using our dynamic, *ab initio* technique versus using a calibrated energy constant derived from a narrow energy bandpass. This crossover occurs when the S/N of the two harmonics is high enough that the associated error in the energy measurement is less than the energy uncertainty introduced by assuming a constant energy for an energy bandpass of finite width. This relationship is illustrated in Figure 6.2, which shows energy measurement error as a function of ion charge. The blue line represents the energy error inherent to the narrowest energy bandpass (~0.3%) achieved by an energy selector in CDMS and is constant irrespective of ion charge. The black line represents the energy error measurement scaling as a function of charge for the CDMS instrument used in the work in this dissertation and the red line represents the theoretical scaling

for the highest S/N charge measurement reported for a CDMS instrument (a 2x improvement in S/N compared to black line). Both the black and red plots assume that the noise at the first and second harmonic are equal. In practice, 1/*f* noise can result in slightly lower noise at the second harmonic frequency, especially for high *m*/*z*, low frequency ions. These data also assume the HAR is equal to 2 for simplicity (typical HAR values range from 1.7–2.4). The cross-over point occurs at 362 *e* for the black data and 181 *e* for the red data. The mass and diameter corresponding to these cross-over charge states can be roughly approximated using a spherical nanodrop charged to the Rayleigh limit (Chapter 5). For the 362 *e* (black) cross-over, this calcuation yields a mass of 20.8 MDa and diameter of 40.4 nm and the 181 *e* yields a mass of 5.2 MDa and diameter of 25.5 nm. Thus, even for existing CDMS instrumentation, the mass at which the *ab initio* energy measurement becomes favorable is relatively close to the lower end of the mass range where CDMS is the preferred technique (Figure 6.1). Because CDMS is a relatively new, still-developing technique, additional improvements to S/N are likely possible. An additional ~2x reduction in noise would decrease the cross-over point to ~90 *e*, corresponding to a mass of ~1.3 MDa and diameter of 16 nm. This is size range where heterogeneity is typically low enough that conventional MS techniques can be used in native MS (Figure 6.1), making the *ab initio* energy measurement technique attractive both for its simplitcity and long-term outlook.

Another key application of CDMS made possible by dynamic energy measurement is to obtain information about the shape of each ion from the same time domain data used to determine the ion mass. The frequency of an ion slowly changes with time as a result of collisions with background gas that reduce the ion energy. The rate of energy loss can be readily determined from this change in frequency, as demonstrated in Chapter 2 and other work.[11,12] The rate of energy loss from collisions roughly correlates with the collisional cross sections measured in conventional drift tube apparatus for small proteins.[12] This calibration of the rate of energy loss to collisional cross sections can be extended to larger analytes using drift-ion mobility and traveling wave ion mobility measurements as calibrants. This will enable the energy loss measured for unknown compounds to be related to their collisional cross sections, with no increase in analysis time over measuring just their individual masses.

Dynamic energy measurements also make it possible to measure the masses of fragment ions formed by precursor dissociation inside the CDMS trap. When an ion dissociates, the signal at the frequency of the precursor disappears with the concomitant appearance of a product ion signal at a different frequency. The temporal correlation of these two signals makes it possible to track which fragment ion comes from which precursor ion, as demonstrated in Chapter 3. The fragment ion initially has an unknown *m*/*z* and energy, but dynamic measurements of ion energy make it possible to measure the energy and hence the *m*/*z* of each fragment ion. Different fragment ions formed from precursor ions of the same mass can be used to obtain a fragmentation spectrum for precursors at that mass. To the extent that the precursor has a unique mass, then a fragmentation spectrum measured from multiple precursor ions of that mass should reflect that obtained from standard ensemble MS/MS measurements. This has the potential to provide useful structural information for macromolecular complexes of unprecedented size.

6.3 Next-generation CDMS Instrumentation

In order to achieve the goal of high-throughput, multiplexed CDMS measurements, a new, innovative instrument design that combines existing quadrupole trapping technology with the novel *m*/*z* and frequency decoupling method will be constructed. A schematic of this design is

shown in Figure 6.3. Ions are produced and desolvated in an ESI ion source and ion funnel. Ions will then be trapped and thermalized in a rectilinear quadrupole trapping stage to remove any correlation between mass and energy caused by aerodynamic acceleration from the ion source. This first trap will have asymptotic guide rods arranged at an angle to the quadrupole (shown in Figure 6.3 in blue).[13] These rods will be held at a constant DC potential, forming a downstream gradient that efficiently transfers the thermalized ions to a second rectilinear quadrupole trap. The second trap will also be equipped with asymptotic field guide rods, but a DC potential pulse is applied to the rods at the same time the downstream exit of the trap is opened. This produces a potential gradient where ions closer to the upstream side of the trap at the time it opens will have higher energies relative to ions near the downstream exit. This energy variance generation step is important because it allows the distribution of ion energies to be tuned via the magnitude of the DC potential pulse applied to the guide rods. Ion energies can be carefully optimized to match the range of energies that have stable trajectories in the detector trap and thereby maximize decoupling and analysis speed. An additional benefit of this instrumental setup is that it naturally accumulates, pulses, and focuses ions into the detector trap during the brief period that it is open between trapping events. This increases the number of ions that can be simultaneously trapped in CDMS instrument and makes multiplexed measurements straightforward even for samples with low analyte concentrations.[14]

6.4 References

(1) Lössl, P.; Snijder, J.; Heck, A. J. R. Boundaries of Mass Resolution in Native Mass Spectrometry. *J. Am. Soc. Mass Spectrom.* **2014**, *25* (6), 906–917.

(2) Uetrecht, C.; Versluis, C.; Watts, N. R.; Wingfield, P. T.; Steven, A. C.; Heck, A. J. R. Stability and Shape of Hepatitis B Virus Capsids in Vacuo. *Angew. Chemie - Int. Ed.* **2008**, *47* (33), 6247–6251.

(3) Weiss, V. U.; Bereszcazk, J. Z.; Havlik, M.; Kallinger, P.; Gösler, I.; Kumar, M.; Blaas, D.; Marchetti-Deschmann, M.; Heck, A. J. R.; Szymanski, W. W.; Allmaier, G. Analysis of a Common Cold Virus and Its Subviral Particles by Gas-Phase Electrophoretic Mobility Molecular Analysis and Native Mass Spectrometry. *Anal. Chem.* **2015**, *87* (17), 8709–8717.

(4) Thomas, S.; Cole, M.; Villa-López, F. H.; Gardner, J. W. High Frequency Surface Acoustic Wave Resonator-Based Sensor for Particulate Matter Detection. *Sensors Actuators, A Phys.* **2016**, *244*, 138–145.

(5) Liu, J.; Hao, W.; Liu, M.; Liang, Y.; He, S. A Novel Particulate Matter 2.5 Sensor Based on Surface Acoustic Wave Technology. *Appl. Sci.* **2018**, *8* (1), 82.

(6) Keifer, D. Z.; Pierson, E. E.; Jarrold, M. F. Charge Detection Mass Spectrometry: Weighing Heavier Things. *Analyst* **2017**, *142* (10), 1654–1671.

(7) Botamanenko, D. Y.; Jarrold, M. F. Ion-Ion Interactions in Charge Detection Mass Spectrometry. *J. Am. Soc. Mass Spectrom.* **2019**, *30* (12), 2741–2749.

(8) Keifer, D. Z.; Shinholt, D. L.; Jarrold, M. F. Charge Detection Mass Spectrometry with Almost Perfect Charge Accuracy. *Anal. Chem.* **2015**, *87* (20), 10330–10337.

(9) Todd, A. R.; Barnes, L. F.; Young, K.; Zlotnick, A.; Jarrold, M. F. Higher Resolution Charge Detection Mass Spectrometry. *Anal. Chem.* **2020**, *92* (16), 11357–11364.

(10) Hogan, J. A.; Jarrold, M. F. Optimized Electrostatic Linear Ion Trap for Charge Detection Mass Spectrometry. *J. Am. Soc. Mass Spectrom.* **2018**, *29* (10), 2086–2095.

(11) Elliott, A. G.; Harper, C. C.; Lin, H. W.; Williams, E. R. Mass, Mobility and MSN Measurements of Single Ions Using Charge Detection Mass Spectrometry. *Analyst* **2017**, *142* (15), 2760–2769.

(12) Elliott, A. G.; Harper, C. C.; Lin, H. W.; Susa, A. C.; Xia, Z.; Williams, E. R. Simultaneous Measurements of Mass and Collisional Cross-Section of Single Ions with Charge Detection Mass Spectrometry. *Anal. Chem.* **2017**, *89* (14), 7701–7708.

(13) Yan, J.; Zhou, M.; Gilbert, J. D.; Wolff, J. J.; Somogyi, Á.; Pedder, R. E.; Quintyn, R. S.; Morrison, L. J.; Easterling, M. L.; Paša-Tolić, L.; Wysocki, V. H. Surface-Induced Dissociation of Protein Complexes in a Hybrid Fourier Transform Ion Cyclotron Resonance Mass Spectrometer. *Anal. Chem.* **2017**, *89* (1), 895–901.

(14) Todd, A. R.; Jarrold, M. F. Dramatic Improvement in Sensitivity with Pulsed Mode Charge Detection Mass Spectrometry. *Anal. Chem.* **2019**, *91* (21), 14002–14008.

6.5 Figures

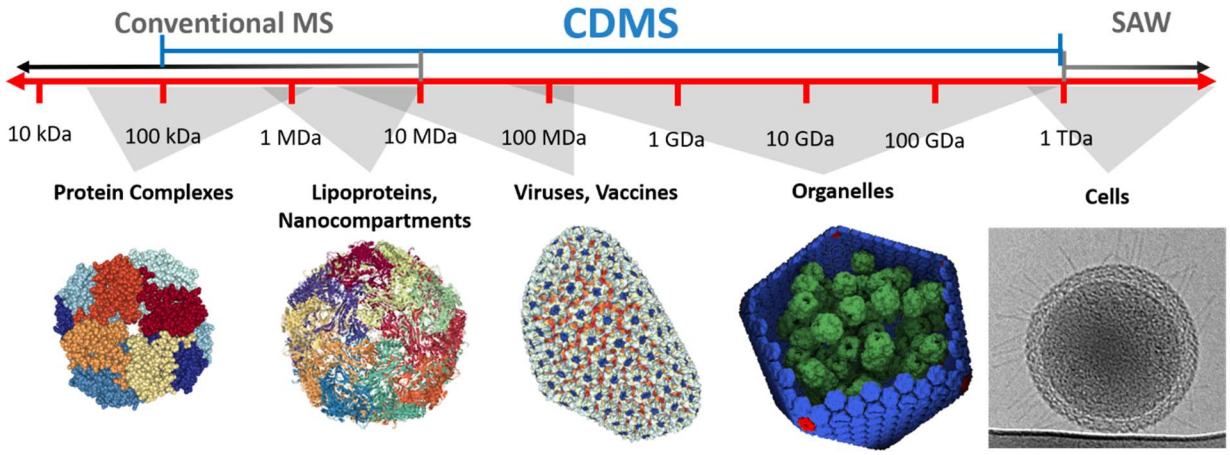


Figure 6.1. Ranges for different mass measurement technologies. The wide mass range of CDMS fills the gap between existing technologies and makes native analysis of many important molecules/complexes possible.

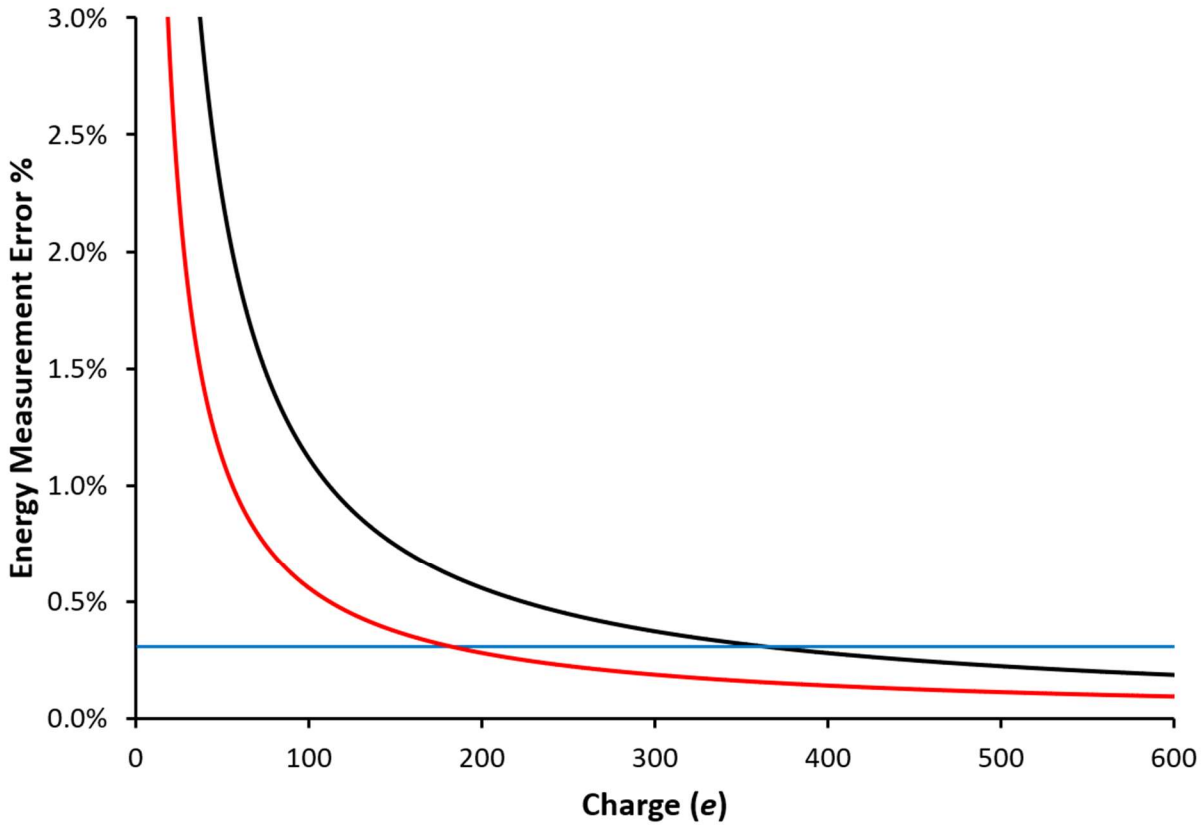


Figure 6.2. Plot of energy measurement error as a function of ion charge for different energy measurement strategies. The energy measurement error inherent to *ab initio* measurement of ion energy from ion signal harmonics in CDMS (red and black plots) decreases with ion charge, but using energy selective optics to admit a narrow distribution of ion energies into the CDMS detector is unaffected by ion charge (blue plot). The black plot is based the average noise determined for the CDMS instrument used in this dissertation and the red plot reflects the lowest noise measurements achieved in CDMS. The cross-over points at 181 *e* (red-blue) and 362 *e* (black-blue) indicate the approximate charge where the *ab initio* method results in less energy measurement uncertainty than the energy selector method.

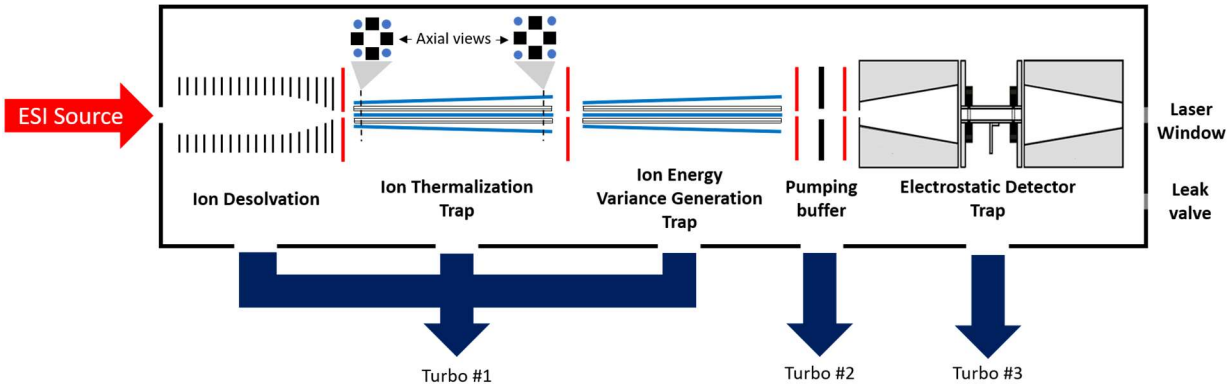


Figure 6.3. Schematic of next-generation CDMS instrumentation. Multiple differentially pumped stages of ion optics desolvate, thermalize, and then inject ions with a variable energy distribution into the detection stage where ions are measured.